Investigations on Turbulence for Wind Turbine Aerodynamics

Bernhard Stoevesandt

Von der Fakultät für Mathematik und Naturwissenschaften
der Carl von Ossietzky Universität Oldenburg
zur Erlangung des Grades und Titels eines

Doktors der Naturwissenschaften
Dr. rer. nat.
angenommene
Dissertation

von Herrn Bernhard Stoevesandt
geboren am 8.6.1970 in Bremen

Gutachter: Prof. Dr. Joachim Peinke
Zweitgutachter: Prof. Dr. Claus Wagner
Tag der Disputation: 8.4.2010

Philosophers have only interpreted the world in various ways, however it is a matter of changing it. (Karl Marx)

Inhaltsverzeichnis

Abbildungsverzeichnis

Abstract

Blades of wind turbines face strong fluctuations of incoming wind. This causes rapid changes in the angle of attack at the different blade sections leading to changes in the loads. Since aerodynamic loads are often calculated by averaging equations, the real loads are often not grasp. Therefore in this work methods are used and being investigated which consider the unsteady and turbulent characteristics on the wind turbine aerodynamics. From this a main question of this work evolved, how much information can be gained from time resolved numerical simulation using spectral element methods. The thesis is about three different fields of aerodynamics related to turbulent flow on the background of wind energy converters.

At first a high order accuracy computational fluid dynamics code using the spectral finite elements method was used to simulate the flow over an airfoil. The method is being described and capabilities of the code were analyzed. The resultant flow field from the simulation is being characterized.

Further, with the aim of the improvement of stochastic flow modeling, an analysis of the turbulent field in the wake of the airfoil is done to improve the understanding of the turbulent characteristics in an inhomogeneous flow field. Therefore a time series at a point in the flow is being characterized by a multipoint correlation method based on Markov properties. After determining Markov properties within the flow the time series was reconstructed. Further the analysis was extended onto spatially distributed points with a simultaneous reconstruction of a time series of the field at a distant point. Even though there were some deviances in the statistical properties between the reconstructed and the simulated time series, the results strongly indicate the possibility to gain accuracy in the spatial modeling of turbulence with the method.

Finally, to improve the calculation of dynamic stall and stall flutter due to wind fluctuations on wind turbines the basic distributions of the inflow on the turbines are being analyzed. Therefore changes in wind speed and wind direction of measurement are being analyzed at high frequencies. This is used to estimate changes in the angle of attack (AOA) on a blade segment of a turbine over short time periods for different estimated turbine concepts. Here a stochastic approach is chosen to grasp the characteristics of the probability distributions to give an over all view of the magnitude and rate of the changes.

Zusammenfassung

Die Blätter von Windkraftanlagen sind starken Fluktuationen durch den einströmenden Wind ausgesetzt. Dies verursacht schnelle Änderungen im Angriffswinkel an den verschiedenen Blattabschnitten und dadurch schnelle Wechsel in den Lasten, welche oft mit mittelden Gleichungen berechnet werden. Dadurch werden jedoch die realen Lasten nicht ermittelt. Daher werden in dieser Arbeit Methoden untersucht, welche die instationren und turbulenten Eigenschaften in der Aerodynamik von Windkraftanlagen wiedergeben. Daraus entwickelte sich eine Hauptfrage der Arbeit danach, wieviel an Informationen durch eine zeitaufgelöste Simulation mit spektraler Elemente Methode gewonnen werden können. Diese Arbeit handelt von drei verschiedenen Feldern im Zusammenhang mit turbulenter Strömung vor dem Hintergrund von Windkraftanlagen.
Erstens wird ein Programm für hoch auflösende Computational Fluid Dynamics, welches auf der Methode spektraler, finiter Elemente basiert, genutzt um die Strömung über ein Flügelprofil zu berechnen. Die Methode wird beschrieben und die Möglichkeiten und Grenzen der Simulation mit dem Programm wurden ergründet. Das aus der Simulation resultierende Strömungsfeld wird charakterisiert.
Im Nachlauf des Profils entstand ein turbulentes Strömungsfeld. Dieses wird im zweiten Teil mit dem Ziel der Verbesserung stochastischer Strömungsmodelle analysiert um das Verständnis der Turbulenzeigenschaften in inhomogener Turbulenz zu verbessern. Dafür wird die Zeitserie an einem Punkt in der Strömung mit Hilfe einer auf Markov-Prozessen basierende Vielpunkt-Korrelationsanalyse beschrieben. Nachdem Markov-Eigenschaften gefunden wurden, konnten die Zeitserie mit empirisch bestimmten Prozessgleichungen rekonstruiert werden. Des weiteren wurde die Analyse auf räumlich verteilte Punkte ausgedehnt indem auch die Zeitserie an einem entfernten Punkt zum gleichen Zeitpunkt rekonstruiert wurde. Auch wenn es noch Abweichungen in den statistischen Eigenschaften zwischen der rekonstruierten und der simulierten Zeitreihe gibt, so weisen die Ergebnisse deutlich darauf hin, dass es möglich sein kann, mit der Methode einen Gewinn an Genauigkeit in der räumlichen turbulenz Modellierung zu erzielen.
Schließlich werden im weiteren zur besseren Berechnung des dynamischen Stalls und Ablöseflattern an Windkraftanlagen die grundlegenden Verteilungen der Anströmung analysiert. Deshalb wurden im weiteren werden Änderungen in Windgeschwindigkeit

und Windrichtung aus einer Messung hochfrequent beschrieben. Dies wird genutzt um Änderungen im Angriffswinkel an einem Blattabschnitt einer Windkraftanlage für unterschiedliche Anlagenkonzepte abzuschätzen. Es wird ein stochastischer Ansatz gewählt um die Eigenschaften der Wahrscheinlichkeitsverteilungen zu erfassen und einen Überblick über die Größe und Frequenz der Änderungen zu geben.

Chapter 1

Introduction

1.1 Wind Turbine Development and Wind Turbine Research

The development of wind turbines for electricity production has made enormous progress during the last 20 years. This is certainly reflected by the size of the produced turbines, which is often referred to (e.g. fig. 1.1). The size itself is not of such a great importance in the economized world. More important than the size of a turbine is today its efficiency, cost reduction and the overall compatibility. On these terms the wind turbine development has made large progress, leading to an outstanding growth in the amount of installed turbines world wide as fig. 1.2 shows.

Ten years ago wind turbine were only economically compatible when subsidized by support programs as there were the guaranteed payment systems in Denmark from the 1980s and Germany from 1992 [3]. Today such subsidies are at good sites not necessary anymore. However to use the overall potential of the wind energy, the support of in itself uneconomical projects is still necessary[1]. The preceding development has proven that such projects foster the development of wind turbines to an extend, that in the end the use of wind energy will become an economical and ecological option world wide.

Nevertheless the strong development of the wind turbines should not conceal that still large progress is to be made. First of all the cost of operation maintenance for wind turbines are still very high with 20-25 % of all costs [4]. Long term studies of the failure rate of wind turbines showed that over a longer period of time almost every two years a turbine experience a failure in a major mechanical part (see fig. 1.3)[5]. Since the turbines and their parts are supposed to be constructed for a 20 years lifetime, the question comes up, why there are some many failures at shorter periods.

[1] Here we argue on basis of the current economic model, regardless of environmental or future costs that arise from the use of the use of fossil fuels

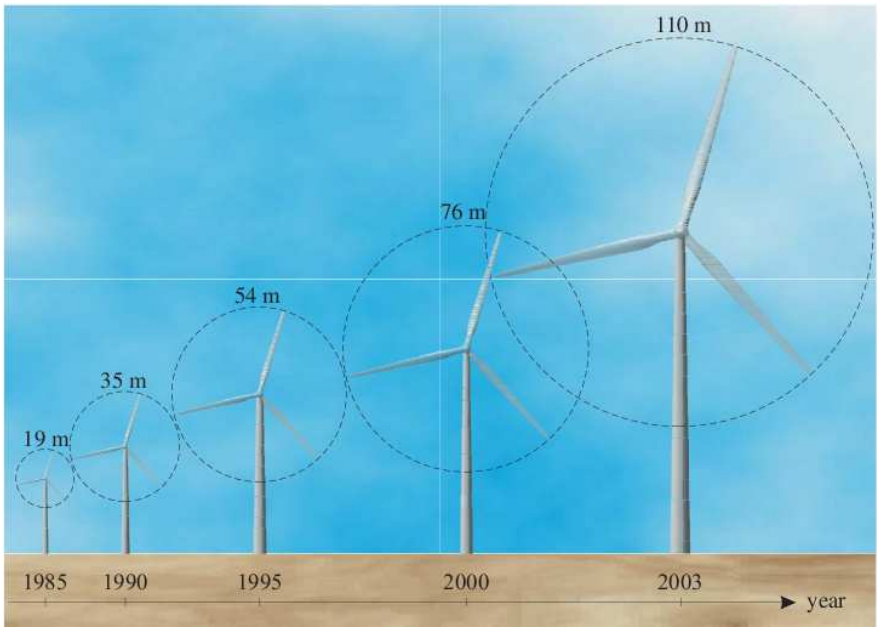

Figure 1.1: Growth in size of the wind turbines over the time period 1985-2003 (image from [1]).

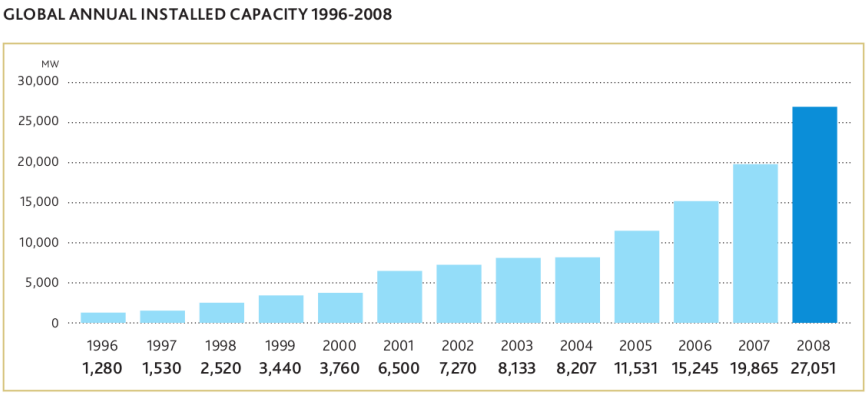

Figure 1.2: The increase of the installed wind power capacity world wide during the last 13 years, shows the development of wind power from a small niche technology to a serious source of electrical power (image from [2])

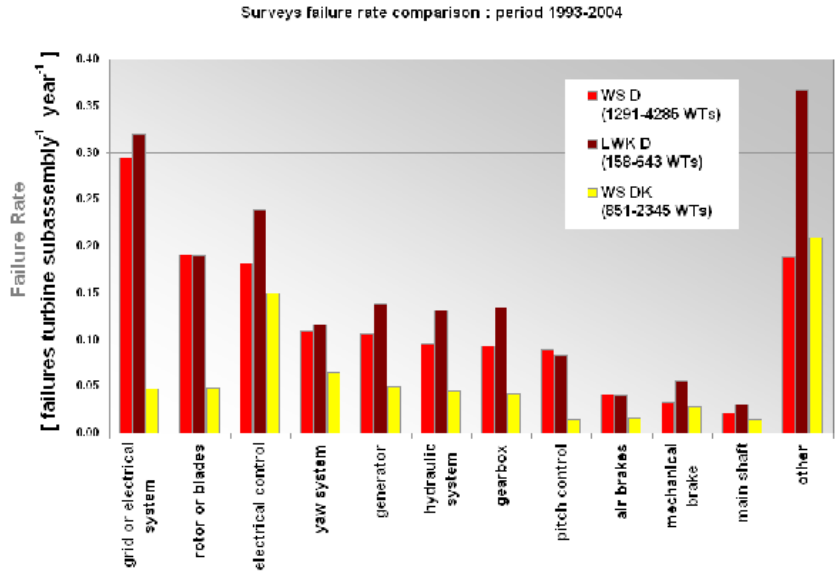

Figure 1.3: Surveys of failure rates from Denmark and Germany for different components of wind turbines in the year 1993-2004 (image from [5])

The problem of high maintenance cost is enhanced for turbines at special locations as mountainous areas or offshore. Both areas offer very promising sites with high wind speeds posing an attractive potential for the use of wind energy. Hence there are challenges for further development that needs to be tackled. Some of the main challenges for the development on which research could focus are

- the high construction cost for offshore wind turbines, making mainly very large turbines efficient. Therefore the interest in the development of larger turbines remains. Further the foundation of the turbines in many different depths is still a very open question. One main topic for offshore turbines are the extreme high maintenance costs. Hence there is an interest in extremely reliable turbines [6].

- the highly turbulent wind fields e.g. caused by complex terrain like mountainous areas [7]. Tilted, upward inflow as well as very irregular turbulence cause extra loads on the turbines and lead to higher maintenance cost [8]. A further problem poses icing on the blades, changing weight and the aerodynamic conditions [9].

- the development of small turbines for urban or very remote areas without grid connection. While the focus of the research has been on large turbines with a rated power ≥ 100 kW, such turbines are not everywhere applicable. Thus small turbines offer to tap new potentials of the use of wind energy [10]. Due to the smaller size many different design types are possible. A

major problem for such turbines is however the strong turbulence they face due to buildings, in urban areas or due to the influence of the turbulent boundary layer as they do not reach large heights [11].

One likely reason for high failure rates is the underestimation of the turbulence in the wind field and the resulting fluctuations in the wind experienced by the turbines. After all some of the most pressing challenges for wind turbine development are directly related to the problems caused by the turbulent flow of the incoming wind field.

1.2 Turbulent Wind Field and Wind Turbines

As turbulence we describe the characteristic of a property to vary significantly and irregularly in time and/or space [12]. The wind which drives the wind turbines is a highly turbulent field showing fluctuations on many different scales. Driven by the geostrophic wind in the upper atmosphere, the wind field forcing wind turbines is mainly a boundary layer flow (a description of the vertical offshore wind field is given e.g. by Tambke et. al. in [13]) . Therefore the turbulence of the wind is a superposition of different phenomenon from quasi two dimensional large vortices of the weather systems to wind shear and all kinds of three dimensional smaller scale turbulence due to wind-surface interactions. This results locally on the surface area of a wind turbine in strong and sudden fluctuations in the wind field.
Such turbulence causes loads on the turbines, which needs to be taken care of in the construction process for such turbines. The IEC standard [14] suggests for the simulation of the turbulent field on one hand the Mann model [15] or the Kaymal model. The latter calculates on the base of a spectrum and thus ends up with a model of purely Gaussian fluctuations. This is however underestimating strong short term fluctuations as Böttcher has shown [16], whose results are approved for another wind field in Chapter 5.
Theoretically the Mann model (see [15]) can be used to superimpose different wind field fluctuating in a Gaussian distributed way for smaller time periods to achieve an intermittent distribution of the over all wind fluctuations. This would be closer to the measured wind fields. However, Gottschall showed for 10 minute intervals that the wind fluctuations at 1 Hz within these intervals are not purely Gaussian [17], therefore such superimposed models still do not grasp the real wind turbulence. The flatness of such distributions might be scattered. Therefore the assumption of a constant flatness - as Gaussian distributions would assume - does not correctly reproduce the measured fluctuations of the wind. This does lead to an underestimation of strong fluctuations due to turbulent wind.
However such wind field models are an important input for the design of wind turbines. The two main aerodynamic engineering models for the construction of wind turbines are the lifting line model and the blade element momentum theory.

Both methods rely on the knowledge of the wind and - mostly an assumption of - the angle of attack, local lift and (for BEM) drag coefficients [18]. While lift and drag coefficient are mostly determined by wind tunnel measurements in wind tunnel conditions [19], the angle of attack is being estimated by models (see e.g. [20][21]). Turbulent wind complicates the situation, as the angle of attack in a situation of rapidly changing inflow is also changing. This leads to a dynamic flow separation called dynamic stall [22] with a differing lift and drag behavior. Again there exist models for the effect, mostly coming from helicopter research [23]. However their accuracy and applicability to wind turbine situations is an open field for research [24][25][26]. One problem is, that in the situation of the turbulent wind, changes in angle of attack are stochastic distributed, so that deterministic models not reflecting this situation will have a limited validity. Another problem is that the actual flow situation on a blade section or airfoil in dynamic stall is hardly know. Thus the existing turbulent wind is in many ways just approximated by the aerodynamic models for the design of wind turbines, making it very likely that unexpected and unclassified failures of components of wind turbines can be caused by this fact.
A different approach for aerodynamic modelling is the attempt to solve the underlying physical equations of the existing flow by numerical methods - called computational fluid dynamics (CFD).

1.3 Simulating Turbulent Flow

1.3.1 The Navier-Stokes Equations

Principally the physics of fluid dynamics is described by the conservation of mass, energy and momentum. Also the conservation of angular momentum can be used for the analysis by the vortex equations [27]. However for the application of the aerodynamics for wind turbines the fluid flow is fully described by the so called momentum equation

$$\partial_t(\rho u_i) + u_j \partial_j(\rho u_i) = -p + \partial_j \tau_{ji} + F_i, \tag{1.1}$$

and the mass conservation

$$\partial_t \rho \partial_j(\rho u_j) = 0. \tag{1.2}$$

These equations are referred to as the Navier-Stokes equations (although sometimes the energy conservation is included [28]). Where ρ is the density of the fluid, u_i are the three velocity components, p is the pressure, τ_{ij} is the viscous stress tensor and F_i are the external forces on the medium. In general it is said, that the approximation of an incompressible fluid can be made if the $|u| \leq 0.3Ma$, where $Ma = \frac{|u|}{c}$ is the Mach number and c is the speed of sound in the medium,

which is about 340 m/s for air near the earth surface [29]. For a wind turbine with a 80 m diameter and a rotational speed of 20 rpm, this criterion holds for the whole blades. The tip would run at a $0.25Ma$, where the approximation of an incompressible flow is still good, but closer to the range at which compressibility should be assumed. This is also stressed by the fact that most of the noise wind turbine cause, is generated in the outer and tip region of the blade [30].
Nevertheless at the given Mach number, for the simulations of flow on wind turbines, it is usually sufficient and often numerically more accurate to calculate with the estimation of an incompressible fluid, where $\rho = const.$. This changes the Navier-Stokes equations to

$$\partial_t u_i + (u_j \partial_j) u_i = -\frac{1}{\rho} \partial_i p + \nu \partial_j^2 u_i + f_i, \tag{1.3}$$

$$\partial_i u_i = 0. \tag{1.4}$$

If not otherwise stated i will use further on normed, non-dimensional magnitudes, as it is commonly done in fluid flow calculations

$$u_i^* = \frac{u_i}{U_0} \tag{1.5}$$

$$x_i^* = \frac{x_i}{l_c} \tag{1.6}$$

$$p^* = \frac{p}{\rho U_0^2}, t^* = \frac{t U_0}{l_c}, \tag{1.7}$$

$$f_i^* = \frac{l_c \cdot f_i}{U_0^2}. \tag{1.8}$$

For simulations the typical choices for normalization are that U_0 is the average inflow velocity, and the characteristic length l_c is the chord length of the airfoil. This changes the Navier-Stokes equations to

$$\partial_{t^*} u_i^* + (u_j^* \partial_j) u_i^* = \partial_i p^* + \frac{1}{Re} \partial_j^2 u_i^* + f_i^*, \tag{1.9}$$

$$\partial_i u_i^* = 0. \tag{1.10}$$

In most of this work this non-dimensional version with the Reynolds number Re as parameter will be used. For convenience reasons the * will be left away.

1.3.2 Discretisation

Due to the non-linear terms an analytical solution for the Navier-Stokes equations have not been found. With the increase of computational power however, numerical approaches by means of computational fluid dynamics (CFD) have been progressively successful for many situations. These approaches have some premises.
The Navier-Stokes equations are field equations. The information of the properties within the field can computationally only obtained for discrete points in space and time. Therefore the overall field is at first spatially discretised. There exist different methods to do so, such as finite-difference, finite volumes, finite element or spectral methods [29]. All in common is, that they can only resolve scales to which their discretisation is fitted to. This poses a problem for the resolution of turbulent flow as very small scales need to be resolved, thus increasing the amount of computational cost enormously (see Chapter 2). As a result some models for the turbulent flows have been established to approximate the behavior of the turbulence either in time or spatial terms. However most of the models are limited in their accuracy already when simulating airfoils [31][32][33].
For the calculation of the aerodynamics of wind turbines the CFD methods are a tempting approach to overcome the deficiencies of simple engineering models that struggle to grasp the effects of turbulence. However the dimensions and scales of the inflow turbulence as well as the dimensions of todays turbines make accurate load calculations using CFD for wind turbines almost impossible[2]. It is still a problem to grasp the correct load for simplified models such as the mentioned dynamic stall on airfoils [34].

1.4 Scope and Structure of the Thesis

The aim of the thesis is to improve the knowledge of turbulence impact on local structures on wind turbines. Since we do consider computational methods for the calculation of flow situations a promising approach, the focus of this thesis was to contribute to the improvement of the understanding of the physical processes of the flow on wind turbines by advanced computational methods. A high order approach to computational fluid dynamics has been used to simulate the flow over an airfoil using non approximated direct numerical simulation. The method has some advantages over other CFD methods. The basic principle, its advantages and drawbacks are being discussed in chapter 2.
Using this method for a simulation at Reynolds numbers in the order of 10^3 (chapter 3) has been done and analyzed to get a deeper understanding of the flow characteristics on airfoils and the transition to turbulence on them. The data

[2]Compare e.g. the proceedings of the European Wind Energy Conference 2009, where CFD-Methods have mostly been used for wake calculations http://www.ewec2009proceedings.info

gained by the first simulation has further been used to analyze the stochastic properties of the flow field and reconstruct time series with shifts in time in space using the Langevin equation. The method is explained and exemplarily verified on the data of the flow field in chapter 4.
Airfoils themselves are on wind turbines just sections of the complete blade. In chapter 5 an analysis of the statistics of the fluctuations of the angle of attack for such airfoils has been done to achieve also a greater knowledge on the actual processes for the modeling of dynamic stall.

Bibliography

[1] Jesper Winther Larsen. *Nonlinear Dynamics of Wind Turbine Wings*. PhD thesis, Aalborg University, July 2005.

[2] Angelika Pullen, Liming Qiao, and Steve Sawyer. Global wind 2008 report. Rue D'Arlon 63-65, 1040 Brussels, Belgium, 2009.

[3] Christine Luch. Optimisation of the share of renewable energies in electricity systems. Master's thesis, Fernuni Koblenz, Koblenz, 2006.

[4] Invest in the future: wind energy, finance and economics. Brussels, Belgium, 2008.

[5] Peter Tavner, Fabio Spinato, Gerard van Bussel, and Efstathios Koutoulakos. Reliability of different wind turbine concepts with relevance to offshore application. In *Proceedings of the EWEC 2008*, 2008.

[6] Prioritising wind energy research. Brussels, Belgium, 2005.

[7] R. J. Barthelemie, S. T. Frandsen, O. Rathmann, K. Hansen, E.S. Politis, J. Prospathopoulos, D. Cabezon, K. Rados, S.P. van der Pijl, J. G. Schepers, W. Schlez, J. Phillips, and A. Neubert. Flow and wakes in large wind farms in complex terrain and offshore. In *Proceedings of the EWEC 2008*, 2008.

[8] Takeshi Kamio, Shingo Kanazawa, Makoto Iida, and Chuichi Arakawa. The wind direction error problem in numerical site calibration. In *Proceedings of the EWEC 2009*, 2009.

[9] Matthew C. Homola, Tomas Wallenius, Lasse Makkonen, Per J. Nicklasson, and Per A. Sundsbo. The dependence of icing severity on chord length. In *Proceedings of the EWEC 2009*, 2009.

[10] J. M. Dores Costa, Nelson Pimenta, Ricardo Rei, Fernando Cardoso, and Paulo Chaves. 1 small-power wind turbine system for urban applications. In *Proceedings of the EWEC 2008*, 2008.

[11] G. Desmet, P. Tant, B. Blocken, K. van Acker, M. Konings, T. Wijsmans, and J. Driesen. Design of a grid-connected roof-mounted wind turbine test system. In *Proceedings of the EWEC 2008*, 2008.

[12] Stephen B. Pope. *Turbulent Flows*. Cambridge University Press, 2000.

[13] Jens Tambke, Lorenzo Claveri, John A. T. Bye, Carsten Poppinga, Bernhard Lange, Lueder von Bremen, Francesco Durante, and Jörg-Olaf Wolff. Offshore meteorology for multi-mega-watt turbines. In *Proceedings of the EWEC 2006*, 2006.

[14] IEC. International standard iec 61400-1, wind turbines part 1: Design requirements. Technical report, International Electrotechnical Commission, 2005.

[15] Jakob Mann. Wind field simulation. *Prob. Engineering Mechanics*, 13(4):269–282, 1998.

[16] Frank Böttcher, Joachim Peinke, Christoph Renner, and Hans-Peter Waldl. Onthe statistics of wind gusts. *Boundary-Layer Meteorology*, 108:163–173, 2003.

[17] Julia Gottschall. *Modelling the variability of complex systems by means of Langevin processes*. PhD thesis, Oldenburg University, 2009.

[18] Tony Burton, David Sharpe, Nick Jenkins, and Ervin Bossanyi. *Wind Energy Handbook*. John Wiley & Sons, Ltd, Chichester, 1. edition, 2001.

[19] Dieter Althaus and F. X. Wortmann. *Stuttgarter Profilkatalog IF. X. Wortman*. Vieweg, Braunschweig/Wiesbaden, 1981.

[20] Tonio Sant, Gijs von Kuik, and Gerard J. W. van Bussel. Estimating the angle of attack from blade pressure measurements on the NREL phase VI rotor using a free wake vortex model: axial conditions. *Wind Energy*, 9:549–577, 2006.

[21] Wen Zhong Shen, Martin O. L. Hansen, and Jens Nørkær Sørensen. Determination of angle of attack (aoa) for rotating blades. In Joachim Peinke, Peter Schaumann, and Stephan Barth, editors, *Wind Energy*, Euromech Colloquium, pages 205–209. Springer, 2007.

[22] William J. McCroskey. Unsteady airfoils. *Annual Review of Fluid Mechanics*, 14:285–311, 1982.

[23] Daniel Young Reber. *Modelbildung und Regelung zur Reduktion von Vibrationen und 'Dynamic Stall bei Hubschrauberrotoren*. PhD thesis, Universität Stuttgart, 2008.

[24] Sandeep Gupta and J. Gordon Leishman. Dynamic stall modelling of the s809 aerofoil and comparison with experiments. *Wind Energy*, (9):521–547, 2006.

[25] Jesper Winther Larsen, S. R. K. Nielsen, and S. Krenk. Dynamic stall model for wind turbine airfoils. *Journal of Fluids and Structures*, 23:959–982, 2007.

[26] Antoine Ducoin, Jacques Andre Astolfi, Francois Deniset, and Jean-Francois Sigrist. Computational and experimental investigation of flow over a transient pitching hydrofoil. *European Hournal of Mechanics B/Fluids*, 28:728–743, 2009.

[27] Jean Matieu and Julian Scott. *An Introduction to Turbulent Flow*. Cambridge University Press, 1 edition, 2000.

[28] John C. Tannehill, Dale A. Anderson, and Richard H Pletcher. *Computational Fluid Mechanics and Heat Transfer*. Series in Computational and Physical Processes in Mechnaics and Thermal Sciences. Taylor & Francis, Washington, 2nd edition, 1997.

[29] Joel H. Ferziger and Milovan Peric. *Computational Methods for Fluid Dynamics*. Spinger, 3. edition, 2002.

[30] Stephan Oerlemans and B. Mendez Lopez. Acoustic array measurements on a full scale wind turbine. Technical Report NLR-TP-2005-336, Nationaal Lucht- en Ruimtevaartlaboratorium, 2005.

[31] L. Davidson, D. Cokljat, F. Fröhlich, A. Leschziner, C. Mellen, and W. Rodi, editors. *LESFOIL Large Eddy Simulation of Flow Around a High Lift Airfoil*, volume 83 of *Notes on Numerical Fluid Mechanics*. Springer Verlag, 2003.

[32] Chaoqun Liu. High performance computation for dns/les. *Applied Mathematical Modeling*, 30:1143–1165, 2006.

[33] Mads Reck. *Computational Fluid Dynamics, with Detached Eddy Simulation and the Immersed Boundary Technique, Applied to Oscillation Airfoils and Vortex Generators*. PhD thesis, Technical University of Denmark, December 2004.

[34] John A. Ekaterinaris, M. S. Chandrasckhara, and Max F. Platzer. Recent development in dynamic stall measurements, computations and control. In *Proceedings of the 43rd AIAA Aerospace Sciences Meeting*, volume AIAA 2005-1296, January 2005.

Chapter 2

Introduction to the Spectral Finite Element Method

For the numerical simulation in this work the $\mathcal{N}\varepsilon\kappa\mathcal{T}\alpha r$-code has been used in a version from 2002, provided by Spencer Sherwin. It uses the high order spectral/hp method for flow simulations, combining the "accuracy and good phase properties of spectral methods with the geometric flexibility of finite element method"[1]. The method has been used and validated for many different cases like cylinder flow [2][3], bats flight [4] or artery flow [4]. Most of this work was done on rather low Reynolds numbers $\leq 10^3$. Nevertheless there have been some exceptions where the code has been used for simulation of higher Reynolds numbers [5]. Inspired by this fact and further studies by the developers of the code [6][7], in this work we have used the method for a different purpose. The aim of this research was to try to implement the method for high accuracy airfoil simulations. The science of airfoil simulations however uses some methods that are not applicable to this code and most likely to this method. Additionally the method has some delicate details which are to be presented here. This does not mean that the method is not useable. It rather means that it is important to mind the proper use of the method. In this chapter a further insight into the functioning of the code, its advantages and limits is given.

2.1 How to calculate with Spectral Methods for Finite Elements

As stated before, the spectral/hp method refers to a combination of finite elements and spectral methods, allowing grid-h- and spectral-order-p-refinement. In the following the method as implemented in the $\mathcal{N}\varepsilon\kappa\mathcal{T}\alpha r$-code is described. The principles of the method are explained by S. Sherwin and G.E. Karniadakis in [8], which is a main reference in the following. However more detailed understanding can gained by a large number of articles cited in this chapter.

To increase the comprehensibility in the following the main method will mainly be explained in two dimensions. Later the third dimension will be included
The aim is to calculate the flow properties using the Navier-Stokes equations (1.10) in a domain $\Omega \in \mathbb{R}^2$. This domain has been subdivided into K elemental subdomains Ω^k. The properties in the domain can be approximated with a function $f(t,x,y)$ by a C^0 continuous expansion over the K subdomains as

$$f(t,x,y) = \sum_{k}^{K} \sum_{n} \hat{f}_n^k(t)\phi_n(x,y) \tag{2.1}$$

where $\hat{f}_n^k(u)$ are the expansion coefficients in the kth subdomain and ϕ_n are the basis functions. x and y are the 2D global coordinates in a Cartesian coordinate system. Within each of the subdomains the expansion has to take place. Therefore it is most convenient to map the global coordinates (x,y) to local coordinates (a,b)[9][10] with

$$Q^2 = \{(a,b)| -1 \leq a,b \leq 1\}. \tag{2.2}$$

Since for many applications unstructured meshes are needed, a triangular coordinate system is also defined

$$T^2 = \{(r,s)| -1 \leq r,s; r+s \leq 0\}. \tag{2.3}$$

Now a mapping from local quadrilateral coordinates to the triangular system with (r,s) as coordinates can be undertaken with

$$\begin{aligned} r &= 2\left(\frac{1+a}{2}\right)\left(\frac{1-b}{2}\right) - 1 \\ s &= b, \end{aligned} \tag{2.4}$$

and of course backwards

$$\begin{aligned} a &= 2\left(\frac{1+r}{1-s}\right) - 1 \\ b &= s. \end{aligned}$$

It is common to refer to the subdomains described here as “elements”, since each subdomain is an element of the whole domain. In the following this term will also be used here.
Due to the normed and mapped coordinate system it is possible to use Jacobi polynomials $P_n^{\alpha,\beta}(a)$ as basis functions. Such polynomials represent the family of solutions to a Sturm-Liouville, which are read for one dimension with $a \in (-1;1)$:

$$\frac{d}{da}\left[(1-a)^{1+\alpha}(1+a)^{1+\beta}\frac{d}{da}P_n^{\alpha,\beta}(a)\right] = -n(\alpha+\beta+n+1)(1-a)^{\alpha}(1+a)^{\beta}P_n^{\alpha,\beta}(a),$$

with n being the polynomial order, and $\alpha, \beta > -1$ coefficients characterizing the polynomials. If we set $\alpha, \beta = 0$, we get the Legendre Polynomial $P_n^{0,0}(x)$. The bases are decomposed into vertex, edge and interior modes. This enables easily a continuity C^0 at the edges and vertices [9]. The general expansion basis was described by Proriol, Koornwinder and Dubiner independently [11][12][13] for a triangular basis as

$$\phi_{nm}(r,s) = P_n^{0,0}\left(2\frac{(1+r)}{(1-s)} - 1\right)(1-s)^n P_m^{2n+1,0}(s). \tag{2.5}$$

Where n and m are the expansion orders, which could be differing for different directions. Using such a basis, differentiation and integration are being done on the elemental level.

The L^2-norm for the spectral resolution within a subdomain can be calculated for example for a Legendre expansion with Legendre polynomials $P_n^{0,0}(a,b)$ in local coordinates a, b by

$$||\varepsilon||_2 = \left[\int_{-1}^{1} |u(a,b) - \sum_{n=0}^{P} \hat{u}_n P_n^{0,0}(a,b)|^2 dadb\right]^{\frac{1}{2}}. \tag{2.6}$$

This leads to an estimation showing clearly an exponential decrease of $||\varepsilon||_2$ with the increase of the polynomial order P, whereas a refinement using the amount of subdomains/elements shows a clearly smaller decrease in error (see e.g. [8] pp. 68-80).
On the other hand the calculation time increases by $W_C \propto \mathcal{O}(NP^{dim+1} \cdot M)$ with N being the number of elements, dim the number of dimensions of the problem to be solved by spectral elements and M the number of Fourier planes (for a homogeneous third dimension - see below) [14].
The time evolution in the momentum equation (1.10) is described by Karnadakis et. al. in [15]. It is a high order splitting scheme. This scheme propagates the field $U^g = U(x,y,t^g)$ and $p^g = p(x,y,t^g)$ over a time step Δt to calculate U^{g+1} and p^{g+1}:

$$\frac{\hat{U} - U^g}{\Delta t} = \sum_{q=0}^{J_e-1} \beta_q N(U^{g-q}) + f^{g+1}, \tag{2.7}$$

$$\frac{\hat{\hat{U}} - \hat{U}}{\Delta t} = -\partial_i \bar{p}^{g+1}, \tag{2.8}$$

$$\frac{U^{g+1} - \hat{\hat{U}}}{\Delta t} = \nu \sum_{q}^{J_i-1} \gamma_q L(U^{g+1-q}), \tag{2.9}$$

using

$$\begin{aligned} N(U) &= (U_i \partial_i U_j), \\ L(U) &= d_i^2 U, \\ \partial d_i \bar{p}^{g+1} &= \frac{1}{\Delta t} \int_{t^g}^{t^{g+1}} \partial_i p dt. \end{aligned} \tag{2.10}$$

With J_e and J_i denote the explicit and implicit order of the scheme respectively and β_q and γ_q being appropriately chosen weights.
So far the description has been mainly for a 2D flow field. Since the two dimensional Navier-Stokes equations have a turbulence behavior that can only be observed in 2D flows (good explained in [16] pp. 12 and 15), it is desirable to actually simulate in most cases a 3D flow field. There are actually two options possible for the spectral/hp method to implement a 3D flow field. On one hand it is possible to extend all coordinate systems by a third component - which then needs to be mapped appropriately. On the other hand, in case of a homogeneous geometry in the third dimension, it is possible to use a Fourier expansion for the resolution of the flow along this direction. In this case the boundary conditions on the sides of the third direction have to be periodic. This lead to an expansion base of

$$\phi_{mno}(a, b, c) = \phi_{mn}(a, b)\phi_o(c).$$

where o is the order of the expansion basis and c is the local coordinate, which is normed by the length of the homogeneous z-direction (L_{span}) as

$$c = \frac{2\pi z}{L_{span}}.$$

This leaves the basis function for the Fourier expansion to be

$$\phi_o(c) = e^{ioc}. \tag{2.11}$$

This method has been used throughout this work. Thus a complete description of the domain in three dimensions could be achieved. The method has some great advantages, but also some drawbacks we want to describe in the following.

2.2 Advantages and restrictions of the spectral/hp method

2.2.1 Advantages

The resolution is a major problem in CFD calculations. If no assumptions on the flow properties especially on turbulence, including turbulent kinetic energy

and dissipations are made, all processes in the flow need to be resolved by the simulation to obtain full knowledge of all flow variables over space and time. Such simulations are called direct numerical simulations (DNS). Generally this requires the resolution at Kolomgorovs dissipation scale $\eta = (\nu^3/\epsilon)^{\frac{1}{4}}$ - where ϵ is the dissipation rate and ν the kinematic viscosity. Since this resolution has to be regarded in three directions, a spacial resolution scaling of $\approx Re^{\frac{9}{4}}$ is needed. Nevertheless some simulations have show good agreements using DNS as a method, even though η was not fully resolved [17].
As there is no analytical way of determining the correct resolution in a flow field in advance, the correct resolution has to be determined "on the fly" in the simulation by analyzing the statistical properties. In case of a not sufficiently resolved flow field, the resolution has to be increased. At this point the spectral/hp method has one of its very strong points: Where other methods - such as finite volumes or finite differences (e.g. explained in [18]) need a time consuming remeshing procedure, for spectral elements only the polynomial order needs to be increased. Since accuracy does increase exponentially with the order, very fast convergence can be expected [8]. This makes the method very convenient for DNS simulations.

2.2.2 Drawback - the lack of geometrical flexibility

Even though the spectral/hp method has some decisive advantages (which are also often stressed by the developers of the $\mathcal{N}\varepsilon\kappa\mathcal{T}\alpha r$-code [19][8]) there are some drawbacks. One of them is the lack of geometric flexibility if very small properties within large structures are supposed to be resolved. The geometry of an object within the flow needs spatially to be resolved by the grid, while it is ideal to resolve most of the flow properties using the spectral method. This does lead to large gradients in the size of the elements of a grid and a very high spatial resolution at certain areas of the geometry if the polynomial order is constant through out the whole domain. One example is given in fig. 2.1 showing the trailing edge of the fx79w-151a airfoil analyzed in chapter 3 and 4. The triangle at the very tip of the tail has side lengths in the scale of 0.002 of the chord length L_c.

If the polynomial order is varied locally it is very difficult to achieve a locally sufficient resolution that avoids large gradients with the next elements. Since the accuracy within the elements is exponentially increased by the polynomial order, a well resolved flow easily becomes instable when it meets an areas of lower resolution. Therefore it is not a good option to lower the polynomial order in the boundary layer where the main problems with the grid due to the geometry appear.
The spacial resolution has an influence on the time stepping to be undertaken. If the time step chosen is too large, the spatial resolution does not capture the processes within the time step. Therefore the time step has to be adjusted to the local flow speed and the size of the elements. Typically the Courant-Friedrich-

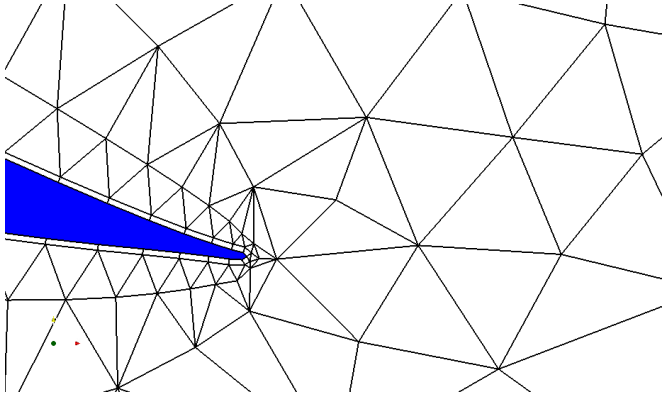

Figure 2.1: The geometrical structure of the airfoil that has been examined in this work includes a small pointed triangular trailing edge of the airfoil. This can only be resolved by very small elements, which leads to strong gradients in the surrounding element-sizes and resolutions.

Levy number (often referred to as CFL number) is used as a measure for the quality of the simulation and its potential stability [20]. It has to be kept low (see [18]). It is given by the maximum number of

$$CFL = \max\left(\frac{\Delta t u}{\Delta x}\right). \tag{2.12}$$

Here Δx is the spatial resolution within the domain, u the local velocity at the time and Δt is the time step. In spectral elements it is a bit more complicated as the spacial resolution is not only given by the grid, but also influenced by the polynomial order. In the $\mathcal{N}\varepsilon\kappa\mathcal{T}\alpha r$-code the CFL is calculated by

$$CFL_{Nek} = \max\left(\frac{u \cdot \Delta t}{\Delta a_{min} \cdot \Delta x}\right), \tag{2.13}$$

which is the maximum value from all the elements of the product of the local velocity and Δt divided by the product of Δa_{min} - the minimal distance in local non collapsed coordinates between two nodal points of the polynomials inside the element - Δx, which is the spatial extension of the element.
Therefore the size of the elements does have a decisive influence on the size of the time steps and thus on the calculation time. If the geometry enforces unusual small resolutions, the time steps Δt decrease proportionally. This problem is enhanced due to the sensitivity of the method to resolution deficiencies.

2.2.3 The sensibility to resolution

One of the at a first sight unpleasant features of the $\mathcal{N}\varepsilon\kappa\mathcal{T}\alpha r$-code is that the simulations of 3D flows become easily unstable. One of the main reasons for this

lays in the implementation of the so called "collapsed" coordinate system [8] as given by equation (2.5). Fig. 2.2 demonstrates basically what the mapping from the rectangular to the triangular space does: Point C is merged with point D (that's why it is called collapsed system). The system maps the vertical lines in the rectangular system to merge in the one point $D = C$. To optimize the distribution of the points of the polynomial calculation usually the Lebesgue constant or Fekete points are being calculated, which is a broadly discussed topic (see e.g. [21][22]). However, it seems that distribution of the so called quadrature points in the triangles follow a procedure of collapsing coordinates, which leads to a high resolution in the region of the merged points in contrast to the areas of non merged points.

In the simulations done during this research it was observed that this non-

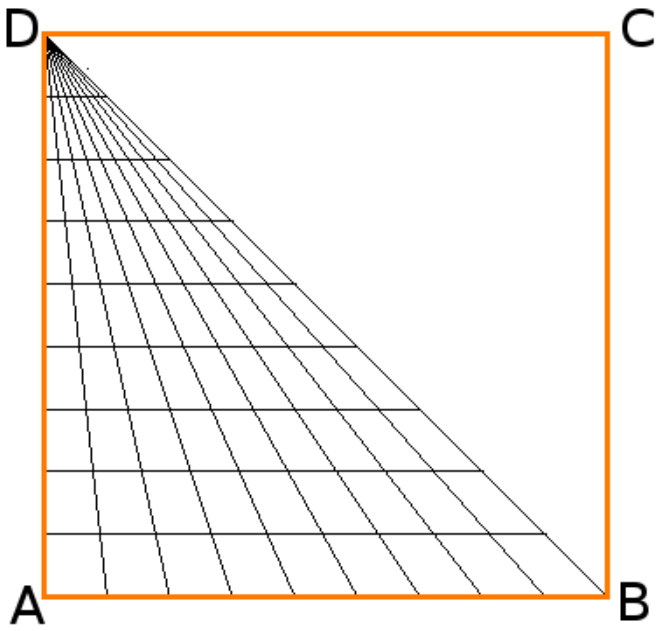

Figure 2.2: Geometrical resolution due to mapping of the rectangular points onto a triangular space.

homogeneity triggers instabilities in situations of an under resolved flow field. In cases of a main flow direction in a turbulent field traveling from a collapsed element onto an area of a non collapsed element, there might be a sharp drop of spatial resolution. In situations of a decaying turbulence when the well resolved collapsed region is able to resolve a suddenly appearing small scale turbulence, the following non collapsed region might not have the spacial resolution to resolve the scales anymore. This leads quite frequently to instabilities as shown in fig. 2.3, which shows an unphysical pressure drop due to the resolution gradient at the boundary between two elements shortly before complete divergence. However

as Moin et. al. mentioned [17] a not completely to the dissipation scale resolved simulation might also lead to decent results. In some cases some regions might not need to be completely resolved, since the result in such regions might not be of any interest. With the method of collapsed coordinate systems this does not work.
It should also be noted that the determination of Fekete points and the Lebesgue constant is always focused on the optimal resolution within a single element. In spectral elements however an optimized resolution over the whole domain or at least in certain local regions consisting of many elements is needed. Further research in this field will therefore be necessary in the future.
The effect of such instabilities does not seem to appear so easily in case of pure 2D

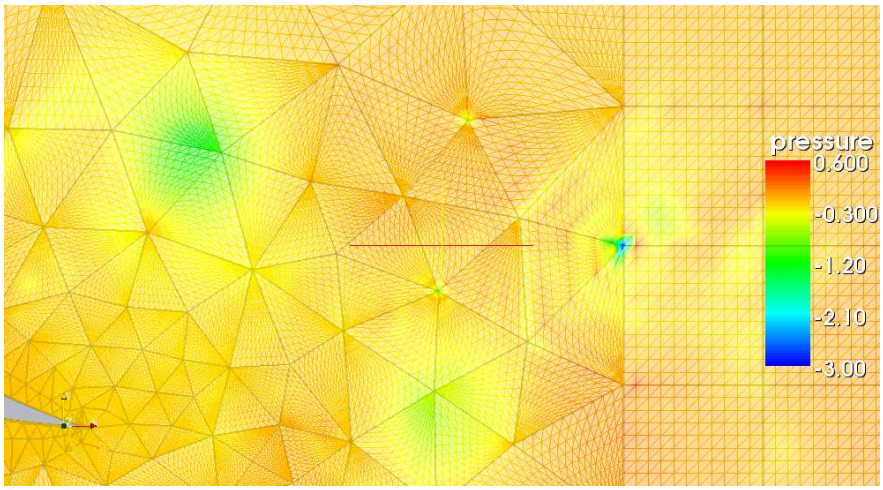

Figure 2.3: Pressure values in an unstable situation at the transition of a collapsed triangle onto a quadrilateral region, leading to unphysical pressure values. In the backround the grid of the polynomial nodal points is shown.

simulations. As described by Mathieu et. al. [16] there is no convective stretching of vortices in pure 2D calculations. This leads to the effect that the vortices do not decay, but due to the inverse turbulent cascade tend to merge with other vortices [23]. Thus the tendency of having to resolve smaller turbulent structures as the flow propagates on is not as strong. As a result a simulation might very well run stable on a certain resolution in 2D whereas in 3D the simulation becomes instable.
On the other hand the instabilities are a good indicator to check if the flow field is well resolved in regions of collapsed coordinates. Further the instabilities are enhanced due to the tendency to unphysical gradients at the edges of the elements.

2.2.4 Gradients of the velocity in the fields

The spectral finite element method utilizes a neat way to ensure C^0 continuity. However this is not the case for C^1. This is for the investigation of the physical turbulent effects in flow fields on or around every object a drawback. Vorticity and vortices are in fluid dynamics important aspects for the research on the actual physical processes in a flow [24][25][26]. Their mathematical description depends on gradients in the flow field and thus on the C^1 structure. However, the implementation of the Jacobi polynomials with the decomposition into vertex, boundary and interior modes does obviously sometimes lead to strong gradients in the derivatives of the velocity. This becomes obvious when regarding the vorticity as shown in fig. 2.4. At the edges of the elements a steep gradient can be observed - especially, but not only - in cases of a turbulent flow, containing strong gradients in itself.

Since vortices are a source of pressure fluctuations, the knowledge of their struc-

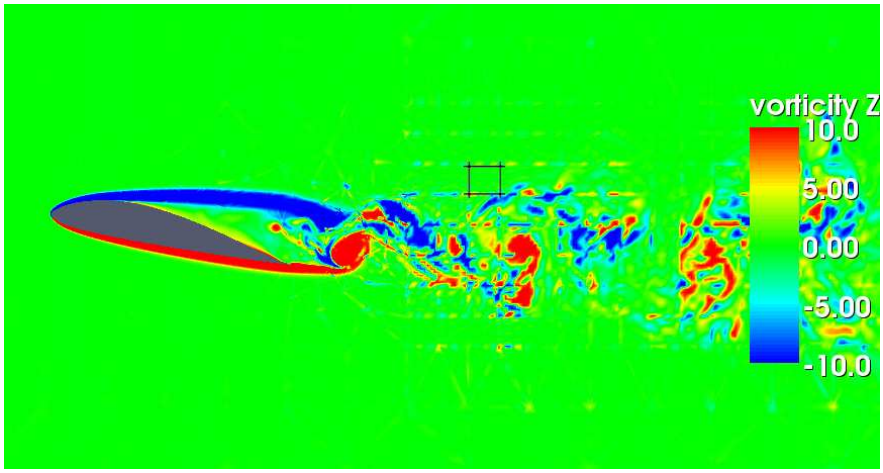

Figure 2.4: Contours of the vorticity in z-direction of the flow around an airfoil at Re=5000. The contours of single elements can clearly be seen. In black a single element is depicted to clearify the grid structure in the wake.

ture, progress and decay is important in aerodynamics. In the recent years the λ_2 criterion has been established to describe the vortices in a fluid flow [24]. For the description of flows using finite spectral elements, as used here, the method is however hardly used (so far only one exception is know to the author which is at a simulation of a curved pipe at Re=100 [27]). The reason is assumed to be in the structure of λ_2 and the problem with velocity gradients. To explain this the derivation of λ_2 shall be described here in a short excursus which refers to Jeong et. al. [24].

Excursus λ_2 criterion

To analyze a flow field in a reliable and meaningful manner is not a trivial topic. One of the main interests in a flow field is the existence and behavior of vortices in the flow. The problem however has been for a long time the question of a reliable definition of a vortex. Definitions of vortices by pressure minima or vorticity magnitude have some restrains as cases exist for either method, where they fail to be applicable. In case of the pressure criterion these are e.g. the Stokes flow or Karmans viscous pump in steady flows. In strong shear flows however the vorticity method fails, since the strong shear might conceal an existing vortex. Therefore Jeong and Hussain proposed the so called λ_2 method as a criterion [24]. First we can take the gradient of the Navier-Stokes equations (1.4), leading to

$$\partial_j a_i = -\frac{1}{\rho}\partial_i\partial_j p + \nu\partial_i\partial_k\partial_k u_i. \tag{2.14}$$

Here $\partial_j a_i$ is the acceleration gradient. Now, we can decompose $\partial_j a_i$ into a symmetrical and an antisymmetrical part:

$$\partial_j a_i = [\frac{DS_{ij}}{Dt} + \Omega_{ik}\Omega_{kj} + S_{ik}S_{kj}] + [\frac{D\Omega_{ij}}{Dt} + \Omega_{ik}S_{kj} + S_{ik}\Omega_{kj}].$$

Here Ω is given by:

$$\Omega_{ij} = \begin{pmatrix} 0 & \partial_x u_y - \partial_y v_x & \partial_x u_z - \partial_z w_x \\ \partial_y v_x - \partial_x u_y & 0 & \partial_y v_z - \partial_z w_y \\ \partial_z w_x - \partial_x u_z & \partial_z w_y - \partial_y v_z & 0 \end{pmatrix}. \tag{2.15}$$

The symmetrical tensor is:

$$S_{ij} = \begin{pmatrix} 2\partial_x u_x & \partial_x u_y + \partial_y v_x & \partial_x u_z + \partial_z w_x \\ \partial_y v_x + \partial_x u_y & 2\partial_y v_y & \partial_y v_z + \partial_z w_y \\ \partial_z w_x + \partial_x u_z & \partial_z w_y + \partial_y v_z & 2\partial_z w_z \end{pmatrix}. \tag{2.16}$$

The symmetrical part of equation (2.14) can now be rewritten as

$$\partial_j a_i = \frac{DS_{ij}}{Dt} - \nu\partial_k partial_k S_{ij} + \Omega_{ik}\Omega_{kj} + S_{ik}S_{kj} = -\frac{1}{\rho}\partial_i\partial_j p. \tag{2.17}$$

For the analysis of vortices, now the first two terms in equation (2.17) can be neglected. Jeong and Hussain define now a vortex core "*as a connected region with two negative eigenvalues of* $S^2 + \Omega^2$" [24].
As $S^2 + \Omega^2$ is a symmetric matrix, the eigenvalues $\lambda_1, \lambda_2, \lambda_3$ are real and $\lambda_1 \geq \lambda_2 \geq \lambda_3$. Therefore, to fulfill the criterion of two negative eigenvalues, it is sufficient that $\lambda_2 < 0$. This is called the λ_2 criterion, which is by now widely used for vortex analysis.

The eigenvalues of $S^2 + \Omega^2$ however contain products of four velocity derivatives. Thus the deviations on the edges of the elements are amplified considerably. A plot of a λ_2 plane shows very easily just non physical artefacts (see fig. 2.5). Therefore the λ_2-criterion is usually not the method that can be applied to evaluate the vortex structure in turbulent flows in the used spectral finite element application and will not be used throughout the rest of this thesis. Instead to depict vorticity structures the use of pressure minima and in one case the pure vorticity will be used.

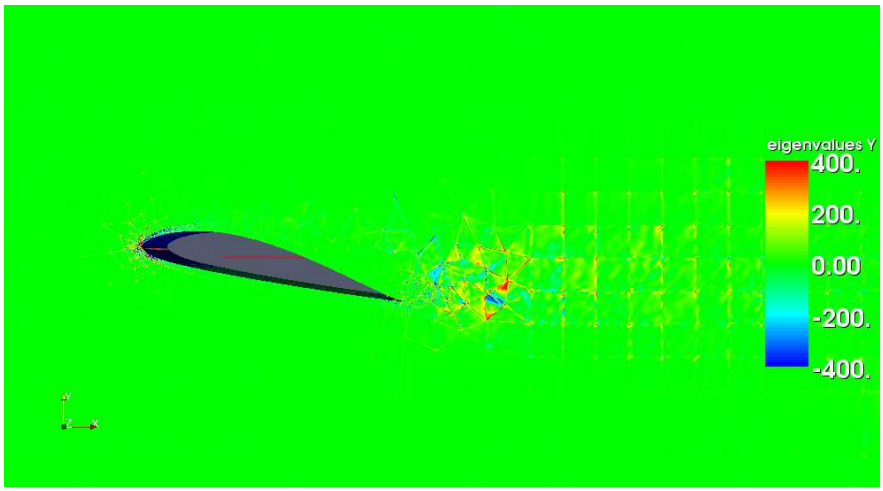

Figure 2.5: Contours on the surface for λ_2 for the same situation as given in fig. 2.4.

2.2.5 Spanwise parallel decomposition accuracy

The simulations using the spectral/hp method can be quite costly in terms of computational time. Therefore the code has been parallelized. This is done by the decomposing the flow field by using a Fourier expansion in the homogeneous direction [28]. Thus we can use equation (2.11) for the expansion of the velocity fields

$$u_i(a,b,c,t) = \sum_{o=0}^{M-1} u_{io}(a,b,t)e^{ioc}. \tag{2.18}$$

Taking the Fourier transform of the momentum equation (1.10) and using the abbreviations in equations (2.11) we obtain an equation for the coefficients $u_{i,o}$ for each moment o

$$\partial_t u_{io} = -\partial_i p_o + \frac{1}{Re} L_o(u_{io}) - FFT_m[N(u_i)] \quad \text{in} \quad \Omega_o, o = 0, ..., M-1 \tag{2.19}$$

Here $FFT_m[N(u_i)]$ is the Fourier transform of the non linear parts of the momentum equation. While

$$\partial_i = \left(\frac{\partial}{\partial x}, \frac{\partial}{\partial y}, ioc\right),$$
$$L_o(u_{i,o}) = \left(\frac{\partial^2}{\partial x^2} + \frac{\partial^2}{\partial y^2} - oc\right)$$

are pretty much straight forward. It is very plausible to set the computational domain Ω_m for now as a x-y slice of the complete domain Ω. Therefore the only coupling between the different modes functions via the non linear term. This way the computation of the different modes o are done independently from another. The calculation is done as a set of possibly M parallel computations [28].

Looking at the results of a simulation in the spanwise direction, a strange phenomenon can be perceived: The results of the Fourier planes that have been calculated by one core on a computer align very well together. However towards the neighboring planes at different cores there is a recognizable deviance. Fig. 2.6 shows the correlation of the u-velocity in spanwise direction in a laminar region calculated once using 16 cores[1] a) and once using 4 cores[2] b). The extreme jumps in the correlation can be explained by the laminar flow, resulting in a field with very small velocity fluctuations and a standard deviation in the order of 10^{-3}. Thus the correlations are governed by small fluctuations in the velocity field.

The phenomenon can even be seen in the averaged velocity flow over a period of time and is independent of different versions of the code (see fig. 2.7). Even though the quantitative differences are slim, the deviances are recognizable if the field is analyzed statistically. The "jumps" in the averaged velocity profile show a magnitude in the laminar flow situation of up to 0.04% of the velocity itself.

The source of the problem is yet not clear. The simulations throughout this work were all done using a dealiasing option in the code for the Fourier expansion to solve problems with under-integration. Without the dealiasing turbulent calculations became quickly unstable. The option increased the order artificially by a factor of 3/2. However this does not explain, why the simulation in spanwise direction is dependent on the number of calculating cores. The impression is rather that it might be an intrinsic effect of the communication between the cores.

So far this phenomenon is not mentioned in the main publications concerned with the code. One reason for this might be, that it is most efficient to split

[1]For the 16 core calculation the Paris Cluster of the University of Hannover was used. Specifications could be (in 2009) found in http://www.rrzn.uni-hannover.de/paris.html

[2]This calculation was done on an AMD Phenom Quad core processor

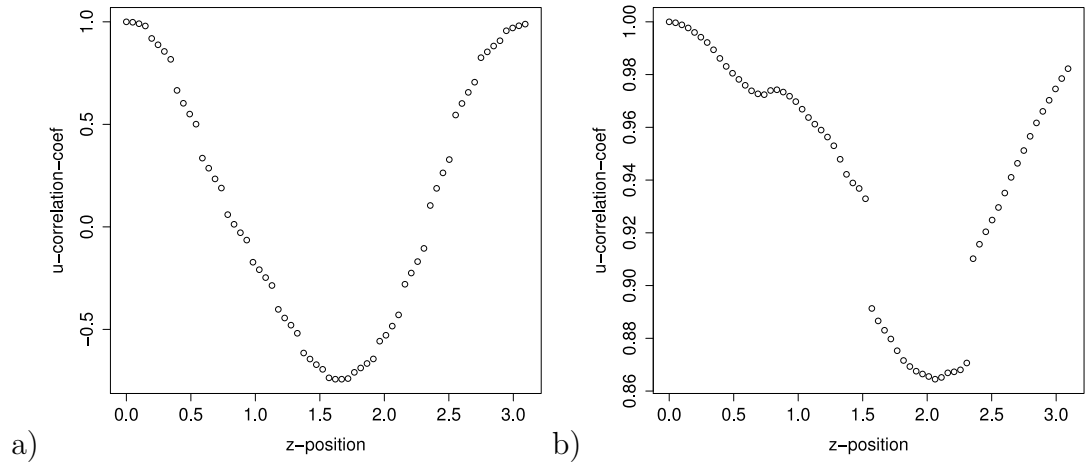

Figure 2.6: Correlation of the u-velocity along the spanwise direction. The left hand figure a) shows the correlation for a time series of t=3 calculated with 16 processors for 64 Fourier planes. In b) a calculation has been done for a time series of t=5 computed on 4 processors. The amount of Fourier planes calculated by one processor can clearly be seen.

the calculation in a way, that each core calculates one plane. This procedure is also suggested by Crawfort et. al. [28] and Dong et. al. [14]. Following this procedure this phenomenon will never surface. So further research is needed to clarify the reasons.

2.3 Conclusions

The method of using spectral methods for finite elements has become quite an advanced technique. It has been very successful in different fields at low Reynolds numbers. However, it remains an open question how good the accuracy is in the spanwise direction if a Fourier expansion is used on parallel computing. Additionally the use of the code should be very well prepared and adapted to the geometrical setting. Otherwise the calculations become very expensive in terms of computational cost.
Nevertheless the method is very convincing especially due to the fast convergence and the absence of the need of remeshing in case of a change in resolution.

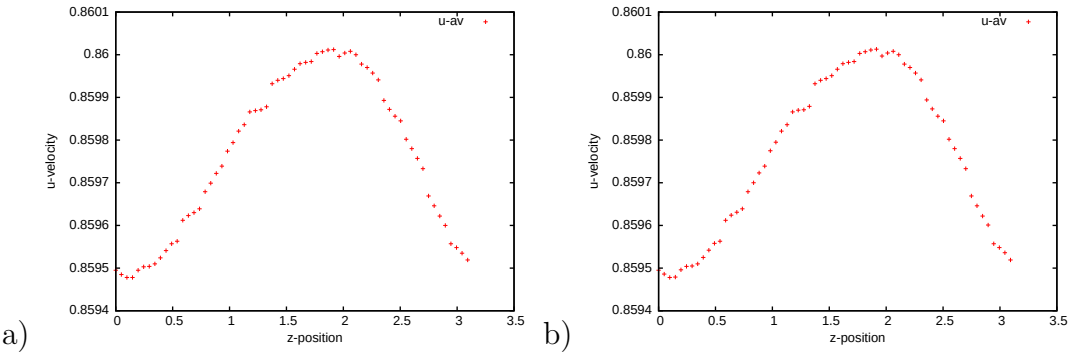

Figure 2.7: Average velocity along the spanwise direction at the same point calculated by two different versions of the code. The old version from 2002 is in a), an new one including a body motion option from 2008 is given in b).

Bibliography

[1] George Em Karniadakis and Spencer J. Sherwin. *Spectral/hp Element Methods for Computational Fluid Dynamics*. Numerical Mathematics and Scientific Computations. Oxford University Press, 1. edition, 1999.

[2] Rupad Darekar and George Em Karniadakis. Flow past a square-section cylinder with a wavy stagnation face. *J. of Fluid Mech.*, 426:263–295, 2001.

[3] Bruno Souza Carmo, Julio Romano Meneghini, Paulo Jose Saiz Jabardo, and Fabio Saltara. Investigation of the flow around two circular cylinders employing the spectral element method with modal decomposition. In *Proceedings of OMAE04*, 23rd International Conference on Offshore Mechanics and Arctic Engineering, jun 2004.

[4] I. V. Pivkin, E. Hueso, R. Weinstein, D. H. Laidlaw, S. Swartz, and George Em Karniadakis. Simulation and visualization of air flow around bat wings during flight. In *International Conference on Computational Science*, pages 689–694, 2005.

[5] S. Dong, George Em Karniadakis, and Nicholas T. Karonis. Cross-site computations on the teragrid. *Computing in Science and Engineering*, pages 14–23, sep/oct 2005.

[6] Robert M. Kirby and George Em Karniadakis. De-aliasing on non-uniform grids: algorithms and applications. *Journal of Computational Physics*, 191, 2003.

[7] X. Ma, G.-S. Karamanos, and G.E. Karniadakis. Dynamics and low-dimensionality of a turbulent near wake. *Journal of Fluid Mechanics*, 410:29–65, 2000.

[8] George Em Karniadakis and Spencer Sherwin. *Spectral/hp Element Methods for Computational Fluid Dynamics*. Numerical Mathematics and Scientific Computations. Oxford University Press, Oxford, 2nd edition, 2005.

[9] Tim Warburton, Spencer J. Sherwin, and George Em Karniadakis. Basic functions for triangular and quadrilateral high-order elements. *Journal of Scientific Computing*, 20(5):1671–1695, 1999.

[10] I. Lomtev, C.B. Quillen, and George Em Karniadakis. Spectral/hp methods for viscous compressible flows on unstructured 2d meshes. *Journal of Computational Physics*, 144:325–357, 1998.

[11] J. Proriol. Sur une famille de polynomes a deux variables orthogonaux dans un triangle. *C.R. Acad. Sci Paris*, 257:2459–2461, 1957.

[12] T. Koornwinder. *Two-variable analogues of the classical orthogonal polynomials*. Academic Press, San Diego, 1975.

[13] Moshe Dubiner. Spectral methods on triangles and other domains. *Journal of Scientific Computing*, 6(4):345–390, 1991.

[14] S. Dong and George Em Karniadakis. P-refinement and p-threads. *Computational Methods in Apllied Mechanical Engineering*, 192:2191–2201, 2003.

[15] George Em Karniadakis, S. A. Orszag, and M. Israeli. High-order splitting methods for the incompressible navier-stokes equations. *Journal of Computational Physics*, 97:414–443, December 1991.

[16] Jean Matieu and Julian Scott. *An Introduction to Turbulent Flow*. Cambridge University Press, 1 edition, 2000.

[17] Parviz Moin and Krishnan Mahesh. Direct numerical simulation: A tool in turbulence research. *Annual Reviews in Fluid Mechanics*, 30:539–578, 1998.

[18] Joel H. Ferziger and Milovan Peric. *Computational Methods for Fluid Dynamics*. Spinger, 3. edition, 2002.

[19] Robert M. Kirby, Tim Warburton, Spencer J. Sherwin, A. Beskok, and George Em Karniadakis. *Dynamic Simulations without Remeshing*, volume 397-1 of *Computational Technologies for Fluid/Thermal/Structural/Chemical Systems with Industrial Apllications*. ASME, 1999.

[20] R. Courant, K. Friedrichs, and H. Lewy. On the partial difference equations of mathematical physics. *IBM Journal*, pages 215–234, March 1967.

[21] Wilhelm Heinrichs. Improved lebesgue constants on the triangle. *Journal of Computational Physics*, 207:625–638, 2005.

[22] Richard Pasquetti and Francesca Rapetti. Spectral element methods on triangles and quadrilaterals: comparisons and applications. *Journal of Computational Physics*, 198:349–362, 2004.

[23] G. Maze, Xavier Carton, and G. Lapeyre. Dynamics of a 2d vortex doublet under external deformation. *Regular and Chaotic Dynamics*, 9(4):477–497, 2004.

[24] Jinhee Jeong and Fazle Hussain. On the identification of a vortex. *J. of Fluid Mech.*, 285:69–94, 1995.

[25] L.P. Bernal and A. Roshko. Streamwise vortex structure in plane mixing layers. *J. Fluid Mech.*, 170:499–525, 1986.

[26] C. H. K. Williamson. Vortex dynamics in the cylincer wake. *Annual Reviews in Fluid Dynamics*, 28:477–539, 1996.

[27] Anthi Miliou, Spencer J. Sherwin, and J. Michael R. Graham. Fluid dynamic loading on curved riser pipes. *Journal of Offshore Mechanics and Arctic Engineering*, 125(3):176–182, 2003.

[28] Catherine H. Crawfort, Constantinos Evangelinos, David Newman, and George Em Karniadakis. Parallel benchmarks of turbulence in complex geometries. *Computer and Fluids*, 25(677), 1996.

Chapter 3

Direct numerical simulation of the turbulent flow around an airfoil using spectral/hp method[1]

Since the accuracy of Reynolds Averaged Numerical Simulations (RANS) is limited considering turbulence effects, we applied a spectral/hp element method to predict the turbulent flow separation at an airfoil for an angle of attack of 12^o. The spectral/hp [1] approach allows to solve the incompressible Navier-Stokes equation with spectral accuracy on unstructured grids by means of Direct Numerical simulation (DNS). Here we present first results we obtained from DNS of the flow around a fx79-w151a airfoil section for a low Reynold Number $Re = 5 \cdot 10^3$.

3.1 The task of the flow simulations on airfoils

The technology of wind turbines for generation of sustainable energy has made a lot of progress in the last 10 years. Yet, due to the strong effect of turbulence in the wind field, predicting the aerodynamic characteristics of wind turbines is still a challenging job to do. Sudden changes in the angle of attack caused by atmospherical turbulences lead to effects such as dynamic stall. Since the numerical simulation of aerodynamic loads under dynamic stall conditions is still difficult, manufacturers of wind turbines rely on estimations calculating the maximum loads on turbine airfoils. Therefore it is an important task to evaluate the

[1]Published as B. Stoevesandt, A. Shishkin, C. Wagner and J. Peinke: *Direct Numerical Simulation of the Turbulent Flow Around an Airfoil* in European Conference on Computational Fluid Dynamics ECCOMAS CFD 2006, edited by P. Wessling, E. Onate, and J. Periaux, ISBN 90-9020970-0, 2006

real loads appearing on a blade in turbulent flow.
Numerical simulations based on the solution of the RANS equation rely on turbulence models, which often have difficulties in predicting accurately all required details of the turbulent effects [2]. Therefore Large Eddy Simulations (LES) and Direct Numerical Simulations (DNS) have become more interesting during the last years as computational power is increasing. Using DNS for airfoil simulations is - due to the still high computational costs at higher Reynolds numbers - not very common. Some groups involved in the research of computational fluid dynamics (CFD) have therefore started to apply LES codes for airfoil flow problems [3][4]. The results have been mostly promising, yet predicting special turbulent effects on airfoils remains a difficult topic. The LESFOIL project [4] showed, that predicting the leading edge and trailing edge flow correctly is difficult and strongly depends on the mesh resolution and its topology. While the simulation at high Reynolds numbers has been difficult, some groups have turned to simulate the flow for lower Reynolds numbers to start off with [3][5][6]. At lower Reynolds number nevertheless DNS becomes an option for simulation again, since its accuracy is still to be higher.
In the present work flow simulations at low Reynolds number were performed by means of DNS and will be compared to the results of the corresponding LES in the future (for the LES results see [7]).
Facing these tasks we employed a spectral/hp code to simulate the turbulent flow around an airfoil [1][8]. The advantage of this code is, that it allows a great flexibility solving that kind of problems with a minimum of costly remeshing. A DNS and a LES solver are implemented in the code, which will allow us a direct comparison in the future. In a first step presented here, the first results obtained with the DNS solver are analysed.

3.2 Numerical Method

As we are considering airfoils for the use on wind turbines and therefore low velocities, it is sufficient to use a calculation for incompressible flow. In this case the flow of the air can be considered as an incompressible Newtonian fluid flow, which can be described by the dimensionless Navier-Stokes equations:

$$\frac{\partial \mathbf{u}}{\partial t} + (\mathbf{u} \cdot \nabla)\mathbf{u} = -\nabla p + \nu \Delta \mathbf{u} + \mathbf{F} \tag{3.1}$$

$$\nabla \cdot \mathbf{u} = 0 \tag{3.2}$$

where $\mathbf{u}$ denotes the velocity, p the pressure, $\mathbf{F}$ the forces and ν the kinematic viscosity. The velocity $\mathbf{u}\,|_{\partial\Omega} = 0$ at on the airfoil.

The spectral/hp method is an attempt to combine the flexibility of finite element or volume methods with the accuracy of spectral methods[1]. The domain

is divided into an unstructured grid that can be adapted to the problems faced. For each of the elements E the spectral method is being applied. A polynomial basis $\Phi_{lm}(r,s)$ is defined to approximate the function $f(r,s)$ for each element E with $(r,s) \in E$:

$$u(r,s) = \sum_l \sum_m \bar{u}_{lm} \Phi_{lm}(r,s) \tag{3.3}$$

Where $\bar{u}_{lm}$ are the expansion coefficients for the polynomial Φ and (r,s) are local coordinates the Element E. This way the polynomial order to calculate every element of the grid can be changed. Jacobi polynomials P are used for the expansion P. So a triangular orthogonal expansion basis for $(r,s) \in E = \{-1 \leq r,s; r+s \leq 0\}$ can be setup as

$$\Phi_{lm}(r,s) = P_l^{0,0}(2\frac{(1+r)}{(1-s)} - 1)(1-s)^l P_m^{2l+1,0}(s) \tag{3.4}$$

To evaluate the calculations a transformation from triangular to rectangular space is being done [9][10].
This principle can be applied for both, the DNS and the LES, technique. The spectral/hp code $\mathcal{N}\varepsilon\kappa\mathcal{T}\alpha r$ was used in the current project. The code is parallelized using MPI.

3.3 Simulation Parameters

The effects of dynamic stall are investigated using a fx79-w151a profile mainly developed for the use on wind turbines. In spanwise direction the profile is to be homogeneous. This profile is being investigated under submission of a shortly disturbed laminar inflow at a Reynolds number of $Re = 5000$ in respect to the chord length L_c at an angle of attack of $\alpha = 12^o$. In Fig. 3.1 a plot of iso surfaces of the velocity in z-direction is presented in order to give an impression of the dimensions of the blade segment.

A computational domain expands from -$15L_c$ in the inflow to $30L_c$ in the outflow direction and from -$15L_c$ to $15L_c$ in cross-flow direction. A periodic boundary condition was chosen for the outer boundary of the domain in cross-flow direction. A Fourier expansion was used along the homogeneous spanwise direction. The spanwise length was set to be πL_c.
The simulation was performed on a grid using K=1954 elements. Fig.3.2 shows a 'z-slice' of the domain and some detailed sections of the mesh around the airfoil as well as the leading and trailing edge. The mesh was generated using the mesh generator gmsh [11]. For a better results in the vicinity of the trailing edge the resolution of the grid was increased in this region. To further improve the resolution in the vicinity of the wall an additional layer of elements was introduced with a mesh size at the wall of $\Delta y^+ \leq 7.2$. Such a Δy^+ value seems rather coarse

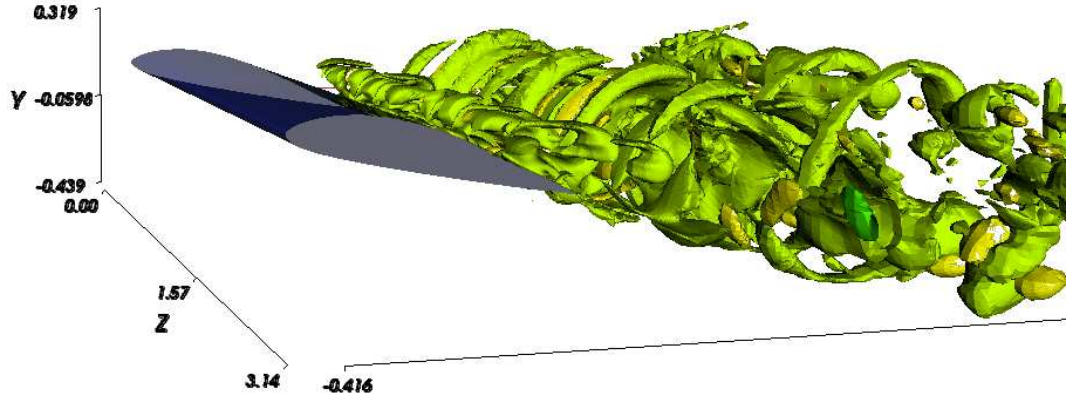

Figure 3.1: Contour-Plot of the velocity in z-direction on the fx79-w151a airfoil. The units on the axis show are given in chord length L_c.

for a DNS, but it cannot be compared to a Δy^+ value used in a finite volume method, since the accuracy in spectral/hp is not only dependent on the mesh size, but on with the polynomial order. Around the airfoil the polynomial order used was $P = 9$. As the error decreases exponentially with an increase of the polynomial order (see [1]), the effective Δy^+ is ≤ 1.
Finally, in the spanwise direction, 64 Fourier planes were used in our DNS.

At the beginning the polynomial order P used in our DNS was set to 5. Together with the number of elements and Fourier planes, this lead to about 1,300,000 degrees of freedom, which was still to low for a well resolved simulation (compare e.g. [8]). As the number of elements was already quite large for the spectral/hp method for such a problem, the polynomial order was varied for the following simulation throughout the domain. Tab.3.1 reflects the areas of the different polynomial orders and the number of elements calculated using these orders. This approach increased the number of degrees of freedom to about 3,570,000. The density of degrees of freedom per volume units varies strongly from the order between 10^7 to 10^5 at the foil to the order of 1 on the outer area of the domain.
Since the polynomial order was varied, also the time stepping was varied during the simulation between time steps of $0.5 \cdot 10^5$ and $2.5 \cdot 10^5$ in dimensionless time units. This way the CFL value was reaching 0.35 in a maximum.

3.3.1 Computational Performance

The computations were performed using 16 processors on the CLUH-Cluster of the RRZN Hannover a 16 MEGWARE Saxonid C4 Compute-Knot Quad-Processor-System and on a 64 bit Opteron Linux-Ethernet Cluster at the Uni-

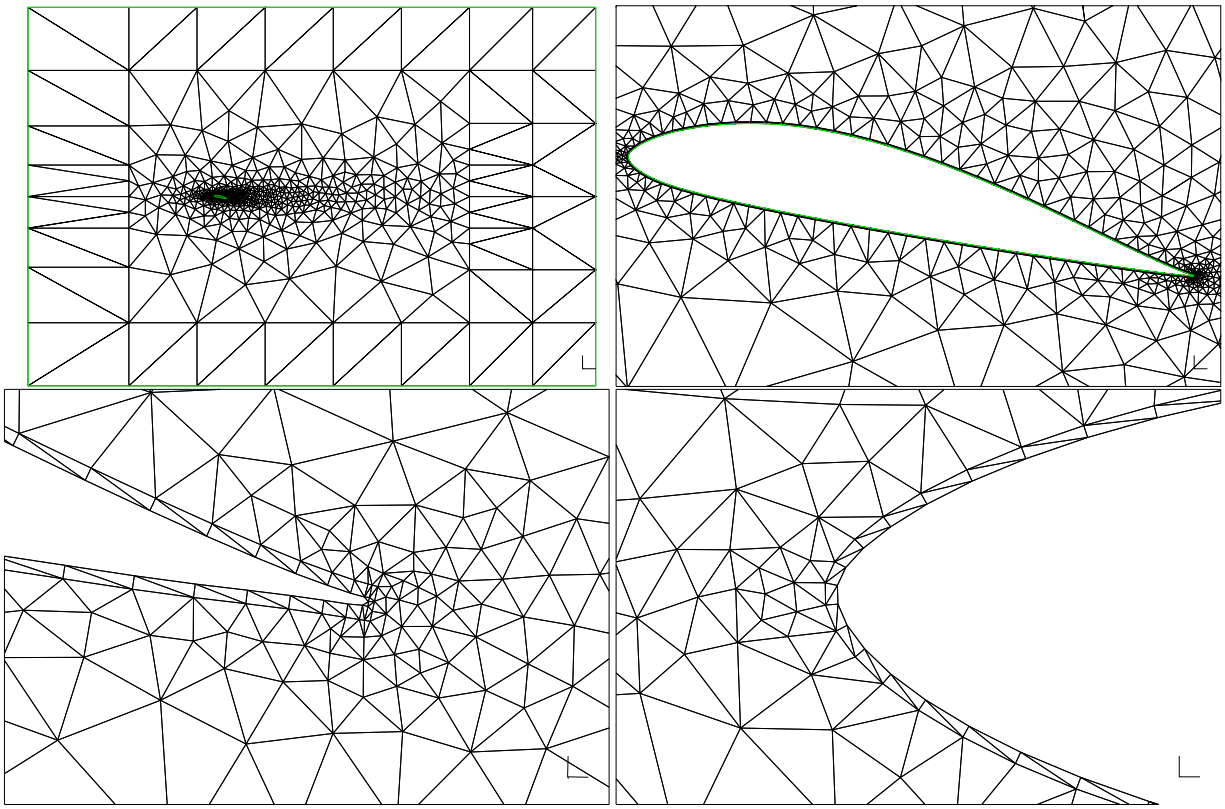

Figure 3.2: Grid in the (x,y)-plane consisting of 1954 elements (top left). The density of elements was strongly increased at tip and tail of the airfoil.

Area	Top right point of area	Low left point of area	P	Number of Elements
Rest Domain	(30,15)	(-15,-15)	5	690
Foils surrounding	(1.1,0.4)	(-0.4,-0.25)	9	1003
Near wake	(5.7,1)	(1.1,-0.6)	7	261
Airfoil	(0.76, -0.16)	(-0.22,0.046)	0	0

Table 3.1: Areas of certain polynomial orders in respect to airfoil position.

versity of Oldenburg. In Fig.3.3 the speed-up obtained at the CLUH-cluster is presented. The linear speed-up underlines the good parallel performance of the used code.

3.4 First Results

The forces in $\mathcal{N}\varepsilon\kappa\mathcal{T}\alpha r$ are calculated as

$$F = -\int_s Pnds + \int_s \tau \cdot nds. \tag{3.5}$$

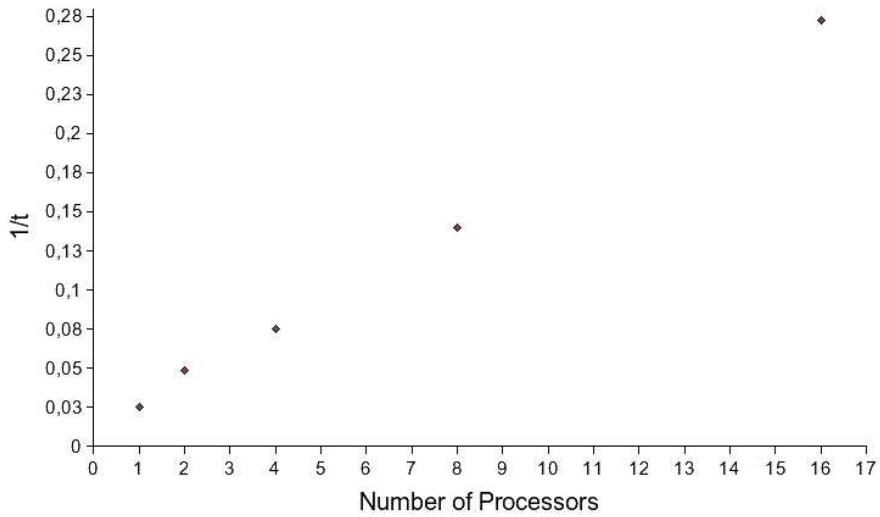

Figure 3.3: Needed averaged inverse computational time per time step over the number of processors. Doubling the number of processors from 8 to 16 still increases the performance by 95%.

The first time variations of lift and drag we obtained are shown in Fig. 3.4 and Fig. 3.5. The plots in Fig. 3.4 display the drag and lift forces over a short period of time. It shows the response of the lift and drag to the turbulent flow separation at the blade. So far the average values of the lift and drag coefficient are $C_l = 0.77$ and $C_d = 0.2$. In Fig. 3.5 contours of the u- and v-velocity are

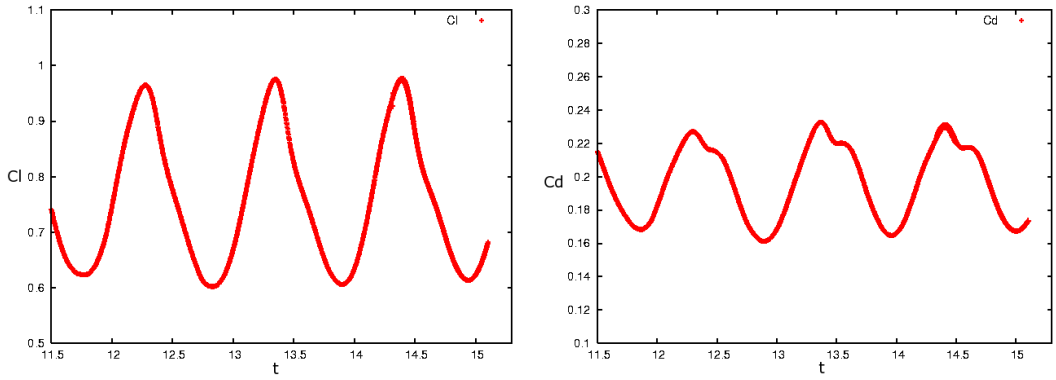

Figure 3.4: Lift (left) and drag (right) for the airfoil over dimensionless time at $Re = 5 * 10^3$ and $\alpha = 12^0$. As the Reynolds number is low, the fluctuations are slow.

presented at a (x,y)-plane cut. A flow separation can be observed in the region of $x/L_c = 0.3$. Fig. 3.6 shows a course of the vortice separation at the trailing edge by pressure contours. In order to perform a detailed statistical evaluation of the flow field, we are continuing the computation in order to present the results

at the conference.

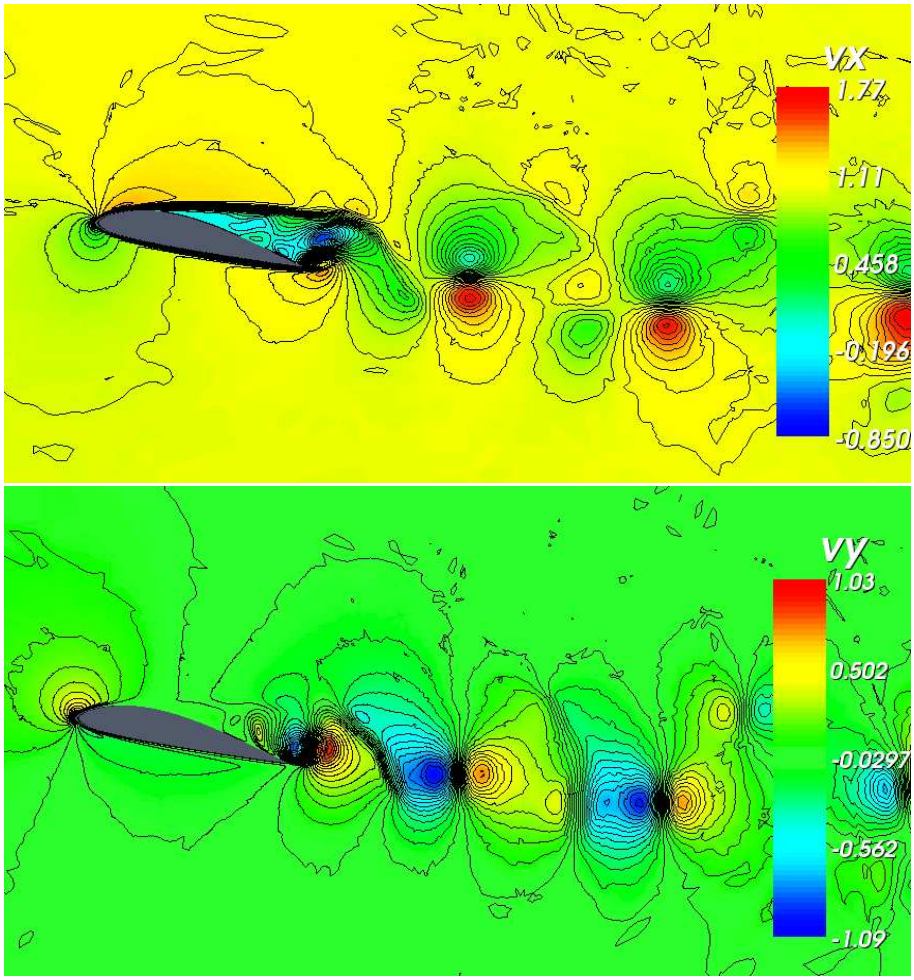

Figure 3.5: Contours of u-velocity (top left), v-velocity(top right) in a (x,y)-plane cut.

3.5 Conclusions

Using the spectral/hp method is due to its flexibility very practical for simulating turbulent flow. Especially the possibility of locally increasing accuracy by increasing the polynomial order in certain grid elements without the need of remeshing has been very useful. A mesh consisting of few elements can thus still be used for high accuracy calculations. Thus it seems to be possible to increase the Reynolds number for further flow simulation on the airfoil even using DNS, since the accuracy can be easily increased.
The first results show the turbulent flow and a small flow separation region at the trailing edge. A verification of the simulation is to be done in the future. So far

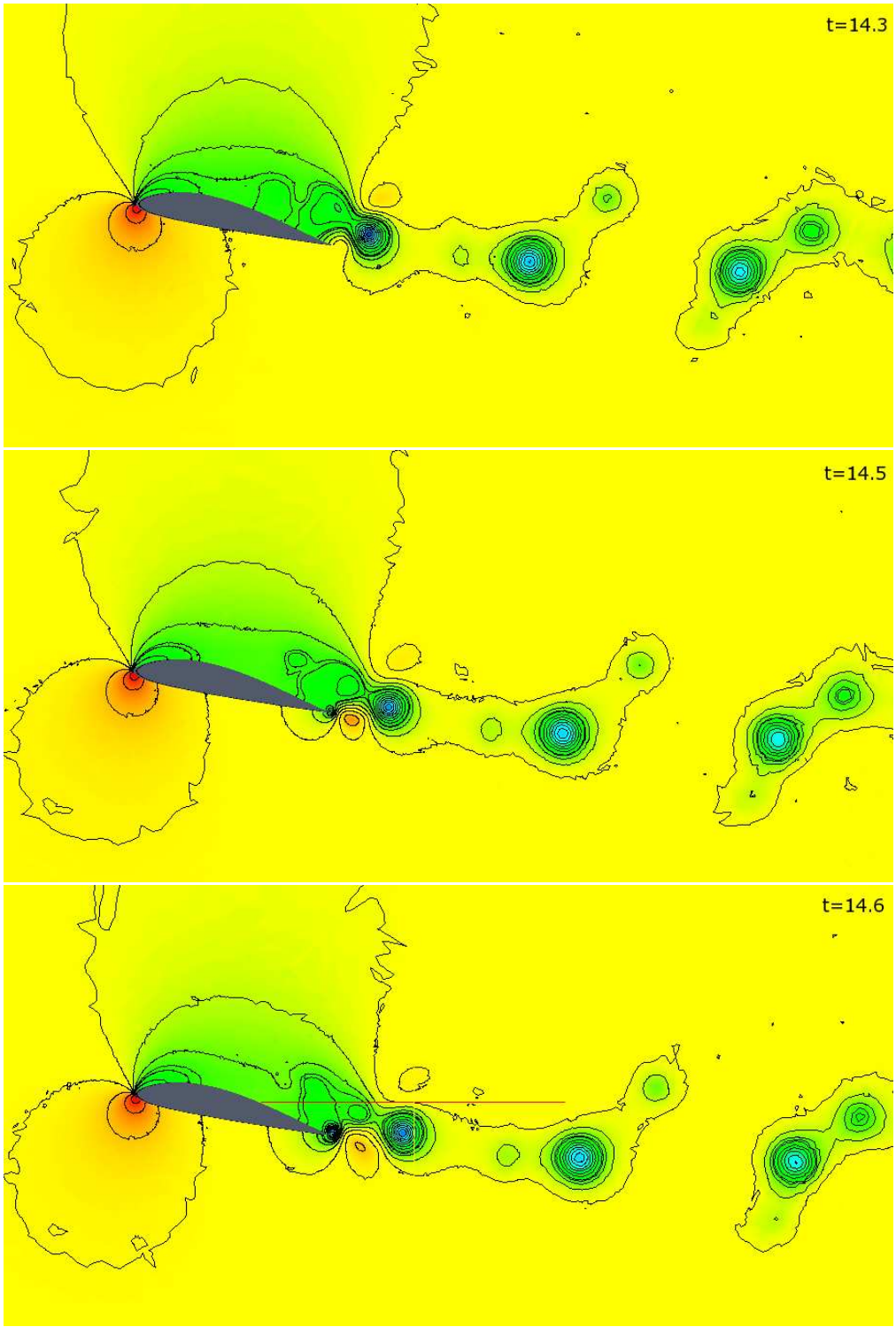
t=14.3
t=14.5
t=14.6

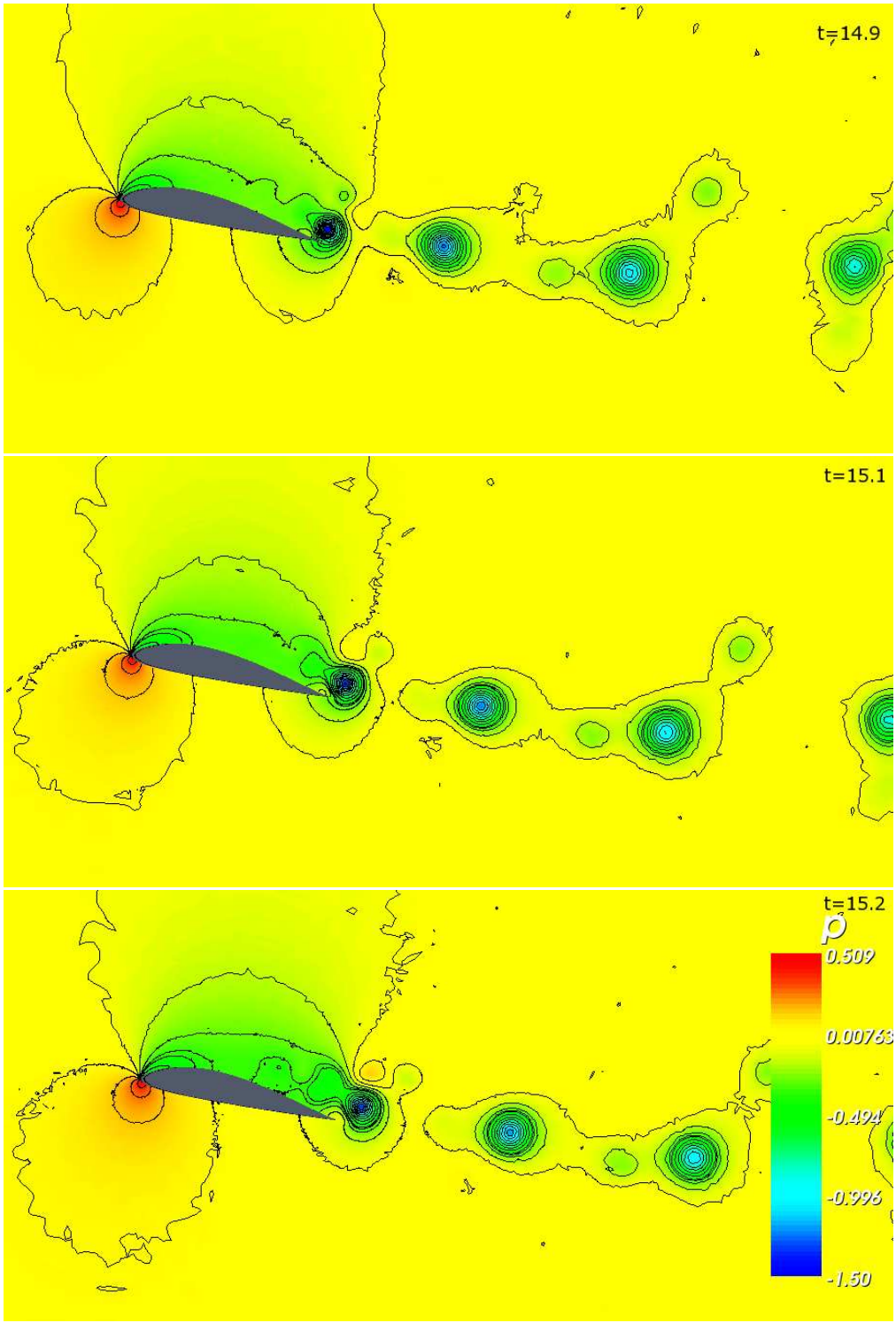

Figure 3.6: Contours of the pressure over a time period for $Re = 5 \cdot 10^3$.

there are no comparable measurements at a $Re = 5000$. The computations have to be continued for some time in order to obtain profound statistical resulting flow fields. Additionally the statistical variation of the turbulent wind field shows a non Gaussian distribution in wind speed and direction[12]. So the next goal will be to resolve the statistical variation of loads on the blade caused by such wind fields. Nevertheless the first results look promising for the future work to use spectral/hp methods as a tool to investigate on dynamical stall effects on rotor blades of wind turbines.

Bibliography

[1] George Em Karniadakis and Spencer J. Sherwin. *Spectral/hp Element Methods for Computational Fluid Dynamics*. Numerical Mathematics and Scientific Computations. Oxford University Press, 1. edition, 1999.

[2] S. Dahlström and L. Davidson. Large eddy simulation of the flow around an aerospitale a-aerofoil. In *Proceedings of the ECCOMAS 2000*, September 2000.

[3] F. Richez, V. Gleize, I. Mary, and C. Basdevant. Zonal rans/les coupling simulation of a transitional and separated ow around an airfoil near stall. In *Conference on Turbulence and Interactions TI2006*, 2006.

[4] L. Davidson, D. Cokljat, F. Fröhlich, A. Leschziner, C. Mellen, and W. Rodi, editors. *LESFOIL Large Eddy Simulation of Flow Around a High Lift Airfoil*, volume 83 of *Notes on Numerical Fluid Mechanics*. Springer Verlag, 2003.

[5] M. Breuer and N. Jovicic. An les investigation of the seperated flow past an airfoil at high angle of attack. In *Direct and Large Eddy Simulation*, volume 8 of *Proc. of the 4th Workshop on DNS and LES, Enschede Netherlands, ERCOFTAC Series*, pages 165–172. Kluwer Academic Publ., 2001.

[6] N. Jovicic, M. Breuer, and J. Jovanovic. Anisotropy-invariant mapping of turbulence in a flow past an unswept airfoil at high angle of attack. *JJournal of Fluids Engineering*, 128(3):559–567, 2006.

[7] Andrei Shishkin and Claus Wagner. Large eddy simu- lation of the flow around wind turbine blade. In P. Wessling, E. Onate, and J. Periaux, editors, *Proceedings of the ECCOMAS 2006*, 2006.

[8] X. Ma, G.-S. Karamanos, and G.E. Karniadakis. Dynamics and low-dimensionality of a turbulent near wake. *Journal of Fluid Mechanics*, 410:29–65, 2000.

[9] Tim Warburton. *Spectral/hp Methods on Polymorphic Multi-Domains: Algorithms and Applications*. PhD thesis, Brown University, 1999.

[10] Xiaoliang Wan, Dongbin Xiu, and George Em Karniadakis. Stochastic solutions for the two-dimensional advection-diffusion equation. *Journal of Scientific Computing*, 26(2):578–590, 2004.

[11] Christophe Geuzaine and Jean-Francois Remacle. Gmsh: A three-dimensional finite element mesh generator with built-in pre- and post-processing facilities. *Journal of Numerical Methods in Engineering*, 2009.

[12] Frank Böttcher. *Statistische Analyse der atmosphaerischen Turbulenz und allgemeiner stochastischer Prozesse*. PhD thesis, Oldenburg University, 2005.

Chapter 4

Analysis of Multipoint Correlations in Direct Numerical Simulation[1]

We examine the Markov properties of the three velocity components of a turbulent flow generated by a DNS simulation of the flow around an airfoil section. The spectral element code Nektar has been used to generate a well resolved flow field around an fx79w-151a airfoil profile at a Reynolds number of Re=5000 and an angle of attack of $\alpha = 12^o$. Due to a homogeneous geometry in the spanwise direction, a Fourier expansion has been used for the third dimension of the simulation.
In the wake of the profile the flow field shows a von Karman street like behavior with the vortices decaying in the wake which trigger a turbulent field. Time series of the 3D flow field were extracted from the flow at different locations to analyze the stochastic features. In particular the existence of Markov properties in the flow have been shown for different cases in the surrounding of the airfoil. This is of basic interest as it indicates that fine structures of turbulence can be replaced by stochastic processes. Turbulent and Markovian scales are being determined in the turbulent field and limits of standard Gaussian Langevin processes are being determined by the reconstruction of a flow field in time and space.

[1]Draft of a manuscript to be submitted as B. Stoevesandt, R. Stresing, A. Shishkin, C. Wagner and J. Peinke: *Multipoint Correlations in Direct Numerical Simulations* to Physics of Fluids

4.1 Introduction

Although computational methods for fluid dynamics have made enormous progress during the recent years, the problem remains to resolve the fine structures of highly turbulent flow. New turbulence models have improved the turbulence simulations to quite some extend [1][2]. Nevertheless, even with the application of new techniques, it remains difficult to correctly simulate turbulent loads e.g. for wind turbines [3][4]. Already the accurate simulation of the flow around single airfoils at higher Reynolds numbers is a difficult task [5][6], as it is difficult to grasp the correct turbulence properties everywhere in the flow. Therefore a lot of effort has been made to improve the modeling of the turbulence in small scales with subgrid models. The most common models are so called "deterministic" models based on eddy viscosities. Meneveau et. al. give a good overview on such models for large eddy simulations (LES) [7].
Since a deterministic description of turbulence still has its limits, it is very convenient to describe the turbulence by a time series [8]. The reconstruction of stochastic time series has made quite some progress in the recent years. First approaches involved the Fokker-Planck equation with Gaussian diffusion [9]. However today the research expands to Langevin equations for Levy processes [10] or even non-Markovian fields [11]. From this evolved approaches to model turbulent data in different fields of science. Hence such methods arouse some interest for the modeling of turbulent flows in numerical flow simulations [12].
Some approaches to use stochastic models for flow simulations have been undertaken. Laval and Dubrulle proposed a Langevin approach for LES models which showed promising first results. Based on the Rapid Distortion Theory (RDT)-model, described in [13][14] and [15], they developed a Langevin equation for an LES model, with friction made of viscosity and rapid distortion by resolved scales, using stochastic forcing with a mean value generated from the energy cascade. The model was validated on the flow in an empty cube against a DNS simulation.
Mostly however, stochastic models were developed and used in the context of particel tracking or a Lagrangian framework as described by Bakosi, Pope, Shotorban or Fox [16][17][18][19][20]. The particle tracking method by Bakosi works with a finite element grid in a Eulerian framework in contrast to the work of other groups. The physical magnitudes of the particles are described by probability density functions (pdfs) at each specific point.
This approach requires the knowledge of the pdfs within a flow. One way to obtain these pdfs is the reconstruction by the Fokker-Planck equation using time series data. In an isotropic and homogeneous field of Gaussian turbulence this method is very easily applied and valid. In non-homogeneous flow fields the stochastic properties of the flow will differ in space. A stochastic reconstruction of the fields using the method proposed by Friedrich and Peinke in [9][21] might nevertheless still be a promising approach to gain knowledge about the turbulent

characteristics of a flow field for the modeling of pdfs. This shall be the focus of the following contribution.

4.2 The underlying equations for turbulence models

The starting point for stochastic modeling is to consider a quantity in a statistical context. In case of fluid dynamics this is done using the Reynolds decomposition

$$u = \overline{u} + u' \tag{4.1}$$

where $\overline{u}$ is the averaged velocity field and u' denotes it's fluctuation. For time averaging the decomposition applied to the Navier-Stokes equations leads to the so called Reynolds Averaged Navier Stokes Equations (RANS). For incompressible fluids they read:

$$\partial_t \overline{u}_i + \partial_j \overline{u}_j \overline{u}_i + \partial_j \overline{u'_j u'_i} = -\frac{1}{\rho}\partial_i \overline{p} + \nu \partial_j^2 \overline{u}_i. \tag{4.2}$$

The incompressible continuity equation is the given as

$$\nabla \cdot (\overline{u} + u') = \nabla \cdot \overline{u} = \nabla \cdot u' = 0. \tag{4.3}$$

To solve the closure problem, models for the Reynolds stress term

$$\partial_j \overline{u'_j u'_i} \tag{4.4}$$

are needed.
This is getting more complicated for LES models. Here the velocity field is spatially filtered and split into a resolved field $\overline{u}_i$ and a subgrid field given by $u'_i = \overline{u}_i - u_i$ for $u_i(x_i, t)$ (note that here the average $\overline{u}_i$ describes an average over a spatial region and not - like in RANS - in time or over ensembles). In this situation the momentum equation of the Navier-Stokes equations turn out to be

$$\partial_t \overline{u_i} + \overline{(\overline{u}_i \partial_i)\overline{u}_j} + \overline{(\overline{u}_i \partial_i)u'_j} + \overline{(u'_i \partial_i)\overline{u}_j} + \partial_j \overline{u'_j u'_i} = -\frac{1}{\rho}\partial_i \overline{p} + \nu \partial_j^2 \overline{u}_i. \tag{4.5}$$

In this case a model for the forcing term $l = (\overline{u}_i \partial_i)u'_j + (u'_i \partial_i)\overline{u}_j$ is needed in addition to the subgrid scale tensor. Recently, Laval et al. [13] propose a stochastic approach to the first unknown term by putting up a Langevin equation:

$$\partial_t l = Al + \xi, \tag{4.6}$$

where a Gaussian noise ξ needs to be added in the equation, while A is a generalized evolution operator. Based on the observation that subfilter-scales are mostly

dependent to resolved scales by a linear process similar to rapid distortion, Laval et al. derive from the momentum equation a model for the evolution operator A [13].
Another approach is the one by Bakosi et.al. [16] who model the stress terms using a (Gaussian) Wiener process to gain a pdf for the stresses. However the knowledge of the pdfs and the ability of their reconstruction are a premise for such a method. This requires the correct description of the turbulent field at all scales. Here the n-point correlation approach by using increments and the knowledge about Markov properties in a flow field is a basis [22][23] from which further modeling can proceed. Tutkun et. al. have done an analysis of a spatial flow field experimentally [24].
As a typical example of a problem of turbulent flow we analyze here a flow field obtained by a DNS simulation of the flow around an airfoil to describe the method. The simulation, its parameters and the resulting field are presented at first in the following section. Then the basic aspects of our stochastic approach is explained in 4.4. The results of the analysis of the data are finally discussed in section 4.5.

4.3 The Simulation

4.3.1 Simulation Parameters

To gain a time series of a turbulent flow field a DNS simulation has been done using the high order spectral element code $\mathcal{N}\varepsilon\kappa\mathcal{T}\alpha r$ [25]. It combines finite element methods with the accuracy of spectral methods using Jacobi polynomials for the spectral expansion [26]. For the velocity pressure coupling a stiffly stable pressure correction scheme and an Adams-Bashfort predictor corrector time step were used as described in [27].
To obtain a well-studied and representative turbulent flow field from numerical flow simulations, the flow over an airfoil has been investigated [28]. The configuration is a 3D flow over a section of an fx79w-151a airfoil at an angle of attack of $\alpha = 12°$ at a Reynolds number of $Re = 5000$ in respect to the chord length.
The used $\mathcal{N}\varepsilon\kappa\mathcal{T}\alpha r$ code works with a 2D mesh with rather few elements for a first spatial discretisation. Further, the interior of the elements is calculated using an expansion by Jacobi polynomials [29]. Here we used a polynomial order of n=9. The discretisation in the homogeneous spanwise direction of the airfoil was realized using the "Fourier" version of the code which calculates the third - spanwise - dimension using a Fourier expansion in combination with periodic boundary conditions on the sides of the domain (for validations see e.g. [30][31]). Measured in chord lengths L_c, the domain size expands from $-10L_c$ to $10L_c$ in the cross-flow direction and from $-6L_c$ to $20L_c$ streamwise direction. The domain size in spanwise direction was set to $\pi \cdot L_c$, which showed good results in

a simulation on the flow around a cylinder at Re=3900 [30]. The extension in the spanwise direction seems to be sufficient, as integral scales in the turbulent region in all directions are one order smaller than the domain size (see L in table 4.1). 64 Fourier planes have been used for the expansion in spanwise direction together with a 2D hybrid mesh consisting of 2116 elements (see fig. 4.1).
To resolve the boundary layer flow a quadrilateral grid layer was created around

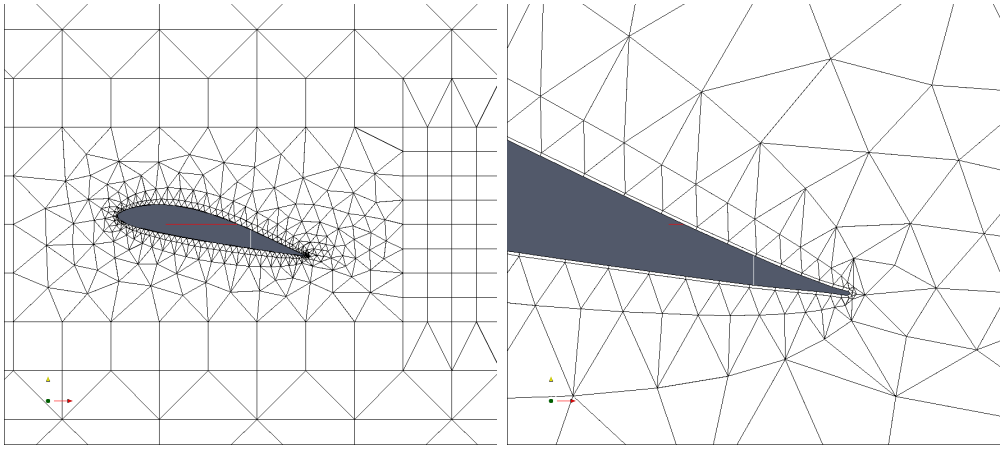

Figure 4.1: 2D grid of the airfoil setup, consisting of 1179 quadrilaterals and 937 triangles. A close-up on the right shows the boundary resolution and the resolution of the tail.

the airfoil. The original shape of the airfoil was not changed since every detail of the geometry has been taken into account. As the tail of the airfoil had a tiny triangular shape, the resolution of this tail leads to very small elements at the trailing edge (see fig. 4.1 on the right). This resulted in very small time steps of order $t \approx 10^{-5}$. In our simulation the maximum CFL was ≤ 0.4.
To avoid instabilities which in turbulent flows often develop from Neumann outflow boundary conditions a sponge layer has been implemented increasing the viscosity in the last $3L_c$ before the outflow. Finally we used a uniform laminar velocity distribution at the inflow.

4.3.2 Simulation Results

Fig. 4.2 depicts the average flow field over the airfoil. Here and further on, all units are dimensionless and normed to chord length of the airfoil (see eq. (1.5)-(1.8)). The average flow field is mainly characterized by a laminar flow separation in the tip region with an impingement point in the area behind $\frac{4}{5}L_c$. The shear flow which develops downstream the separation point leads to a von Karman like vortex street in the rear part of the airfoil. Triggered by the vortices a turbulent wake flow field appeared (see e.g. vorticity contours in fig. 4.3a)). To give an impression of the distribution of the turbulence intensity in

the field, fig. 4.3b) shows contours of the RMS of the velocity magnitude of the flow in the vicinity of the the airfoil. In this figure high fluctuations in the velocity magnitude are recognizable mainly close to the trailing edge and in the wake. Thus for the study of turbulence at and around the airfoil the regions at the trailing edge and in the wake of the airfoil were of main interest.
To perform a time series analysis of the flow properties specific points effected by the turbulent wake flow have been chosen within selected elements of the mesh in the region depicted in fig. 4.4.

The regions selected were positioned on one hand in the wake (element 1),

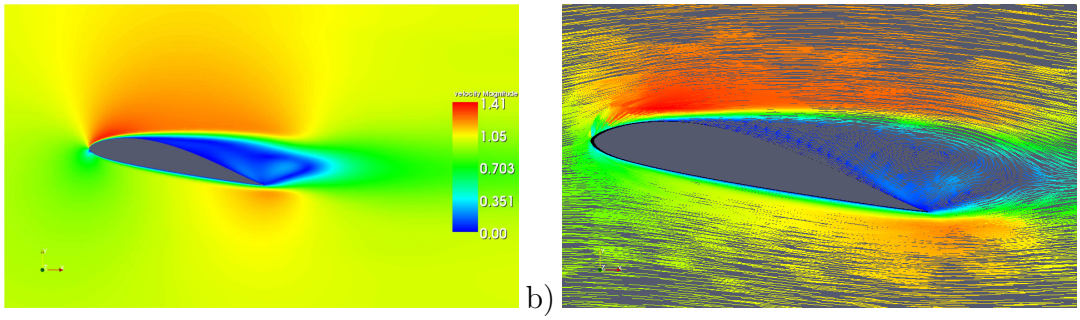

a) b)

Figure 4.2: Average velocity of the flow field over t=20 in normalized time scales. The magnitudes of the velocity given in a) by the colors, additionally the vector orientation of the flow in b).

on the other hand close to the trailing edge of the airfoil at different heights (elements 2-5). It must be noted that all position selected for the recording of time series are located in regions with a triangular unstructured grid. Within the selected elements at the spanwise position of $z = 2.11L_c$ a time series of 10922 datasets at 208 different spatial points were collected at a sampling rate of $f_r = 400$. Out of the five selected elements 62 points have been chosen for the purpose of the following analysis.

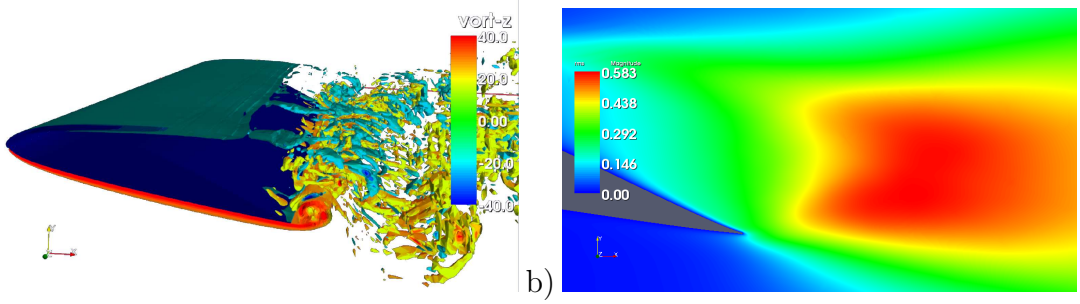

a) b)

Figure 4.3: Snapshot of vorticity components in z-direction a) and rms-fluctuations of the velocity magnitude in b).

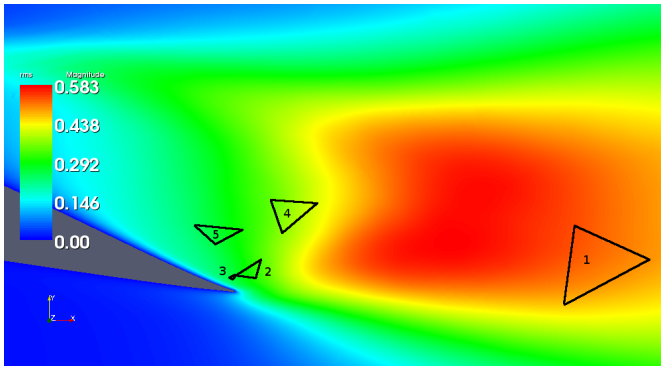

Figure 4.4: Selected grid in the region just above the trailing edge for the further investigation of the turbulence

4.4 The Definition of Markov Properties

In the following the stochastic analysis of the turbulent flow field will be discussed. The final aim is to gain more knowledge of the Reynolds stress tensor, which for a the stochastic analysis reads

$$\overline{u_i' u_j'} = \int u_i' u_j' p(u_i' u_j') d(u_i' u_j'), \tag{4.7}$$

where $p(u_i' u_j')$ is the probability density function (pdf) of the components of the Reynolds stress tensor $u_i' u_j'$.
In the following we will generalize the discussion on the stochastic features of important fluctuating quantities such as Reynolds stress. For turbulence it is of central interest to characterize the spatial correlations of quantities $\phi(x_i, t)$. Therefore it is common to investigate the statistics of increments in a scale of r at the same point in time t

$$\phi(r, t) = \phi(x_i - r, t) - \phi(x_i, t), \tag{4.8}$$

where x_i denotes the position in space and t is the time.
The following analysis will be based on probabilities of such increments at different scales. The conditioned probability function of ϕ can be described as

$$p(\phi_1, r_1 | \phi_2, r_2; ...; \phi_n, r_n) = \frac{p(\phi_1, r_1; \phi_2, r_2; ...; \phi_n, r_n)}{p(\phi_2, r_2; ...; \phi_n, r_n)} \tag{4.9}$$

where the left hand side reflects the probability density function of the magnitude ϕ_1 at the incremental scale r_1 under the condition that at the scales $r_2, ..., r_n$ the

magnitudes $\phi_2, ...\phi_n$ have selected fixed values. Here we use $r_i < r_{i+1}$ and the abbreviation $\phi_1 = \phi(r_1, t)$.
In stochastics we speak of Markov properties, if the pdf of a dataset can be completely described with the knowledge of the neighboring magnitude at scale r_{n-1} without being influenced by the next magnitude at r_{n-2}. In case of the increments this means:

$$p(\phi_n, r_n|\phi_{n-1}, r_{n-1}; ...; \phi_1, r_1) = p(\phi_n, r_n|\phi_{n-1}, r_{n-1}) \tag{4.10}$$

If this is the case the general n-scale statistics can be closed by the two scale statistics $p(\phi_n, r_n|\phi_{n-1}, r_{n-1})$. Furthermore, it is possible to apply the Kramers-Moyal expansion of the data series, which leads to:

$$-r\frac{\partial p(\phi, r|\phi_0, r_0)}{\partial r} = \sum_{k=1}^{\infty}\left(-\frac{\partial}{\partial\phi}\right)^k D^{(k)}(\phi, r)p(\phi, r|\phi_0, r_0). \tag{4.11}$$

The coefficients of this expansion are defined as

$$D^{(k)}(\phi, r) = \lim_{\Delta r\to 0} M^{(k)}(\phi, r, \Delta r) \tag{4.12}$$

$$M^{(k)} = \frac{r}{k!\Delta r}\int_{-\infty}^{\infty}(\phi' - \phi)^k p(\phi', r - \Delta r|\phi, r)d\phi'. \tag{4.13}$$

This definition of $D^(n)$ can be used to estimate its value directly from the data [9][21][22].
The theorem of Pawula states that $D^{(k)} = 0\ \forall\ k > 2$ if the coefficient of the expansion $D^{(4)} = 0$ [32]. In such a case the Kramers Moyal expansion (4.11) truncates to the second order, yielding the Fokker-Planck equation (also called Kolmogorov forward equation) [32]:

$$\partial_r p(\phi, r|\phi_0, r_0) = [-\partial_\phi D^{(1)}p(\phi, r) + \partial_\phi^2 D^{(2)}p(\phi, r)]p(\phi, r|\phi_0, r_0). \tag{4.14}$$

The first coefficient $D^{(1)}$ is referred to as the drift coefficient, the second coefficient $D^{(2)}$ is called diffusion coefficient and determines the strength of a Gaussian distributed white noise. This noise is δ-correlated due to the Markov properties [32]. The Fokker-Planck equation can be reformulated as a Langevin equation following Itô or Stratonovich (see [32]). The Itô formulation is:

$$-\frac{\partial\phi(r)}{\partial r} = \frac{1}{r}D^{(1)}(\phi, r) + \sqrt{\frac{1}{r}D^{(2)}(\phi, r)}\Gamma(r). \tag{4.15}$$

$\Gamma(r)$ is the Gaussian distributed white noise.
Under these conditions it is possible to analyzed the Reynolds stress tensor $\phi = u_i'u_j'$. Having determined $D^{(1)}$ and $D^{(2)}$, the Fokker-Planck eq. (4.14) allows to

reconstruct a series on all n-scales of r_n [33]. Thus it is possible to reconstruct $p(\phi_i, r_i)$ for given scales r_i, where r_i may be given by a finite spatial relation. This can be used as an expression for the components of the Reynolds stress tensor $u_i' u_j'(r)$ eq. (4.4). A similar procedure could be constructed for other relevant turbulent quantities like the additional stress terms in equation (4.5).
The aim is now to find out under which conditions this stochastic simplification holds for a given flow problem. However, the geometrical distribution of the data points of the flow field makes a straight forward analysis difficult since not enough straight r_n scales could be evaluated for a complete reconstruction. Therefore the analysis is being done using the Taylor hypothesis of frozen turbulence, which is applied quite frequently also in experimental works (like e.g. [22][23]), by

$$r = \tau \overline{u}. \tag{4.16}$$

Now, $\tau = (t - t_0)$ is a time scale by which the same analysis can be undertaken as in given above in equations (4.9)-(4.13).
In this paper we focus on the most important underlying Markov property. Thus we look if

$$p(u_0, \tau_0 | u_1, \tau_1; u_2, \tau_2)) = p(u_0, \tau_0 | u_1, \tau_1) \tag{4.17}$$

in time and in spatial scales if

$$p(u_0, r_0 | u_1, r_1; u_2, r_2) = p(u_0, r_0 | u_1, r_1) \tag{4.18}$$

holds, u is one velocity component and $r = x_0 - x_1$ is a spatial scale for this coordinate. For simplicity reasons the nomenklatura used for the coordinates and orientations has been chosen as in usual Cartesian coordinates giving (x, y, z) for the streamwise, crossflow and spanwise direction as well as $(u(\tau), v(\tau), w(\tau))$ for the velocity increments in this direction.

4.5 Analysis of the results

From the over all flow field four points (marked as 13,61,119 and 218) have been selected for further evaluation (see fig. 4.5). In table 4.1 the scale of the spacing between the points r is given for all components (x,y,z) as well as the mean velocity components $\overline{u_i}$, standard deviation σ_i of the velocities and estimations of the integral, Taylor and dissipation length scales, represented by L_i, λ_i and η_i respectively. All length scales have been calculated according to [34]. Since the Taylor length is a fit with possible deviations and the dissipation scale is derived from the Taylor length, both more or less give values for the order of magnitude and are not to be seen as exact values.

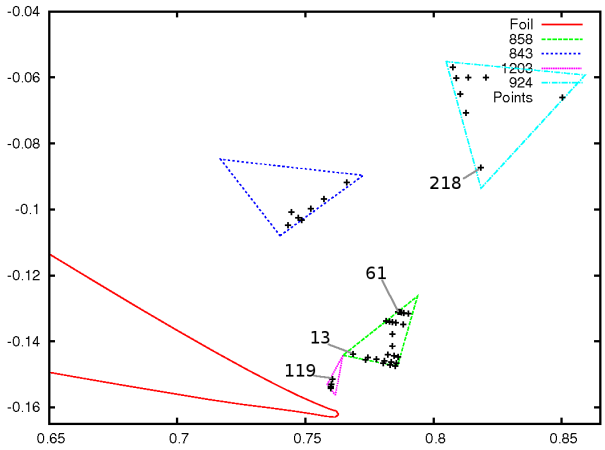

Figure 4.5: Geometric positioning of the evaluated points in the region over the tail of the airfoil. The numbered points have been selected for further analysis and reconstruction

4.5.1 Analysis in time scales

The first analysis of the time series has been conducted using the dataset of the point marked with the number 218 as a reference in time scales τ. We are later interested to use the Taylor hypothesis. The mean flow field direction is oriented in the x-y-plane. Therefore we focussed here on the analysis of the u- and v-velocity increments. However, the complete analysis has also been done for the spanwise direction, even though for brevity these results might not all be presented here.
To give a first idea of the distributions of the velocity increments, the non conditioned histograms of the single components are shown in fig. 4.6 for $\tau_0 = 0.15$.

It is obvious, that for the u and v-components there is some skewness in the distribution and all distributions are non-Gaussian.
Next we discuss at which scales the flow field does show Markov properties. For all geometrical points a dataset of a time series of 10922 points in time was recorded. Since this was very short, only 15 bins have been used for the evaluation.
Fig. 4.7 shows the contours of the conditioned probability density function for $p(u_i, \tau_0|u_{i,1}, \tau_1)$ and $p(u_i, \tau_0|u_{i,1}, \tau_1; u_{i,2}, \tau_2)$ for $\Delta\tau = \tau_1 - \tau_0 = 0.15$, $\tau_0 = 0.15$ and $\tau_2 = \tau_0 + 2\Delta\tau$ for the velocity components u and v. Also slices of the contour-plot are given to give an impression of the shape of the conditioned pdfs.

The shapes of the pdfs do not appear very smooth as it has to be kept in mind, that the over all number of data is just above 10000 and the plots are logarithmic. However, the similarity of the two contours suggest the existence of Markov

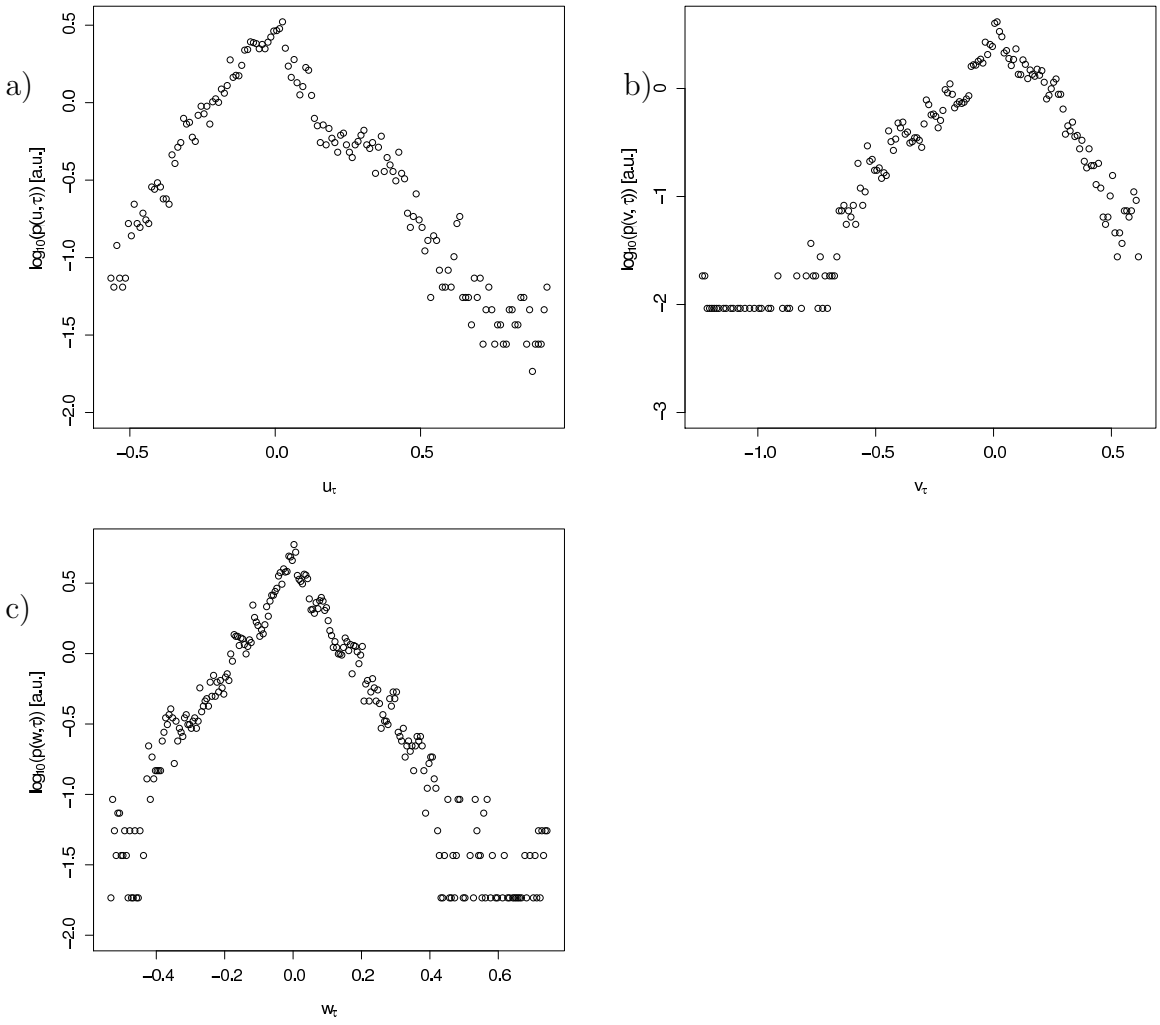

Figure 4.6: Histogram of the velocity increments in semi-logarithmic presentation for u in a), v in b) and w in c) and $\tau_0 = 0.15$.

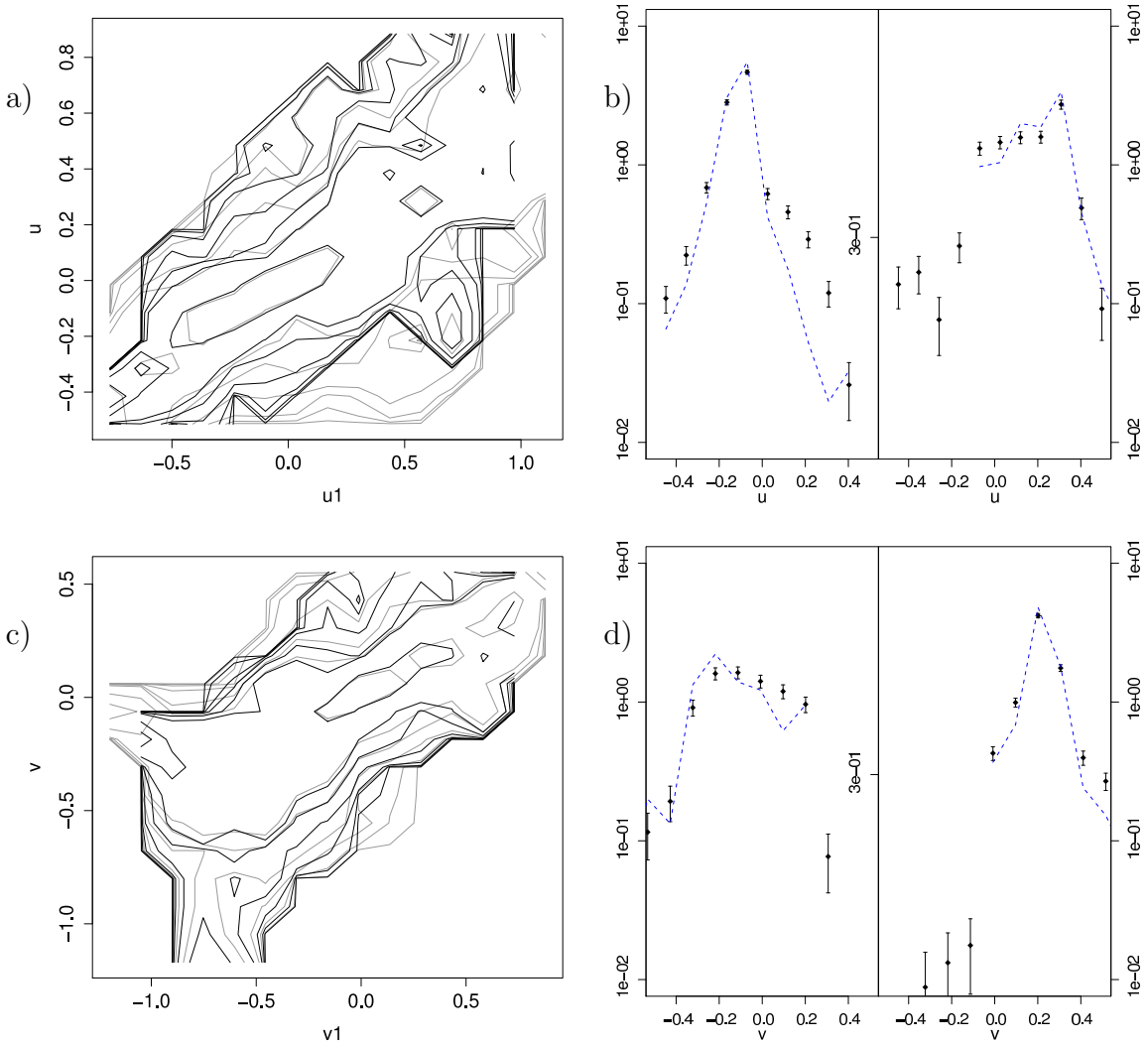

Figure 4.7: a) and c) give the contour plots of the pdfs of $p(u_i, \tau_0|u_{i,1}, \tau_1)$ (gray) and $p(u_i, \tau_0|u_{i,1}, \tau_1; u_{i,2}, \tau_2)$ (black) for $\tau = 0.15$ for u- and v-increments respectively. Slices at about $+/-0.8\sigma$ for u- and $+/-0.9\sigma$ for v-increments in b) and d) respectively show a high coherence between the two distributions, where the dotted line represents the data from $p(u_i, \tau_0|u_{i,1}, \tau_1; u_{i,2}, \tau_2)$ and the errorbars are given by $\sqrt{N}$ with the number of events N in the bin.

Point	Component	r	$\overline{u}$	σ	L	λ	η
218	x	0.0	-0.14	0.253	0.1805	0.0139	0.0005
218	y	0.0	-0.12	0.216	0.1519	0.0087	0.0004
218	z	0.0	-0.006	0.157	0.3308	0.0048	0.0003
61	x	0.032	-0.039	0.2077	0.1523	0.0032	0.0002
61	y	0.044	-0.074	0.171	0.1539	0.0065	0.0004
61	z	0.0	-0.004	0.129	0.1666	0.0033	0.0003
13	x	0.050	-0.012	0.183	0.1598	0.0014	0.0002
13	y	0.057	-0.058	0.112	0.1771	0.0064	0.0005
13	z	0.0	0.004	0.130	0.2850	0.0041	0.0004
119	x	0.058	0.028	0.151	0.1689	0.0033	0.0003
119	y	0.066	-0.036	0.059	0.1824	0.0033	0.0005
119	z	0.0	-0.001	0.135	0.5075	0.0024	0.0003

Table 4.1: The analyzed points, their geometrical distances - with point 218 as a reference point -, their velocity and the statistical properties of the velocity for all components.

properties.
Next, a more quantifying test is done to check if Markov properties are given. To evaluate the Markov properties, now a χ^2-test has been performed for the distributions of $p(u_i, \tau_0|u_{i,1}, \tau_1)$ and $p_2(u_i, \tau|u_{i,0}, \tau_0; u_{i,1}, \tau_1)$ (see [35])

$$\chi^2 = \sum_i \frac{(p_1(i) - p_2(i))^2}{p_1(i)}. \tag{4.19}$$

Here $p_1(i)$ represents the first probability density - in this first case $p(u_i, \tau_0|u_{i,1}, \tau_1)$, i is the bin number and $p_2(i)$ is the second probability density respectively - here $p(u_i, \tau_0|u_{i,1}, \tau_1; u_{i,2}, \tau_2)$. The test quantifies the difference between two pdfs from data with errors. Usually as p_1 a theoretically know pdf is taken. For our purpose of the estimation of the existence of Markov properties, this might lead to cases where $p_1(i) = 0$. In such cases we set χ^2 has been set to 0. Thus $\chi^2 = 0$ events had to be evaluated separately.
15 bins have been used for evaluation, giving 15 degrees of freedom. Taking the average of the χ^2 values for all the evaluated distributions shown in fig. 4.8 for all velocity components, we obtain an impression of the validity of the assumption of Markov properties.
In fig. 4.8 it becomes evident, that the bins containing few incidences further from the mean values, show stronger deviances in the distributions. This might be due to statistical reasons which lead to very low binning values, however it might also be caused by a non-Markovian behavior of the stronger fluctuations in the flow at some scales. This could only be clarified if the dataset would be

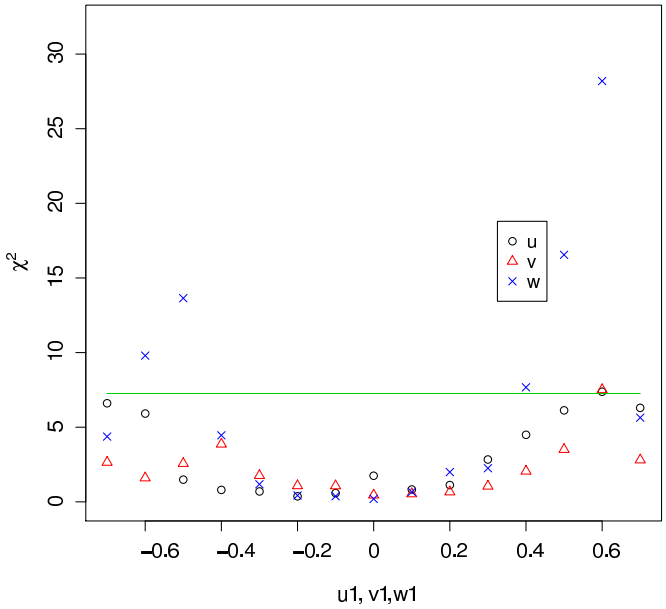

Figure 4.8: χ^2 values for the conditioned pdfs with τ_0 and $\Delta\tau = 0.15$ against the u_1, v_1, and w_1-velocity increments bin. χ^2 is calculated as the sum over all velocity bins u, v and w. The line marks the value under which the probability of the distribution to be non-Markovian is less then 5% in the classical χ^2 theory.

increased for a longer simulation period.
Due to this insecurity in the Markov analysis, five bins have been excluded from the evaluation for the further analysis: The three outer bins to the lowest negative velocity increments and the two bins containing the highest velocity increments. Fig. 4.9 shows the dependency of the average χ^2 on $\Delta\tau$ for $0.0125 \leq \Delta\tau \leq 0.45$ for the velocity components, a) and c) including all bins and in b) and d) using only 10 bins after the exclusion of the five bins containing to few data. Note, that with the decrease of degrees of freedom, the limit for the criterion of the probability being $\leq 5\%$ for non-Markov properties also decreases.

Using the 10 bins we can expect Markov properties at $\Delta\tau \geq 0.15$ for the v- and w-component while for the u-component we supposed to have a Markovian field for $0.075 \leq \Delta\tau \leq 0.375$. Applying the Taylor hypothesis (eq. (4.16)), this would correspond to a so called Markov length of $\lambda_M = 0.011$ for the u-velocity and $\lambda_M = 0.018$ for the v-velocity respectively. Note the comparable values to λ in table 4.1 as proposed by [36].
Within the estimated validity range for the Markow properties, now the Kramers-Moyal coefficients have been determined for each τ and $\Delta\tau$. Therefore for each τ a fit for $lim_{\Delta\tau\to 0}$ corresponding to equation (4.13) has been done. To estimate $D^{(1)}$ a linear fit was used, whereas for $D^{(2)}$ and $D^{(4)}$ logarithmic fits have been used, since they fitted to course of the curve better and avoided

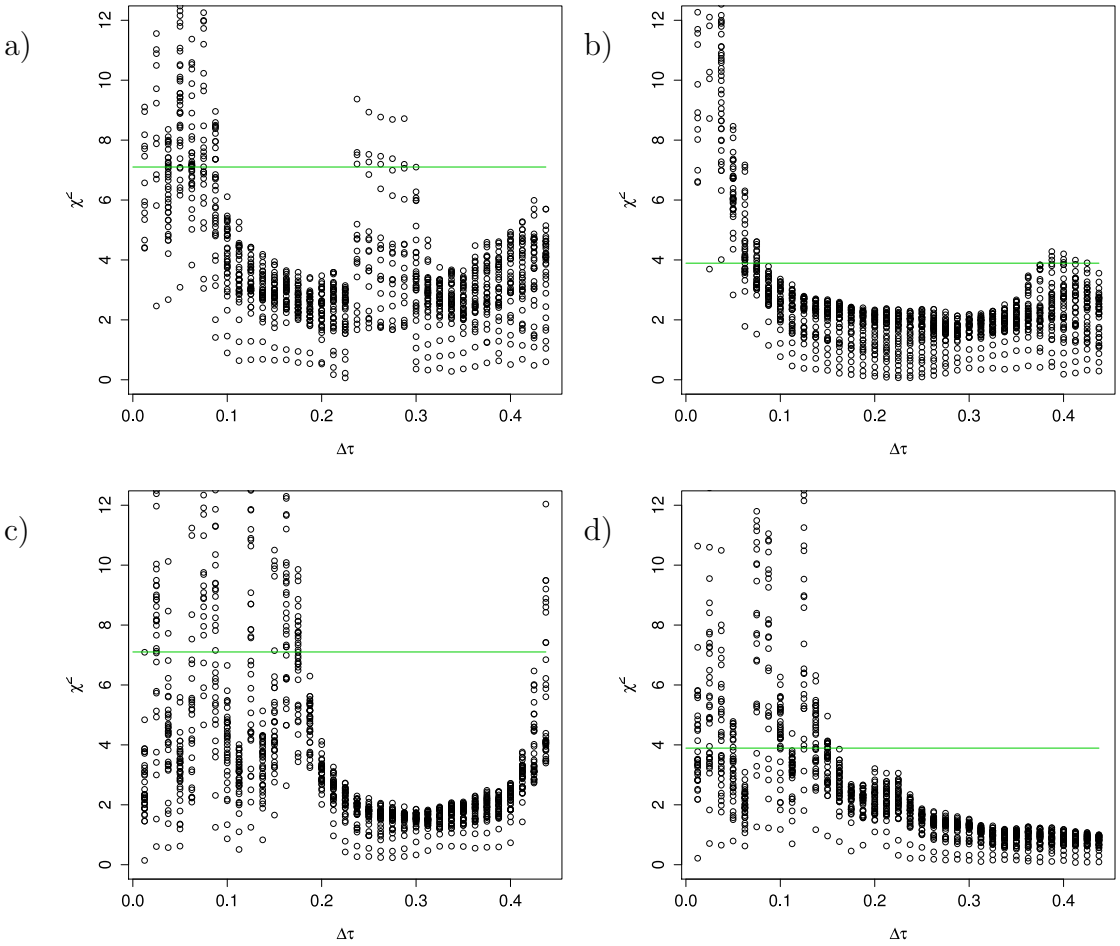

Figure 4.9: χ^2 in dependency of $\Delta\tau$ for all bins a) and c) on the left and for only 10 well populated bins on the right b) and d), as a) and b) depict the u-component and c) and d) the v-component. It becomes evident, that Markov properties can be assumed in case of the smaller absolute value of the increments where enough data is available. The assumed validity of the Markov properties in the date here is $\Delta\tau \geq 0.15$ for the v-component and $0.075 \leq \Delta\tau \leq 0.375$ for the u-component.

unphysical negative values. As an example in fig. 4.10 a), b) and c) the fit for the normed v-velocity increments at $\tau = 0.15$ is shown for $D^{(1)}$, $D^{(2)}$ and $D^{(4)}$.

The $D^{(1)}(u_i, \tau)$ and $D^{(2)}(u_i, \tau)$ have further been fitted by a linear and a quadratic function over all $u_{i,\tau}$, as described by Renner in [22] for isotropic turbulence (see fig. 4.10 d) and e)). These fits were in the following used for the reconstruction.
Even though we cannot assume $D^{(4)}(u_i, \tau) = 0$ in the dataset used, since $D^{(4)} << D^{(2)}$ we take the Fokker-Planck equation (4.14) as an approximation.

4.5.2 Reconstruction in time

To get an estimation of the accuracy of a reconstruction assuming a Gaussian field, the reconstruction has been done using only the first two Kramers-Moyal coefficients.
The obtained $D^{(1)}(u_i, \tau)$ and $D^{(2)}(u_i, \tau)$ are used to reconstruct the time series with a Langevin equation (4.15) modified for time scales. In fig. 4.11 the pdfs $p(u_i, \tau_0|u_{i,1}, \tau_1)$ and $p(u_i, \tau_0|u_{i,1}, \tau_1; u_{i,rec}, \tau_2)$ of the u- and v-velocity increments for $\tau_0 = 0.15$ and $\tau_1 = 0.30$ are compared. Here $u_{i,rec}(\tau_2)$ is the reconstructed data at a 3τ scale. Below again slices at about $+/-0.8\sigma$ for u and $+/-0.9\sigma$ are shown.

The pdfs of the increments show a non perfect, but quite good reconstruction. Fig. 4.12 shows the semi-logarithmic plot of the pdf of the original data against the reconstructed data for $\tau_0 = 0.15$. Although certainly the dataset was still short, the general shape of the curve is met in most cases (see table 4.5.2). The main reason for deviations is most likely the approximation for the Kramers-Moyal expansion, since $D^{(4)} \neq 0$ as the higher order Moments are not met perfectly.

The contours of the single conditioned pdfs $p(u, \tau_0|u_1, \tau_0 1)$ and $p(u, \tau|u_{rec}, \tau_1)$ give a good impression of the quality of the reconstruction (fig.4.13) in the relation between the developments of the pdfs in time. While the overall tendency of the structure of the main peaks and their form is very similar, the spatial extension differs a bit between the two pdfs.

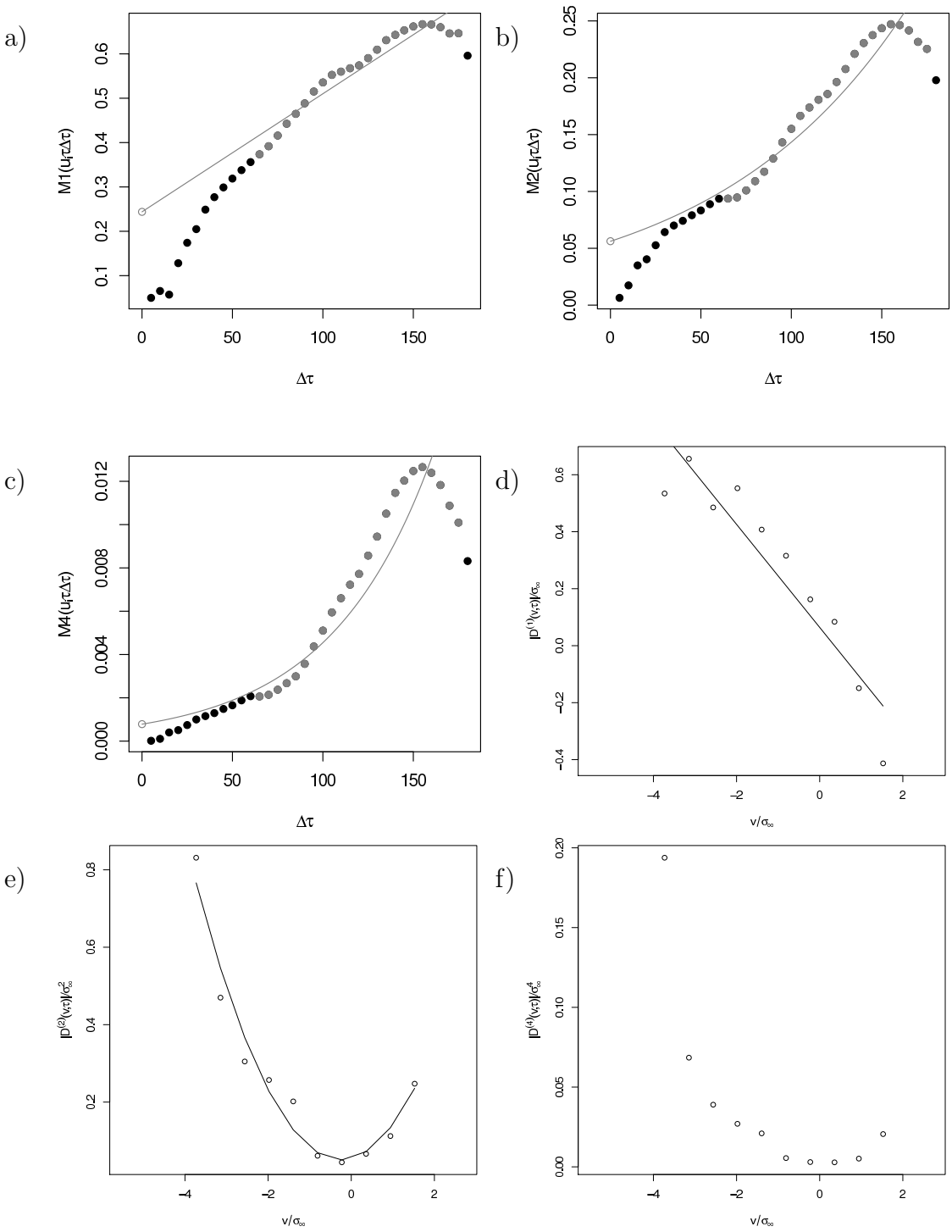

Figure 4.10: Examples of the fits of $M^{(1)}$, $M^{(2)}$ and $M^{(4)}$ in fig. a), b) and c) respectively for $\tau = 0.15$. The used range is plotted in gray, while black dots have been excluded. The resulting normed $D^{(1)}$, $D^{(2)}$ and $D^{(4)}$ plotted on all used bins with fits for $D^{(1)}$ and $D^{(2)}$ in d), e) and f).

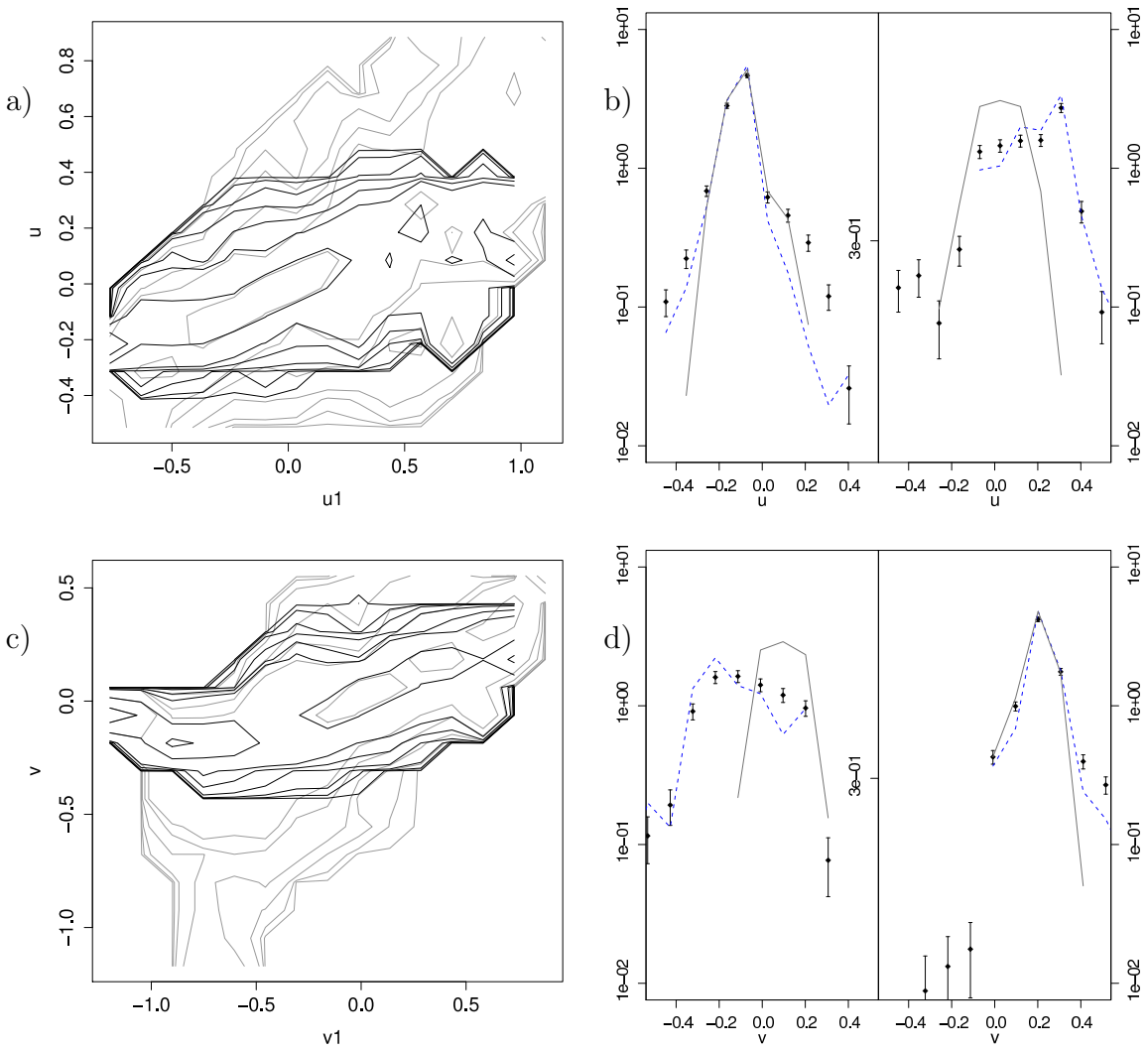

Figure 4.11: Comparison of the contour plots in a) and c) of the pdfs of $p(u_i, \tau_0|u_{i,1}, \tau_1)$ and $p(u_i, \tau_0|u_{i,1}, \tau_1; u_{i,rec}, \tau_2)$ for $\tau = 0.15$ in case of the reconstructed time series $u_{i,rec}$ for u- and v-increments respectively. Again slices at about $+/-0.8\sigma$ for u and $+/-0.9\sigma$ for v in b) and d) respectively give an impression of the distributions. Here the dotted line represents the data from $p(u_i, \tau_0|u_{i,1}, \tau_1; u_{i,2}, \tau_2)$ and the solid line the data from $p(u_i, \tau_0|u_{i,1}, \tau_1; u_{i,rec}, \tau_2)$.

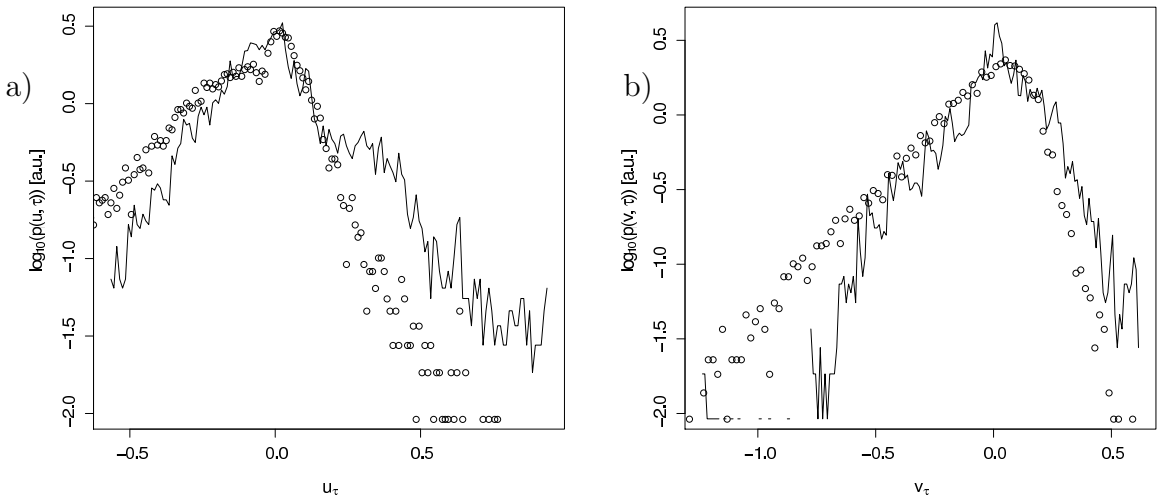

Figure 4.12: Logarithmic plot of the non conditioned pdfs $p(u, \tau_0)$ (line) and $p(u_{rec}, \tau_0)$ dots at $\tau_0 = \tau_1 = 0.15$ showing good general coincidence some differences in particular due to the different skewness of the distributions.

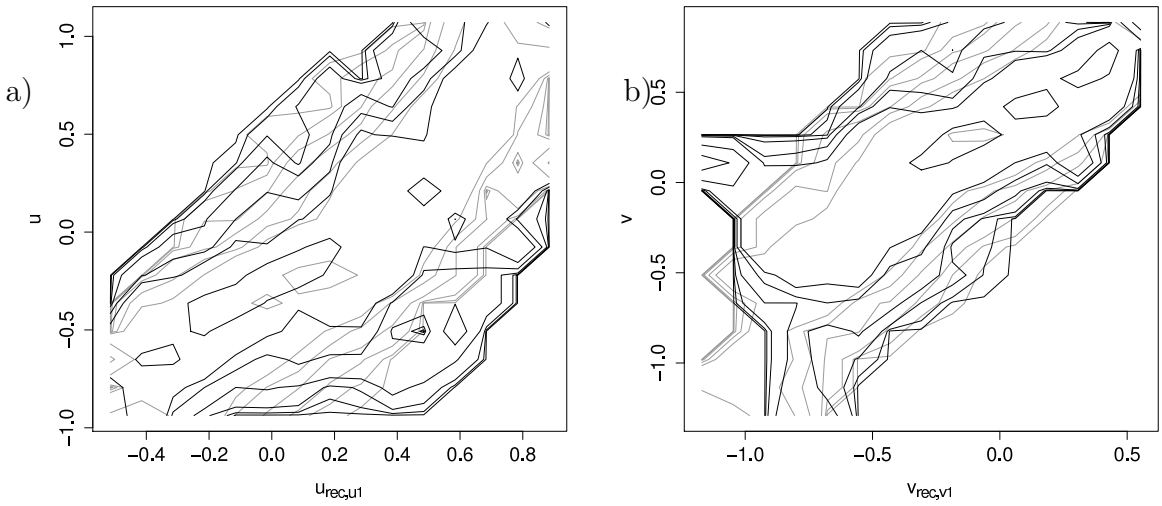

Figure 4.13: Contour plot of the single conditioned pdfs $p(u, \tau|u_0, \tau_0)$ (black) and $p(u, \tau|u_{rec}, \tau_0)$ (grey) at $\tau = \tau_0 = 0.15$ showing the coincidences and some differences between the contours, especially due to the asymmetry of $p(u, \tau|u_0, \tau_0)$.

Comp	Type	Mean	σ	Skewness	Ex-Kurtosis
x	data	0.001	0.224	0.75	1.46
x	recon	-0.1246	0.243	-1.08	2.63
y	data	0.003	0.216	-0.74	2.06
y	recon	-0.089	0.258	-1.37	3.07
z	data	0.0008	0.155	0.26	2.03
z	recon	-0.051	0.158	-1.00	4.23

Table 4.2: Statistical properties of the distributions of the original data (marked with data) and the reconstructed time series (recon) for $\tau = 0.15$. Notable is that the higher order moments are not reconstructed correctly.

4.5.3 Reconstructing the spatial distributions

One of the main problems for flow simulations is the unknown statistics of the flow at a distant point. After having obtained convincing results for the Markov properties of velocity increments, we will apply next the Taylor hypothesis to investigate the velocity increments in for the selected points 218,61,13, and 119 of fig. 4.5.
For local isotropic turbulence it is well know that for increment statistics in space and in time are related by the Taylor hypothesis. Here we will consider a flow with a shear which is not homogeneous or local isotropic. The open question is, whether it is possible to use the above obtained characteristics of the turbulent flow for an application in space.
First we start with the Markov properties. Fig. 4.14 shows the contours of the conditioned pdfs $p(u_i, r_0|u_{i,1}, r_1)$ and $p(u_i, r_0|u_{i,1}, r_1; u_{i,2}, r_2)$ of the u- and v-velocity increments between the points 218-61, 218-13 and 218-119, with overall distances $r = 0.054$, $r_0 = 0.076$ and $r_1 = 0.088$.

The contours in fig. 4.14 indicate good Markov properties. This is reflected in the χ^2 values for the two distributions shown in fig. 4.15 where some of the outer bins have a the lack of data points. However, especially close to the mean velocity increments $\overline{u}_{i,r_0}$ the Markov properties can be very well assumed, as the probability of a non Markovian field is $\leq 5\%$.

Taking the result as a strong indication that Markov properties hold, we want to show that the spatial statistics can be reproduced by the stochastic processes, we extracted in the previous section from the increments using a time step τ. We reconstruct from the results obtained for the point 218 data series using eq. (4.15). For a $\tau = \frac{r}{u}$ where $r = d(218, 119)$ the correspondig conditional pdf can be obtained for all components (see fig.4.16).

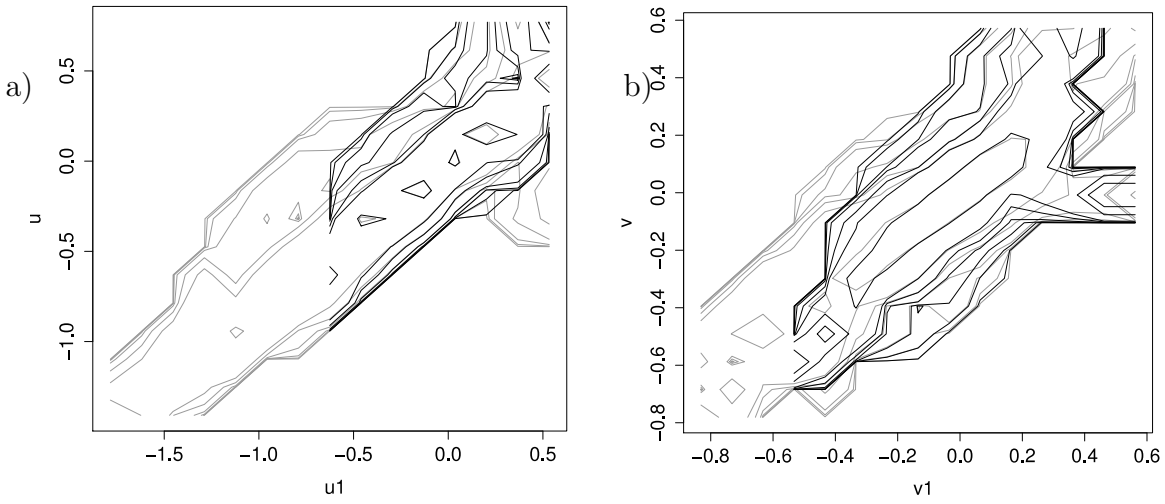

Figure 4.14: Contour-plot of conditioned pdfs of the time series $p(u_i, r_0|u_{i,1}, r_1)$ (grey) and $p(u_i, r_0|u_{i,1}, r_1; u_{i,2}, r_2)$ (black) for the u- and v-velocity increments between point r0=d(218,61), r1=d(218,13) and r2=d(218,119).

Further we compare the pdfs of the increments of $r_2 = d(218, 119)$ of the simulated data with the reconstructed increments. The results for all components are given in fig.4.17. As can been seen the spanwise flow direction was obviously the easiest to reconstructm, since there was no big difference in velocity magnitude between the two points and the original distribution was also symmetrical. For the pdfs of the u- and v-velocity increments show good agreement, even though slight deviations can be observed.

By adding the reconstructed increment to the velocity time series, one can finally resolve a reconstructed time series for the velocity at point 119:

$$u_{i,119}(t) = u_{i,218}(t) - u_{r2,rec}(t).$$

with $u_{i,218}(t)$ being the u_i-velocity component at the point 218 at the time t and $u_{r2,rec}$ the reconstructed increment for $r_2 = d(218, 119)$. Thus we are able to compare the characteristics of the original velocity at point 119 given in table 4.1 to a velocity reconstruction. Table 4.5.3 displays the results of this reconstruction. Concerning the mean, the u-velocity shows some deviation. Although the tendency of a reduction of the velocity closer to the airfoil surface is correct, this decrease is not yet large enough. On the other hand the values for the v- and w-velocity are met quite well. This contrast leads to the conclusion, that mainly the u-component had effects in the flow field which were not grasp by the Gaussian statistics. Nevertheless the results was surprisingly good as in an

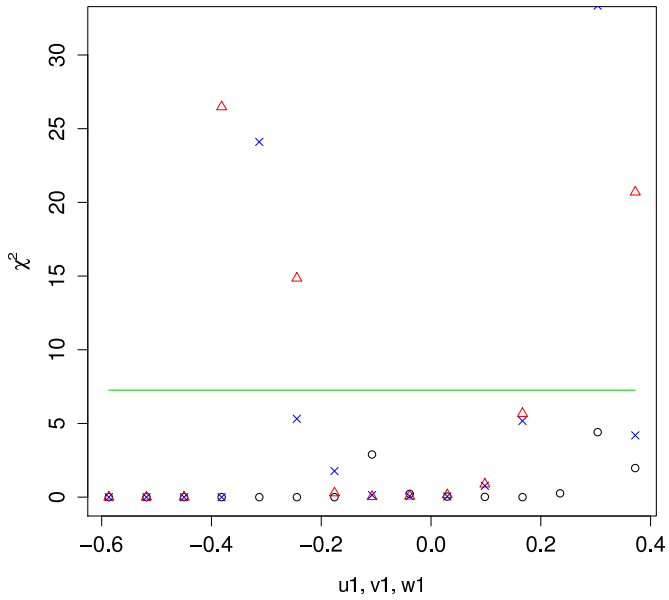

Figure 4.15: χ^2 values for the conditioned pdfs for the increments between points 218, 61, 13 and 119 with overall scales $r = 0.054$, $r_0 = 0.076$ and $r_1 = 0.088$.

Point	Component	$\overline{u_i}$	σ_i	L_i	λ_i	η_i
119-rec	x	-0.093	0.292	0.162	0.0015	0.0001
119-rec	y	-0.042	0.199	0.127	0.0005	9.4e-05
119-rec	z	-0.002	0.192	0.115	0.0002	6.8e-05

Table 4.3: Length scales, mean and standard deviation of the reconstructed time series at point 119.

inhomogeneous, anisotropic field with a physical object in the area it was possible to reconstruct the field by pure statistical analysis.

4.6 Conclusions

We analyzed a simulated flow field with the aim to gain information about the statistical properties of the field. An additional aim was the reconstruction of the statistics of the flow as it might be useful for stochastic models in computational fluid dynamics. Further the attempt was made to reconstruct the statistical property of the flow at one point from the stochastics at a different point. The field was obtained by a simulation around an airfoil using the spectral element code $\mathcal{N}\varepsilon\kappa\mathcal{T}\alpha r$.
The simulation generated a well resolved flow field with an anisotropic and inhomogeneous turbulence area in the wake of the airfoil. The resolution of the field

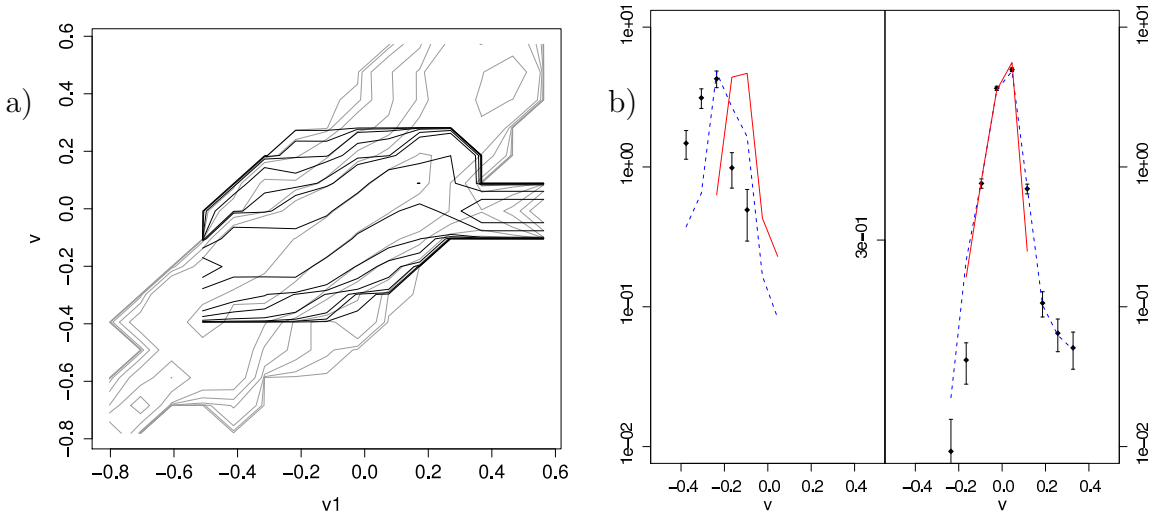

Figure 4.16: Contour-plot of conditioned pdfs of the time series $p(u_i, r_0|u_{i,1}, r_1)$ (grey) and $p(u_i, r_0|u_{i,1}, r_1; u_{i,rec}, r_2)$ (black) for the v-increments a). Slices of the plot at $+/-0.9\sigma$ for the v component. Here the dotted line represents the data from $p(u_i, r_0|u_{i,1}, r_1; u_{i,2}, r_2)$ and the solid line the data from $p(u_i, r_0|u_{i,1}, r_1; u_{i,rec}, r_2)$. The points with error bars are obtained from the data of the simulation with the errorbars being $\sqrt{N}$.

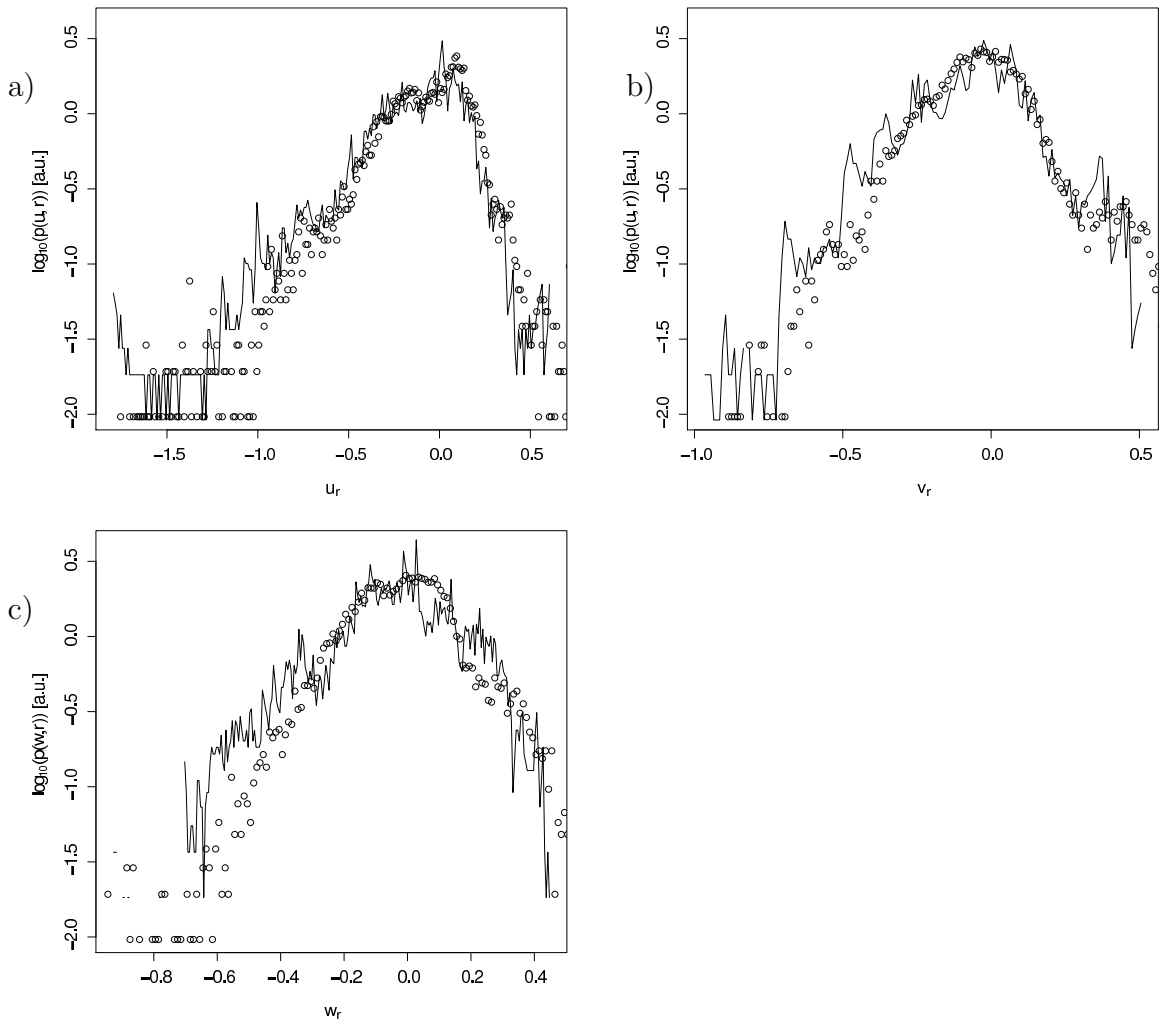

Figure 4.17: The semi-logarithmic plot of the pdf of the velocity increments for all components, where the line is the distribution resulting from the original simulation data and the dots represent the reconstructed time series.

enabled us to use the flow field for an analysis of the stochastic characteristics of the turbulent wake using n-point correlation methods with velocity increments.
In a first step the time series has been analyzed at a point within an anisotropic and inhomogeneous turbulent field in the wake of the airfoil. Although the number of data points was low, there was a strong indication that there exist Markov properties for time scales greater than a certain "Markov timescale". Applying the Taylor hypothesis, this would correspond to a Markov length of $\lambda_M = 0.011$ for the u-velocity component and $\lambda_M = 0.018$ for the v-velocity component respectively. However, due to the lack of data an uncertainty on Markov properties remains for the more rare incidences of large increments.
Assuming that Markov properties hold, the conditional moments $M^{(n)}(u, \tau, \Delta\tau)$ and Kramers-Moyal coefficients $D^{(n)}(u, \tau)$ for the time series at different $\Delta\tau$ and τ have been calculated. $D^{(4)} = 0$ was not found, however, $D^{(4)} << D^{(2)}$ was given. Hence the further analysis has been conducted under the assumption that the conditions of Pawulas theorem were met. The first two Kramers-Moyal coefficients were used for a reconstruction of the incremental time series at the analysis position.
This reconstruction of the incremental time series by a Langevin equation lead to promising results. Slight deviations were observed since we used Gaussian methods for reconstruction. Thus skewness and kurtosis did show some differences.
Further we used the obtained coefficients to estimate the structure of the flow field in real space of separated points within the inhomogeneous turbulent field by applying the Taylor hypothesis. Therefore the incremental analysis was also done using four points aligned in the wake including the original analysis point. The distance between the base point and the position of the reconstruction was about 5-8 times the Markov length scale λ_M.
The results were surprisingly good, especially for the v-velocity component. The flow field was very inhomogeneous due to the shear flow on the one side of the field and a boundary layer towards the airfoil. Thus the reconstruction was quite good considering the use of a Langevin equation just based on the statistics of the field in one point.
Since the results were promising, we do encourage further research in this area. It would be especially promising to extend the model to non Gaussian Langevin equations for the inclusion of the effect of higher order moments. It also should be investigated to which accuracy and on which scales it is possible to assume the statistics of a distant point from the statistics in another point - within an inhomogeneous filed. The results in this work give hope that such methods could lead to quite satisfying results, particularly since the dataset was still very short for the used method.
Towards the aim of implementing the method into a general stochastic turbulence model also further questions need to be answered, such as how the flow properties change in the boundary layer, the direct shear area or for different Reynolds numbers. Answering these questions should make the method implementable in

stochastic models for flow simulations as the ones proposed by Laval or Bakosi [13][16] and increase their accuracy.

Bibliography

[1] F. Richez, I. Mary, V. Gleize, and C. Basdevant. Near stall simulation of the flow around an airfoil using zonal f. richezrans/les coupling method. *Computer and Fluids*, 37(7):857–866, 2008.

[2] H.-J. Kim, S. Lee, and N. Fujisawa. Computation of unsteady flow and aerodynamic noise of naca0018 airfoil using large-eddy simulation. *International Journal of Heat and Fluid Flow*, 27:229–242, 2006.

[3] Andreas Bechmann and Niels Sørensen. Simulation of the mexico rotor wake. In *Proceedings of the EWEC 2009*, volume EWEC, 2009.

[4] Nilav Sezer-Uzol and Lyle N. Long. 3-d time-accurate cfd simulations of wind turbine rotor flow fields. In *Presented at AIAA Aerospace Sciences Meeting*, AIAA-Paper 2006-0394. AIAA, January 2006.

[5] M. Breuer, B. Kniazev, and Marcus Abel. Development of wall models for les of separated flows using statistical evaluations. *Computer and Fluids*, (36), 2007 817-837.

[6] L. Davidson, D. Cokljat, F. Fröhlich, A. Leschziner, C. Mellen, and W. Rodi, editors. *LESFOIL Large Eddy Simulation of Flow Around a High Lift Airfoil*, volume 83 of *Notes on Numerical Fluid Mechanics*. Springer Verlag, 2003.

[7] Charles Meneveua and Joseph Katz. Scale-invariance and turbulence models for large-eddy simulationjoseph. *Annual Reviews in Fluid Mechanics*, 32:1–32, 2000.

[8] Andreas Muschinski, Rod G. Frehlich, and Ben B. Balsley. Small-scale and large-scale intermittency in the nocturnal boundary layer and the residual layer. *J. of Fluid Mech.*, 515:319–351, 2004.

[9] Rudolf Friedrich and J. Peinke. Statistical properties of a turbulent cascade. *Physica D*, 102(147):147–155, 1997.

[10] Ihor Lubashevsky, Rudolf Friedrich, and Andreas Heuer. Continuous-time multidimensional Markovian description of levy walks. *Physical Review E*, 80(3), September 2009.

[11] R. L. S. Farias, Rudnei O. Ramos, and L. A. da Silva. Stochastic langevin equations: Markovian and non-Markovian dynamics. *Physical Review E*, 80(3), sep 2009.

[12] A. S. Monin and A. M. Yaglom. *Statistical Fluid Mechanics: Mechanics of Turbulence*, volume 2. The MIT Press, 1975.

[13] Jean-Philipe Laval and B. Dubrulle. A les-langevin model for turbulencb. dubrulle. *The European Physical Journal B*, 47(4):471–481, Febuary 2006.

[14] B. Dubrulle, Jean-Philipe Laval, S. Nazarenko, and O. Zaboronski. A model for rapid stochastic distortions of small-scale turbulence. *J. of Fluid Mech.*, 520:1–21, 2004.

[15] Jean-Philipe Laval, B. Dubrulle, and J. C. McWilliams. Langevin models of turbulence: Renormalization group, distant interaction algorithms or rapid distortion theory? *Physics of Fluids*, 15(5):1327–1339, May 2003.

[16] J. Bakosi, P. Franzese, and Z. Boybeyi. A non-hybrid method for the pdf equations of turbulent flows on unstructured grids. *Journal of Computational Physics*, 227:5898–5935, 2008.

[17] S. B. Pope. The vanishing effect of molecular diffusivity on turbulent dispersion: implications for turbulent mixing and the scalar flux. *J. of Fluid Mech.*, 359:299–312, 1998.

[18] Babak Shotorban and Farzad Mashayek. A stochastic model for particle motion in large-eddy simulation. *Journal of Turbulence*, 7(18), January 2006.

[19] R. O. Fox. On velocity-conditioned scalar mixing in homogeneous turbulence. *Physics of Fluids*, 8(10):2678–2691, 1996.

[20] R. O. Fox and P. K. Yeung. Improved lagrangian mixing models for passive scalars in isotropic turbulence. *Physics of Fluids*, 15(4):961–985, 2003.

[21] Rudolf Friedrich and J. Peinke. Description of a turbulent cascade by a Fokker-Planck equation. *Phys. Rev. Lett.*, 78(5):863–866, 1997.

[22] Christoph Renner, Joachim Peinke, and Rudolf Friedrich. Markov properties of small scale turbulence. *J. Fluid Mech.*, 433:383–409, 2001.

[23] Frank Böttcher, Joachim Peinke, Rudolf Friedrich, David Kleinhans, Pedro G. Lind, and Maria Haase. Reconstruction of complex dynamical systems affected by strong measurement noisepedro g. lind. *Phys. Rev. Lett.*, 97, 2006.

[24] M. Tutkun and L. Mydlarski. Markovian properties of passive scalar increments in grid-generated turbulence. *New Journal of Physics*, 6(49), 2004.

[25] Robert M. Kirby, Tim Warburton, Spencer J. Sherwin, A. Beskok, and George Em Karniadakis. *Dynamic Simulations without Remeshing*, volume 397-1 of *Computational Technologies for Fluid/Thermal/Structural/Chemical Systems with Industrial Apllications*. ASME, 1999.

[26] George Em Karniadakis and Spencer Sherwin. *Spectral/hp Element Methods for Computational Fluid Dynamics*. Numerical Mathematics and Scientific Computations. Oxford University Press, Oxford, 2nd edition, 2005.

[27] George Em Karniadakis, S. A. Orszag, and M. Israeli. High-order splitting methods for the incompressible Navier-Stokes equations. *Journal of Computational Physics*, 97:414–443, December 1991.

[28] Bernhard Stoevesandt, Andrei Shishkin, Claus Wagner, and Joachim Peinke. Direct numerical simulation of the turbulent flow around an airfoil usig spectral/hp method. In P. Wessling, E. Onate, and J. Periaux, editors, *European Conference on Computational Fluid Dynamics ECCOMAS CFD 2006*, 2006.

[29] Tim Warburton. *Spectral/hp Methods on Polymorphic Multi-Domains: Algorithms and Applications*. PhD thesis, Brown University, 1999.

[30] X. Ma, G.-S. Karamanos, and G.E. Karniadakis. Dynamics and low-dimensionality of a turbulent near wake. *Journal of Fluid Mechanics*, 410:29–65, 2000.

[31] S. Dong, G.E. Karniadakis, A. Ekmekci, , and D. Rockwell. A combined direct numerical simulation - particle image velocimertry study of the turbulent near wake. *J. of Fluid Mech.*, 569:185–207, 2006.

[32] H. Risken. *The Fokker-Planck Equation*. Springer Verlag, 1996.

[33] Andreas P. Nawroth and Joachim Peinke. Multiscale reconstruction of time series. *Physics Letters A*, 360:234–237, 2006.

[34] Stephen B. Pope. *Turbulent Flows*. Cambridge University Press, 2000.

[35] I. N. Bronstein and K.A. Semendjajew. *Taschenburch der Mathematik*. Teubner, 25. edition, 1991.

[36] Stephan Lück, Christoph Renner, Joachim Peinke, and Rudolf Friedrich. The Markov-Einstein cohernce length - a new meaning for the Taylor length in turbulence. *Physics Letters A*, 359:335–338, 2006.

Chapter 5

Effects of Sudden Changes in Inflow Conditions on the Angle of Attack on HAWT Blades[1]

In this paper changes in wind speed and wind direction from a measured wind field are being analyzed at high frequencies. This is used to estimate changes in the angle of attack (AOA) on a blade segment over short time periods for different estimated turbine concepts. Here a statistical approach is chosen to grasp the characteristics of the probability distributions to give an over all view of the magnitude and rate of the changes. The main interest is the generation of basic distributions for the calculation of dynamic stall effects and stall flutter due to wind fluctuations.

5.1 Introduction

Dynamic stall is a concept to calculate strong, yet hard to predict, load fluctuations on wind turbines. One of the main causes for dynamic stall and stall flutter on wind turbines are sudden changes in wind speed and wind direction leading to changes in the angle of attack (AOA) on wind turbine blades. Both angle of attack and dynamic stall are part of the 2D calculation concept used by most blade element moment (BEM) or lifting line model theory programs to calculate the main aerodynamic properties for wind turbines [1][2]. Dynamic stall is mostly taken into account by empirical models based on the knowledge of the amplitude and fequency of the changes in the angle of attack [3].
Most of the research on the dynamic stall models evolved from helicopter research like the ONERA model [4] or the Beddoes-Leishman model [5] and

[1]Prepared to be submitted as B. Stoevesandt and J. Peinke: *Effects of Sudden Changes in Inflow Conditions on the Angle of Attack on HAWT Blades* to Wind Energy.

were later transfered to wind turbine applications. At helicopters dynamic stall mainly appears due to a rapid change in AOA induced by a - from the rotor perspective - yawed inflow [6] caused by the flight velocity. The changes in AOA and its rates of change are periodic in time and thus can easily be calculated. Such change rates are also often used for wind turbine dynamic stall modeling [7][8].

In case of a natural wind field the situation is different, as changes in the AOA are induced by the incident wind field which appears in most cases to be highly turbulent. To calculate the amplitudes and frequencies of changes in AOA the distributions of changes in wind direction and wind speed have to be investigated.

The fluctuations of the wind has attracted attention in research in recent years (e.g. [9][10][11]). The investigation on the influence of such fluctuations on the AOA is a relevant consequence. Bierbooms and Veldkamp did some research on wind speed fluctuations and the resulting loads on wind turbines [12][13].

For the load estimation on wind turbines, so far wind field generators using a wind field based on a Gaussian distributed wind speed fluctuations are applied quite often (e.g. [14][15][16][17]). This Gaussian approach leads to an underestimation of extreme values of the fluctuations in wind speeds (see e.g. [18]).

Changes in wind direction lead to a yawed inflow condition, which is one reason for wind turbines to face dynamic stall effects [19][20]. The analysis of wind directional changes has been described by van Doorn et al. [21]. The methods are picked up in this paper and applied to a measured wind field for further statistical analysis.

If the fluctuations in wind speed and changes in wind direction would be strongly correlated, it would be straight forward to develop a comprehensive analytical model for the fluctuations in the AOA. However this does not often seem to be the case [22]. Therefore we propose a direct calculation of the fluctuations in the AOA from changes in both, the wind speed and the wind direction.

Due to the unsteadiness of the wind field and the response of the wind turbine, the actual AOA is hard to determine. Different approaches to resolve this problem have been proposed [23][24][25][26]. In this paper we assume that the actual AOA is unknown. Yet the changes in the AOA due to changes in wind speed and wind direction are evaluated. We do so by estimating the changes in the AOA over short period of time. Therefore will assume certain simplified models for such changes on an arbitrary chosen position on a rotating blade.

Here we will explain the methodology to calculate the local changes in the AOA, using a measured wind field as input. At first a short analysis of the wind field data will be. Next, for two different wind turbine modeling principles, the changes in AOA are calculated and analyzed. Included is an analysis of the changes in AOA only due to changes in wind direction. In the end an analysis of the time scales on which the changes appear and the characteristics of their

distribution are presented with the aim to improve the investigation of dynamic stall effects and their modeling for wind turbines.

5.2 Characteristics of the measured wind

Before we present a method to calculate the changes in AOA, the measured wind field we used for the demonstration shall be discussed here on the bases of its statistical aspects.
The data from a measurement campaign at a wind farm at Meerhof near Paderborn in Germany is being used throughout this paper [27]. The data was measured using a Gill R3-50 ultra sonic anemometer in 98m height with a sampling rate of 50 Hz. If not otherwise stated, it has been averaged to a 10 Hz sampling rate. Using the Taylors frozen turbulence hypothesis this sampling rate corresponds to a length scale of 1 m at a wind speed of 10 m/s. Wind coming from the sector from 40.5° to 133.5° has been excluded from the analysis, since a wind farm was near in these wind directions. This way an influence by the wake of the wind farm on the wind measurement could be avoided. For the investigation a dataset of seven consecutive days from December 1st to 7th, 2005 has been used, leading to a dataset of $6 \cdot 10^6$ samples at 10 Hz.

We proceed with different relevant characteristics of the wind field and the description of methods for the characterization of turbulent fluctuations.
The mean measured wind speed over all data was $\bar{u} = 6.96$ m/s with a turbulence intensity of $I = 13.3\%$ according to IEC-61400-1 Standard [28], calculated from the average standard deviation of 10 minutes periods.
For the further calculations some approximations have been made. We exclude wind speeds of $|u| < 2$ m/s in the analysis. Changes in wind direction at low wind speeds are very sensitive to measurement errors. Very low wind speeds are also irrelevant for wind turbines, due to the lack of induced relevant loads.
Since the dataset consisted only of one point measurements, we will also make the assumption for the calculations that the wind field and its turbulence is homogeneous. Even if this is in reality not the case, implementing a different wind field on the method will be straight forward.
For the research of dynamic stall we are mainly interested in the extend of the changes at certain periods. Therefore the wind field and its turbulent structure was further analyzed using incremental statistics. They are a good measure for fluctuations at time steps τ. Increments of a property $\xi(x,t)$ are defined as

$$\xi_\tau(x) = \xi(x, t+\tau) - \xi(x,t) \quad . \tag{5.1}$$

where τ is the time scale to be considered. The statistics of the increments allow a time scale resolved analysis of the fluctuations of a magnitude ξ in time.

For the measured data the probability density function (pdf) of the wind speed increments for a time scale of τ=10 Hz is given in fig. 5.1 in semi-logarithmic presentation. We observe a typical intermittent behavior of the pdfs, which has been described e.g. by Böttcher [18]. The distribution deviates strongly from a fitted Gaussian curve. In our case the empirical probability of wind speed changes at 10 Hz and of magnitude 0.85 m/s is already by a factor $\geq 10^4$ higher than a corresponding Gaussian distribution would predict. For larger increments this deviance increases by further orders of magnitude.

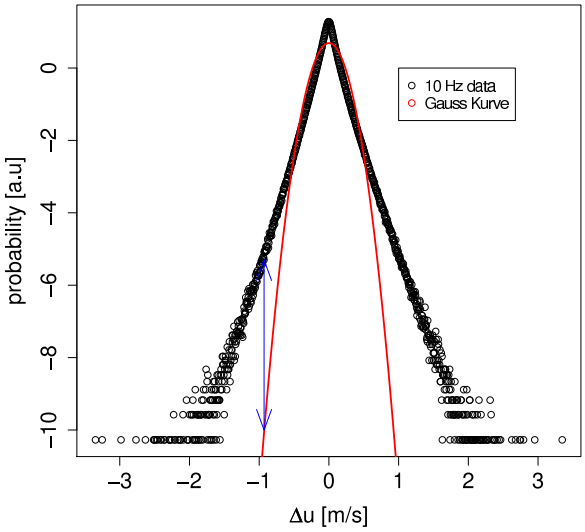

Figure 5.1: Probability density function (pdf) of all wind speed increments for $\frac{1}{\tau} = 10$ Hz. The typical intermittent behavior is seen by the strong deviations of the tails from a fitted Gaussian distribution. Here like for all other plots we used only wind speeds at $|u| \geq 2$ m/s.

The deviance from a Gaussian curve can be quantified by the kurtosis and the skewness, where the kurtosis can be used to describe a symmetric deviation from a Gaussian curve and the skewness to describe the asymmetry of the curve. In this paper the excess kurtosis is taken into account given by

$$\gamma = \frac{\frac{1}{n}\sum_{i=1}^{n}(x_i - \overline{x})^4}{(\frac{1}{n}\sum_{i=1}^{n}(x_i - \overline{x})^2)^2} - 3 \quad . \tag{5.2}$$

The excess kurtosis is normed so that $\gamma = 0$ for a Gaussian distribution and $\gamma > 0$ for intermittent pdfs.
The skewness is calculated by the standardized third moment:

$$\nu = \frac{\frac{1}{n}\sum_{i=1}^{n}(x_i - \overline{x})^3}{(\frac{1}{n}\sum_{i=1}^{n}(x_i - \overline{x})^2)^{\frac{3}{2}}} \quad . \tag{5.3}$$

It follows that $\nu = 0$ for symmetrical pdfs.
For a characterization of the wind field, we can determine the pdfs of the wind speed increments at different time scales τ (see fig. 5.2). In fig. 5.2 b) the corresponding values of the excess kurtoses are shown as a function of time scales between 0.1s and 3s is shown. With an increase in time period of wind speed increments γ becomes smaller, which means that the shape of the pdfs approach slowly the shape of a Gaussian curve. A linear regression indicates a characteristic $\gamma \approx \tau^{-0.21}$. An extrapolation would lead to a kurtosis of a Gaussian curve at a time scale of 150 s. This is however a time scale far above the scales at which most control systems adapt wind turbines to the surrounding conditions. Thus it is of no further interest for our considerations here.

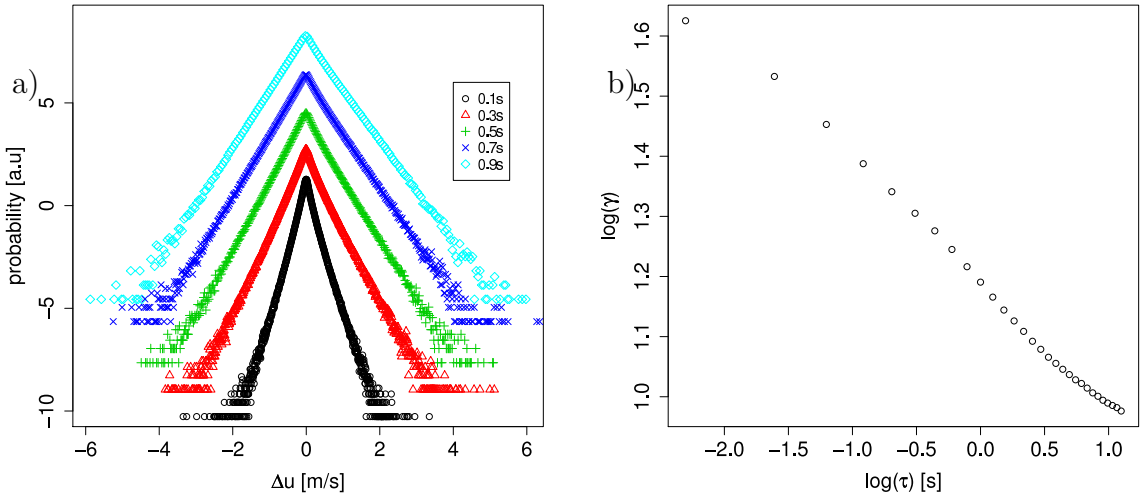

Figure 5.2: pdfs wind speed increments for different time scales τ on a semi-logarithmic scale a). The values of the excess kurtosis of the pdfs give an idea of the magnitude of the deviation from Gaussian distributed pdfs with a $\gamma = 0$.

So far we have look just at the wind speed $|u|$ and its increments. For our purpose it is also important to take the wind direction ϕ and its increments into account.
The pdfs of the increments of the wind direction show again an intermittent form (see fig. 5.3). The values of the excess kurtoses are lower than for the wind speeds. Fig. 5.3 makes clear, that wind direction changes are large and appear rapidly. Changes of 10° and more within 0.1 seconds do occur. For larger time scales, still less 1 second, changes of up to 20° occur. The double logarithmic presentation of the excess kurtoses in fig. 5.3 b) leads to a similar power law with $\gamma \approx \tau^{-0.42}$ for scales $0.5 \leq \tau \leq 3.0$. An interpolation leads to a kurtosis of a Gaussian curve at $\tau \approx 4.6$ s.

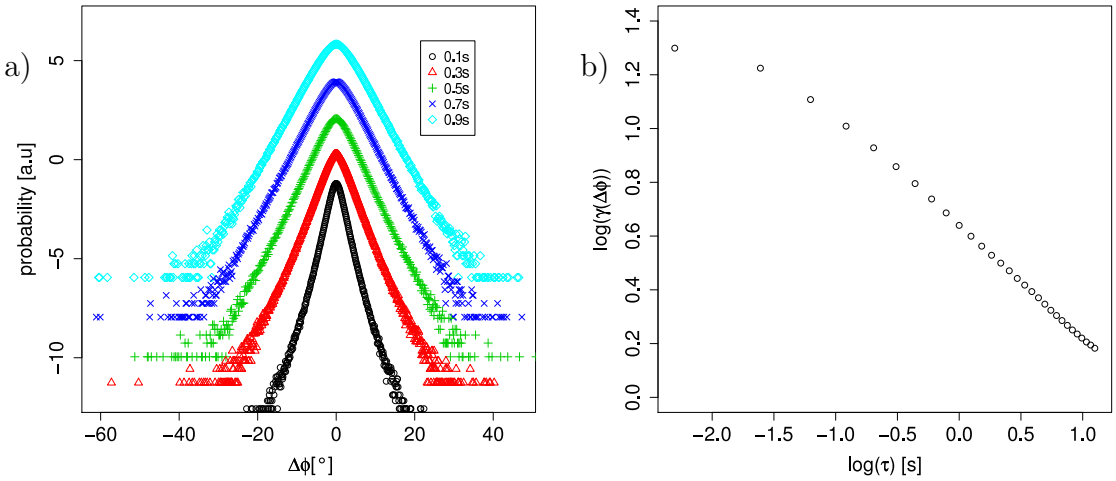

Figure 5.3: a) probability density functions of wind direction increments at different time scales on a semi-logarithmic scale and b) the excess kurtoses.

As both changes in wind speed and in wind direction can cause changes of the angle of attack, the correlation of the appearances of both phenomena is of particular interest. A possible measure to quantify this is the so called gust directional index (GDI)

$$GDI(\tau) = \frac{abs(u(t+\tau) - u(t))}{max(abs(u(t+\tau) - u(t)))} + \frac{abs(\phi(t+\tau) - \phi(t))}{max(\phi(Dir(t+\tau) - \phi(t)))}, \qquad (5.4)$$

as introduced by Hansen et al. [22]. Here $u(t)$ is the wind speed at time t, τ is the time scale and $\phi(t)$ the wind directione. The $GDI \in [0, 2]$ takes into account two simultaneous increments $u_\tau(t)$ and $\phi_\tau(t)$, with $GDI(\tau) = 2$ if both magnitudes show extreme events occurring in a correlated way and $GDI(\tau) = 0$ for complete non-correlation. For quantification the probability of strongly correlated events is regarded [22].
For an 1 Hz sampling rate the probability of the $GDI \geq 1.98$ for $\tau = 10$ s was at $1.3 \times 10{-}5$. For a sampling rate of 10 Hz this value for $\tau = 10$ s decreases to 1.5×10^{-7}. It seems a large simultaneous change in wind speed and direction is not likely to appear, the numbers of large GDI events are comparatively low.
The low values indicate for the question of the changes in angle of attack, that changes in wind speed and direction could mostly be considered separately for this wind field. Nevertheless this does not seem to be the case for all wind situations (compare [22]).

5.3 Analysis of fluctuations in the AOA

5.3.1 The calculation concept

Instead of focussing on aspects of the wind field components separately we proceed to calculate the changes in AOA by a comprehensive approach. To do so a model of an estimated wind turbine is need. The real AOA on wind turbines is strongly dependent on its control system. Here we do not intend to go into details of a specific control system. Instead we consider two different simplified cases:

a) A classical fixed tip speed ratio turbine that adapts tip speed and pitch angle to the changes in the averaged wind of a certain period τ_a by a fast controlling system. We will take here $\tau_a = 2$ s.

b) A turbine with a fixed rotational speed, that adapts the pitch angle to the averaged wind of the last 2 seconds.

The models will further be labeled as case a) or b) respectively.
For all cases of the models we find a finite time τ_a for the control system to pose a wind turbine in its optimal working condition. In case of wind changes on time scales $\tau \leq \tau_a$ the control system is not able to react quickly enough. For these situations the fluctuations of the wind conditions e.g. grasped by increments are of importance. This aspect will be studied in the following.
The used estimations of turbines enable us to determine a change in AOA by

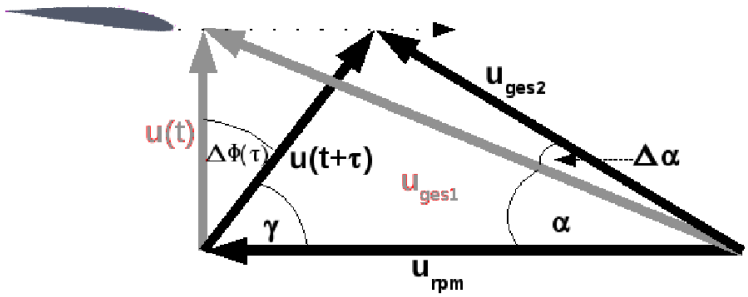

Figure 5.4: The changing AOA can be calculated by the law of cosines. In grey is the original wind velocity and direction - black is the new one after a time τ.

a change in wind situation. Such changes can then be calculated by using the geometry shown in fig. 5.4, where

$$\Delta\phi = \phi(t+\tau) - \overline{\phi}(t). \tag{5.5}$$

Here $\overline{\phi}(t)$ is the averaged angle between the incoming wind and the rotor plane determined by the "slow" yaw system.

The general equations for the changing AOA $\Delta\alpha$ in fluctuating winds are, in case a) of the fixed tip speed ratio turbine

$$\Delta\alpha = \arccos\left(\frac{\overline{u}(t)\frac{\lambda_T r}{R} - \frac{2}{3}u(t+\tau)\sin(\Delta\phi)}{\sqrt{(\overline{u}(t)\frac{\lambda_T r}{R})^2 + (\frac{2}{3}u(t+\tau))^2 - \frac{4}{3}u(t+\tau)\overline{u}(t)\frac{\lambda_T r}{R}\sin(\Delta\phi)}}\right) - \arctan\left(\frac{2}{3}\frac{1}{\frac{\lambda_T r}{R}}\right). \quad (5.6)$$

For the fixed rotational speed turbine case b) we use

$$u_{rpm} = \frac{2\pi r n_r}{60} \quad (5.7)$$

where n_r is the rotational speed in number of rounds per minute. For turbines with a rotor radius of $R = 40$ m, typical values of n_r lay between 10 and 20. Thus we obtain:

$$\Delta\alpha = \arccos\left(\frac{u_{rpm} - \frac{2}{3}u(t+\tau)\sin(\Delta\phi)}{\sqrt{u_{rpm}^2 + (\frac{2}{3}u(t+\tau))^2 - \frac{4}{3}u(t+\tau)u_{rpm}\sin(\Delta\phi)}}\right) - \arccos\left(\frac{u_{rpm}}{\sqrt{u_{rpm}^2 + (\frac{2}{3}\overline{u}(t))^2}}\right). \quad (5.8)$$

Here in both cases $u(t)$ is the absolute value of the wind velocity at the time t, λ_T is the tip speed ratio, which was taken to be 7 for case a). R is the total rotor radius, which is considered to be $R = 40$ m in this paper. r is the position of the blade, which is to be regarded. The factor of $\frac{2}{3}$ in both equations reflects the estimated deceleration of the wind due to the blockage effect.
All calculations were done at a position of half of the blade length $r = 20$ m. Although the absolute changes in AOA depend on r, the form of the distributions of the increments do not.

5.3.2 Overall estimation of changes in AOA

In fig. 5.1 and fig. 5.3 we can conclude that the timescales of rapid fluctuations do not differ very much between wind speed change and wind direction change. Further we can conclude from the low value of the GDI in section 5.2 that we cannot expect a strong correlation of the fluctuations in wind speed and wind direction. Therefore it makes sense to investigate the changes in the AOA by

regarding the over all change in wind speed and direction at the same time, calculated by equations (5.6) and (5.8).
Here the models for case a) (const. tip speed) and case b) (constant u_{rpm}) are taken into account. We use $\tau_a = 2$ s. We use $\tau_a = 2$ s. Fig. 5.5 presents the pdfs of the increments $\Delta\alpha$ for both cases, in a) with $u_{rpm} = 20$ in b) $u_{rpm} = 10$ representing the limits of the range of rotational speed for a typical R=40 m turbine. To emphasize the difference in shape of the pdfs between the two cases a) and b) the results have been plotted together for each u_{rpm}.

The pdfs in fig. 5.5 for both assumed models of the turbines show a strong

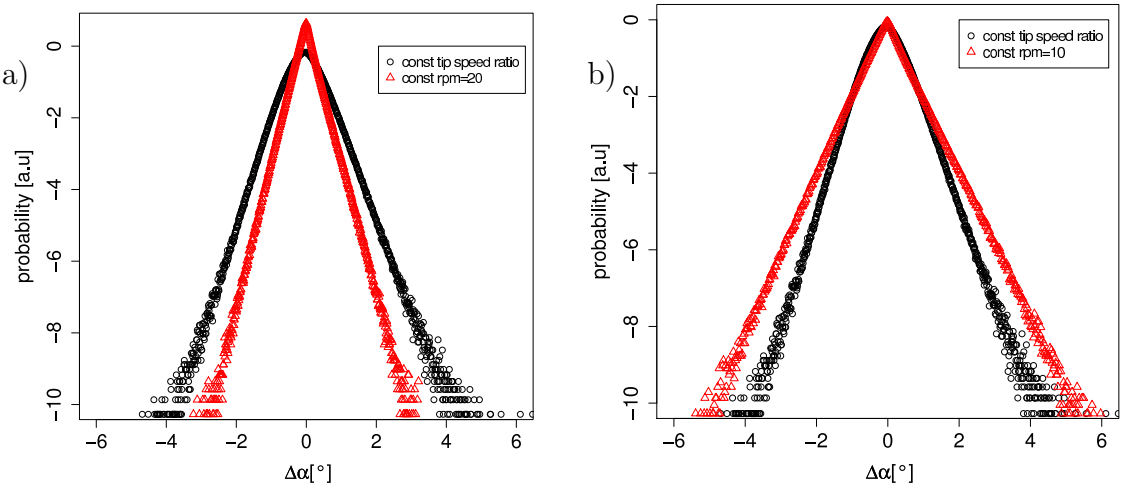

Figure 5.5: Pdfs of the changes in AOA due to change in wind over the period of $\tau_a = 2s$. In both figures a) and b) the changes of the calculations for constant rotational speed against (case b)) constant tip speed ratio (case a)) are given. In figure a) the const. rotational speed is given by a rotation of $n_{rpm} = 20$, whereas in fig. b) $n_{rpm} = 10$. Note that the pdf of case a) with depicted by the round symbols is the same in both plots.

intermittent structure. In case of the case a) turbine with constant tip speed ratio, the intermittency is less distinct. This is also quantified by the kurtoses of the pdfs in table 5.1. The kurtosis of the case a) pdf is much lower yet the standard deviation σ is relatively high compared to the pdfs of case b). The reason lies in the adaption of the case a) turbine rotation to the wind speed filtering some of the extreme fluctuations.
Further a slight asymmetry in the pdfs could be observed which are quantified by the skewness in table 5.1. Since the fluctuations in wind speed should not cause such an asymmetry, this effect should be a result from the changes in wind direction. To quantify the influence of the changes in wind direction on the pdfs of the changes in angle of attack, we will proceed to analyze this effect separately.

Type	Skewness	Kurtosis	σ
$\lambda_T = 7$	0.20	1.8	0.59°
$n_{rpm} = 10$	0.16	3.1	0.71°
$n_{rpm} = 20$	0.17	3.2	0.36°

Table 5.1: Characterization of the pdfs for the change in AOA due to wind fluctuations - including wind speed and direction.

5.3.3 Maximum changes of attack due to sudden yaw angle changes

In the following we analyze the effect of the changes in wind direction on the changes in angle of attack.
We regard the maximum changes in AOA under the following conditions: The wind speed is expected to be constant, the averaging period $\tau_a = 2$ s and $\lambda_T = 7$ for case a) and $n_r = 10, 15, 20$ rpm for the case b) model. Thus for the $n_r = 15$ case a rotor blade would perform half a revolution.
Using these assumptions the model equations (5.6) and (5.8) change to

$$\Delta\alpha = \arccos\left(\frac{\frac{\lambda_T r}{R} - \frac{2}{3}\sin(\Delta\phi)}{\sqrt{(\frac{\lambda_T r}{R})^2 + (\frac{2}{3})^2 - \frac{4}{3}\frac{\lambda_T r}{R}\sin(\Delta\phi)}}\right) - \arctan\left(\frac{2}{3}\frac{1}{\frac{\lambda_T r}{R}}\right), \tag{5.9}$$

for turbines with constant tip speed ratio and to

$$\Delta\alpha = \arccos\left(\frac{u_{rpm} - \frac{2}{3}\overline{u}(t)\sin(\Delta\phi)}{\sqrt{u_{rpm}^2 + (\frac{2}{3}\overline{u}(t))^2 - \frac{4}{3}\overline{u}(t)u_{rpm}\sin(\Delta\phi)}}\right) - \arccos\left(\frac{u_{rpm}}{\sqrt{u_{rpm}^2 + (\frac{2}{3}\overline{u}(t))^2}}\right) \tag{5.10}$$

for a turbine at a constant rotational speed.
Using $\Delta\phi(\tau_a)$ we obtain the pdfs for the changes in AOA presented in fig. 5.6.

The pdfs for the AOA in fig. 5.6 show a remarkable difference between the case of a turbine running at constant tip speed ratio and the turbine running at constant rotational speeds. Due to the constant ratio between the wind speed and the rotational speed the pdf of the case a) model shows a distribution

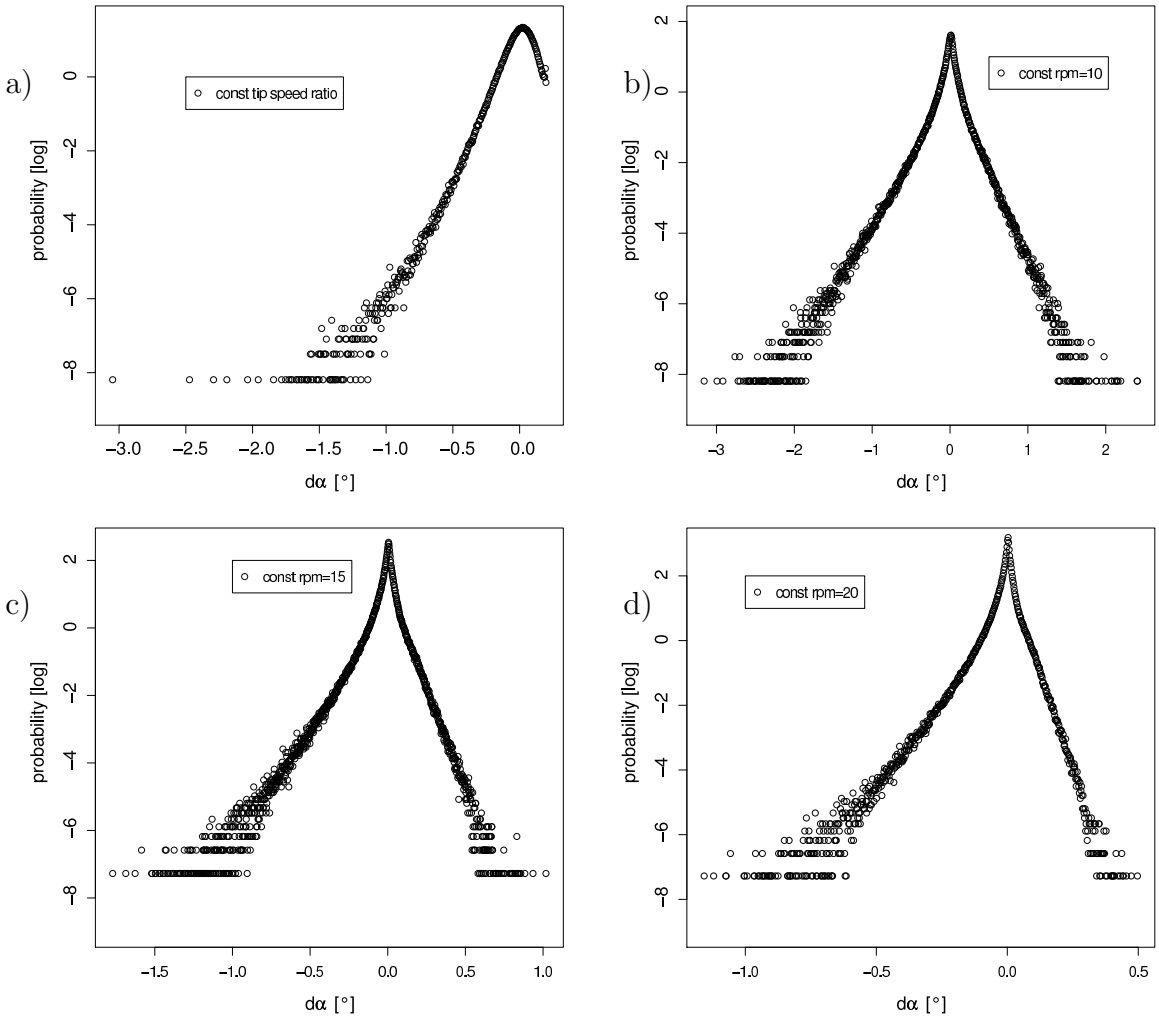

Figure 5.6: Pdf of the changes in AOA due to change in wind direction within 2 s. a) depicts the case a) of the turbine with a constant tip speed ration. The figures b), c) and d) show the pdfs for the case b) model rotating at a constant speed of $n_{rpm} = 10$, 15 and 20 rpm respectively.

Type	Skewness	Kurtosis	σ
$\lambda_T = 7$	-1.7	7.5	0.28°
$n_{rpm} = 10$	-0.9	8.2	0.23°
$n_{rpm} = 15$	-1.6	10.9	0.11°
$n_{rpm} = 20$	-2.2	14.1	0.06°

Table 5.2: Characteristics of the pdfs of $\Delta\alpha$ due to change in wind direction

limited towards positive deviations. While the pdfs for the case b) model show an intermittent curve, which is strongly asymmetric. The base functions (5.9) and (5.10) lead to a higher scatter toward negative angles in all cases. As a result all pdfs in the graphs have a negative skewness and very high values for the kurtoses given in table 5.2. Comparing the characteristics of the pdfs in table 5.2 to the values of the pdfs obtained for the complete wind field in table 5.1, we conclude that the influence of the changes in wind direction on the changes in AOA are small.

5.4 Deeper analysis of the statistics of $\Delta\alpha$

To develop models for the fluctuations in the AOA, the rate of the changes over time have to be regarded. This helps to derive a model for the turbulence of the changes in the AOA and as a result realistic estimations of extreme values. Also the rates of $\Delta\alpha$ over time is of major interest for dynamic stall modelling. Therefore the fluctuation of an estimated AOA at different time scales were calculated. To gain a quantative image of the magnitude of the time scales of fluctuations in angle of attack, instantaneous changes in the AOA without averaging have to be regarded. Therefore here a modified (case c)) version of equation (5.8) is being used for the further calculations. Thus only a comparison between the current wind and the one at a time different τ is done, so that $\overline{\phi}(t)$ and $\overline{u}(t)$ have to be replaced by $\phi(t)$ and $u(t)$ in equations (5.5) and (5.8) respectively. The time scale was henceforth varied from 10 to $\frac{1}{3}$ Hz.

It can be seen in fig. 5.7 a) a main portion of the changes in $\Delta\alpha$ appear to evolve at short time periods. For the characterization of the distributions we plotted the kurtosis over the time scales in fig. 5.7 c). It can be observed that the kurtosis of the pdfs shrinks only slowly for time scales of 10 - $\frac{1}{3}$ Hz. As an example of the deviation from a Gaussian distribution fig. 5.7 b) depicts the distribution for a time scale of $\tau = \frac{1}{10}$ s.
The knowledge of the pdfs make reconstructions of such distributions by analytical models in case of wind speed distributions possible [29]. If such models are

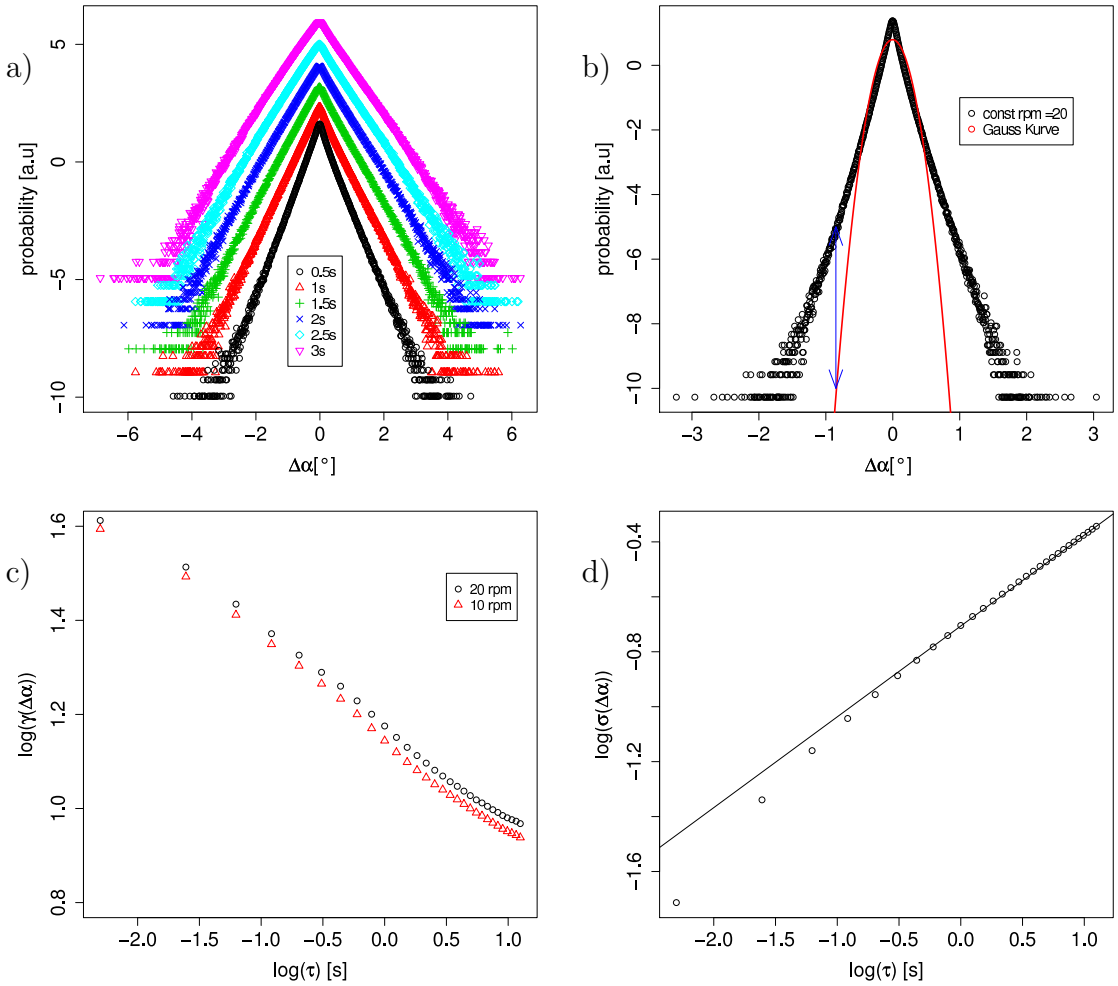

Figure 5.7: The pdfs for different time scales are given in a). As expected $\Delta\alpha$ tends to be broader for longer time scales. The pdfs remain nevertheless intermittent all the time. Fig. b) depicts the pdf of the $\frac{1}{10}$ s time scale against a Gaussian curve. Both figures a) and b) are calculated for a fixed rotation of $n_{rpm} = 20$ rpm. The rate of the intermittency over the time scale is given by the kurtosis in fig. c) for fixed rotations of $n_{rpm} = 10$ rpm and $n_{rpm} = 20$ rpm respectively. Fig. d) shows the broadening of pdfs by its standard deviation and the time scale τ. The line in d) depicts the slope of a linear function of $\frac{1}{3}$ for the case of $n_{rpm} = 20$.

applicable also to the change in AOA $\Delta\alpha$, they can further be used to optimize models for dynamic stall on wind turbines. Castaing et. al. proposed to fit the pdfs of Δu to a function that would for $\Delta\alpha$ look like

$$P(\Delta\alpha_\tau) = \frac{1}{2\pi\lambda}\int_0^\infty exp\left(-\frac{\Delta\alpha_\tau^2}{2\sigma^2}\right) exp\left(-\frac{ln^2(\sigma/\sigma_0)}{2\lambda^2}\right)\frac{d\sigma}{\sigma^2} \tag{5.11}$$

where σ_0 is the most probable variance of $\Delta\alpha$ [30]. By determining the λ we thus gain the analytical fit function $P(\Delta\alpha_\tau)$ of the pdf for the time scale τ. Since λ^2 can be taken from

$$\lambda^2 \propto ln(\gamma), \tag{5.12}$$

the knowledge of the different statistical properties as $\sigma(\tau)$ and $\gamma(\tau)$ is essential, they describe the pdfs at different conditions. In the following they shall be described in more detail to give an overview over the characteristics of the pdfs. The distribution of the pdfs given in fig. 5.7 a) only broaden at a mediocre rate as the time scale increases. In fig. 5.7 d) the double logarithmic plot the standard deviations σ of the pdfs of $\Delta\alpha$ over the different time scales are shown. For time scales $\tau \geq 0.6$ s the broadening of the standard deviation can be well described by a power law of $\sigma \approx \tau^{\frac{1}{3}}$. If we assume the Taylor hypothesis to be valid in that range

$$\Delta\vec{r} = <\vec{u}>\Delta t, \tag{5.13}$$

the slope of the curve in fig. 5.7 d) coincides with the turbulence theory of Kolomogorov from 1941 for isotropic and homogeneous turbulence [31] in case of the second structure function, stating

$$S_u^n(r) \propto r^{\frac{n}{3}}. \tag{5.14}$$

Here S is the structure function of the n-th order. As the variance is the structure function of the 2-nd order, $\sigma \propto r^{\frac{1}{3}}$ could be expected for Gaussian turbulence. So even though the overall pdfs for the change in angle of attack for time scales $0.6 \leq \tau \leq 3.0$ s show a non Gaussian behavior, the relations for the structure function for these time periods behave according to [31] like a Gaussian distribution.
A possible reason for this could be, that the overall distribution consists of a superposition of many mainly almost Gaussian distributions. In fig. 5.8 the pdfs and the kurtoses over time scales are shown for wind speeds under the restricting condition $6 \leq |u| \leq 8$ m/s. Already the pdfs can clearly be identified to be a lot closer to a Gaussian shape then it was the case for the non-conditioned wind speed in fig. 5.7a). Though $\tau \leq 2$ s the kurtosis of the pdfs is still positive, it is a lot smaller than for the over all wind field. This explains why obviously equation (5.14) is in our case still valid.
As could be seen in fig. 5.7, for time scales $\tau < 0.6$s the relation of equation

(5.14) does not hold anymore. This is also reflected for the conditioned pdfs in fig.5.8 for small time scales $\tau \leq 0.5$ s. The kurtoses do not decrease or approach a value close to $\gamma = 0$.
Using this background it is a reasonable attempt to fit a reconstructed pdf to the data to gain an analytical function with equation (5.11) for the distribution. Such a fit has been done for the conditioned pdfs in fig. 5.8 a). The pdfs give to a good extend the characteristics of the changes in the angle of attack at a certain position of a wind turbine blade within a given period of time.
Since for the calculation of dynamic stall not only the magnitude, but also the

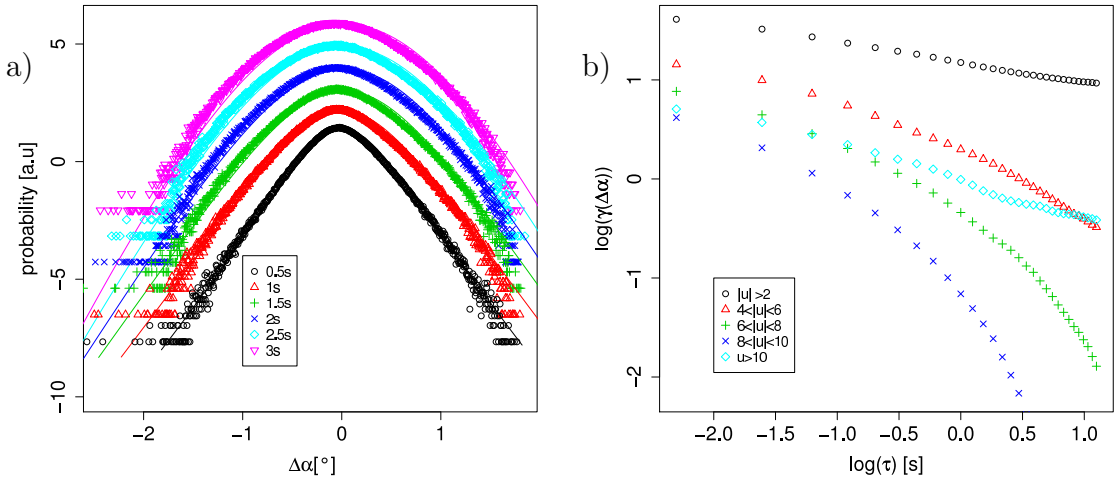

Figure 5.8: Looking at pdfs of $\Delta\alpha$ under certain wind speed conditions. In a) pdfs for different time scales under the condition of $6 \leq |u| \leq 8$ m/s show increasingly Gaussian shapes the larger the time scale gets. This is quantified by the plot of the kurtoses in b) for different conditions. Where the original curve shows way larger values.

time in which changes in angle appear are important, the rates of the changes in time are being presented here. It is straight forward to calculate the distribution of $d\alpha/dt$ for a sampling rate of $\tau = 10$ Hz. Fig. 5.9 a) shows the distribution for $\Delta\alpha/\tau$ for a rotation of $n_{rpm} = 20$ rpm. In fig. 5.9 the rates are plotted for the standard deviation of the pdfs and the maximum values for different τ.

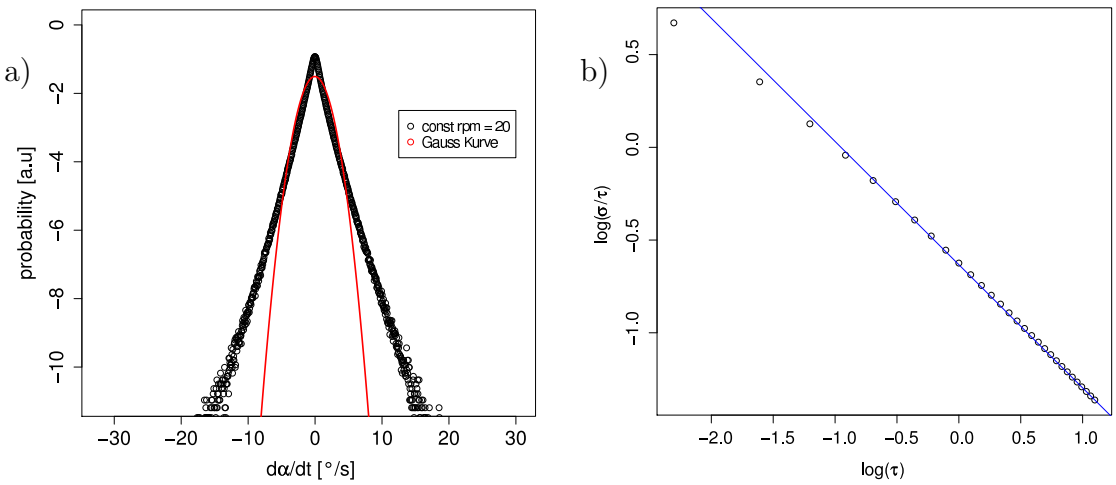

Figure 5.9: Probability density function of $\Delta\alpha/\tau$ for $\tau = 10$ Hz graphed with a Gaussian distribution for comparison, giving an idea for $d\alpha/dt$ a). The maximum rates and the rates for the standard deviation of the distribution for different τ is given in b).

5.5 Discussion and Conclusion

Inspired by the strong simplifications in the modeling of dynamic stall, we have shown an analysis of the statistical properties of the changes in the angle of attack estimated from the wind field. After a short analysis to characterize the wind field, we proposed a simple comprehensive model to estimate the changes in the angle of attack on a turbine blade at a certain rate of time. Basic turbulence characteristics from the wind field were thus transformed into characteristics which could be used for the modeling of dynamic stall on wind turbine blades.
The statistical properties of the wind speed and the wind direction showed the typical intermittent behavior. Even though the latter had a tendency to be less intermittent. Both changes in wind cause changes in the angle of attack on blades of a rotating turbine. Such changes therefore reflect the distributions of the changes in wind and showed in general also an intermittent distribution. Different cases were regarded in the study.
Two model cases were used to calculate the changes in AOA: case a) for constant tip speed ratio and case b) constant rotational speed. For both cases the changes in AOA with a moving average at a time scale $\tau_a = 2$ s were analyzed. In case a) the adaption of the rotational speed to a moving average of the wind speed caused the pdfs of the changes in AOA to be less intermittent than the ones for turbines running at a constant rotation rate.
To analyze the asymmetry in the pdfs, the same cases have been evaluated for

the instance of a change in wind direction only. Here pdfs for the changes in AOA show a strongly skewed behavior. However for the over all pdfs of the changes in AOA caused by wind speed and wind direction changes, it could be seen that the changes in wind speed dominate the effects on the changes on the AOA.
Since the aim was to find models for the changes in AOA that could be used for dynamic stall modeling the turbulent structure of the changes have been further analyzed. It was found for turbines running at a constant speed, that for time scales $\tau \geq 0.6$ s the standard deviation of the pdfs broadens by a power law $\approx \tau^{\frac{1}{3}}$. From this was concluded that the intermittent distributions over the complete time consist most likely of a superposition of mostly Gaussian distributions. For time scales $\tau < 0.6$ s this is not true anymore. So for AOA changes at time scales of $\tau \leq 0.5$ s larger values of the kurtoses and smaller values of the standard deviation are to be expected - indicating intermittent, non-Gaussian fields. Due to the small time scales, this is expected to lead to local aerodynamic effects on the blade as dynamic stall and will not happen on scales to which an existing controlling system would be able to react.
Since the main interest was to find characteristic distributions for the dynamic stall modeling the resulting conditioned pdfs for the changes in AOA have been fitted. The results showed slight deviations caused by the changes in wind direction. However the major characteristics were grasp very well. This makes new approaches for the modelling of dynamic stall for the optimization of wind turbine design possible.

Bibliography

[1] Simon-Philippe Breton, Frank N. Coton, and Geir Moe. A study on different delayed stall models using a prescribed wake vortex scheme and nrel phase vi experiment. In *Proceedings of the EWEC 2007*, 2007.

[2] Hermann Snel. Review of aerodynamics for wind turbines. *Wind Energy*, 6:203–211, 2003.

[3] William J. McCroskey. Unsteady airfoils. *Annual Review of Fluid Mechanics*, 14:285–311, 1982.

[4] C T Tran and D Petot. Semi-empirical model for the dynamic stall of airfoils in view of the application to the calculation of responses of a helicopter blade in forward flight. *Vertica*, 5:35–53, 1981.

[5] J Gordon Leishman and T S Beddoes. A semi-empirical model for dynamic stall. *Journal of the American Helicoper Society*, 34:317, 1989.

[6] Daniel Young Reber. *Modelbildung und Regelung zur Reduktion von Vibrationen und 'Dynamic Stall bei Hubschrauberrotoren.* PhD thesis, Universität Stuttgart, 2008.

[7] Sandeep Gupta and J. Gordon Leishman. Dynamic stall modelling of the s809 aerofoil and comparison with experiments. *Wind Energy*, 9(6):521–547, 2006.

[8] Alvaro Gonzales and Xabier Munduate. Unsteady modelling of the oscilating s809 aerofoil and NREL phase VI parked blade using the beddoes-leischman dynamic stall model. *Journal of Physics (conference series)*, (75), 2007.

[9] Philip Sura. Stochastic analysis of southern and pacific ocean sea surface winds. *Journal of Atmospheric Sciences*, 60(4):654–666, 2003.

[10] Adam H. Monahan. The probability distribution of sea surface wind speeds. part i: Theory and seawinds observations. *Journal of Climate*, 19(4):497–520, 2006.

[11] Frank Böttcher, Joachim Peinke, and Stephan Barth. Small and large scale uctuations in atmospheric wind speeds. *Stochastic Environmental Research and Risk Assessment (SERRA)*, 21(3):299–308, 2007.

[12] Wim Bierbooms. Simulation of stochastic wind elds which encompass measured wind speed series - enabling time domain comparison of simulated and measured wind turbine loads. volume European Wind Energy Conference Proceedings, 2004.

[13] Wim Bierbooms and Dick Veldkamp. Time domain comparison of simulated and measured wind turbine loads using constrained wind fields. In Joachim Peinke, Peter Schaumann, and Stephan Barth, editors, *Wind Energy*, Proceedings of the Euromech Colloquium, pages 15–20, 2007.

[14] Jeffrey Folge, Puneet Agarwal, and Lance Manuel. Towards an improved understanding of statistical extrapolation for wind turbine extreme loads. *Wind Energy*, 11:613–635, 2008.

[15] Bonnie J. Jonkman and Marshall L. Buhl Jr. *TurbSim Users Guide*. National Renewable Energy Laboratory, tp- 500-41136 edition, 2007.

[16] Anand Natarajan, William E. Holley, Reveendra Penmatsa, and Bhanu Chandar Brahmanapalli. Identification of contemporaneous component loading for extrapolated primary loads in wind turbines. *Wind Energy*, 11:577–587, 2008.

[17] Partick Moriarty. Database for validation of design load extrapolation techniques. *Wind Energy*, 11:559–576, 2008.

[18] Frank Böttcher. *Statistische Analyse der atmosphaerischen Turbulenz und allgemeiner stochastischer Prozesse*. PhD thesis, Oldenburg University, 2005.

[19] Scott Schreck. Spectral content and spatial scales in unsteady rotationally augmented flow fields. *Journal of Physics (conference series)*, 75, 2007.

[20] Scott Schreck and Michael Robinson. Three-dimensional dynamic stall response to wind turbine operation condition. *J. of Sol. En. Eng.*, 127:488–495, 2005.

[21] Eric van Doorn, Brindesh Dhruva, Katepalli R. Sreenivasan, and Victor Cassella. Statistics of wind direction and its increments. *Physics of Fluids*, 12(6):1529–1534, June 2000.

[22] Kurt Schaldemose Hansen and Gunner C. Larsen. Full scale experimental analysis of extreme coherent gust with wind direction changes (eod). *Journal of Physics (conference series)*, 75, 2007.

[23] Wen Zhong Shen, Martin O. L. Hansen, and Jens Nørkær Sørensen. Determination of angle of attack (aoa) for rotating blades. In Joachim Peinke, Peter Schaumann, and Stephan Barth, editors, *Wind Energy*, Euromech Colloquium, pages 205–209. Springer, 2007.

[24] Wen Zhong Shen, Martin O. L. Hansen, and Jens Nørkær Sørensen. Determination of the angle of attack on rotor blades. *Wind Energy*, (1):91–98, 2009.

[25] Tonio Sant, Gijs von Kuik, and Gerard J. W. van Bussel. Estimating the angle of attack from blade pressure measurements on the NREL phase VI rotor using a free wake vortex model: axial conditions. *Wind Energy*, 9:549–577, 2006.

[26] Tonio Sant, Gijs von Kuik, and Gerard J. W. van Bussel. Estimating the angle of attack from blade pressure measurements on the national renewable energy laboratory phase VI rotor using a free wake vortex model: Yawed conditions. *Wind Energy*, (1):1–32, 2009.

[27] Julia Gottschall. *Modelling the variability of complex systems by means of Langevin processes*. PhD thesis, Oldenburg University, 2009.

[28] IEC. International standard iec 61400-1, wind turbines part 1: Design requirements. Technical report, International Electrotechnical Commission, 2005.

[29] Frank Böttcher, Joachim Peinke, Christoph Renner, and Hans-Peter Waldl. Onthe statistics of wind gusts. *Boundary-Layer Meteorology*, 108:163–173, 2003.

[30] B. Castaing, Y. Gagne, and E. J. Hopfinger. Velocity probability density functions of high reynolds number turbulencs. *Physica D*, 46:177–200, 1990.

[31] A. N. Kolmogorov. The local structure of turbulence in an incompressible viscous flow for very high reynolds numbers. *Dokl. Acad. Nauk. SSSR*, 305:301–305, 1941.

Kapitel 6

Conclusion

The aerodynamics of wind energy will always face very turbulent conditions. The aerodynamics of turbulent flow stay to be a challenging field for research. This work is a contribution to this research.
One of the promising tools in the aerodynamics are CFD methods, though there exist a lot of problems modeling the turbulent flow. Therefore a description of the mathematical method for spectral finite elements calculations with the code $\mathcal{N}\varepsilon\kappa\mathcal{T}\alpha r$ was given in Chapter 2. Characteristics, theoretical accuracy and parallelization method were outlined. Since in the process of the thesis some difficulties using the code appeared, the difficulties and limits of the code were described. Problems occurred especially due to the necessity of a very well resolved flow field. Also throughout the whole further simulations one problem remained the necessity to resolve even the smallest geometries with a grid. Since the main convergence is however done by the polynomial order p, this lead to absurdly high resolutions in some areas with high computational costs. An open question remains also the reason of an effect caused by implementation of the parallel computing which can be observed in the results of the simulation.
Even though the code has some drawbacks, it has the strong advantage of very high accuracy, which can be very flexibly varied due to p-refinement. Thus good simulation results were achieved in a 3D simulation on an fx79-w151a airfoil at Re=5000 as described in chapter 3. At this Reynolds number the loads on the airfoil were dominated by a von Karman like vortex street in the wake of the airfoil. The flow on most of the airfoil remained laminar. Only in the tail region, where an impingement point could be found, a turbulent flow region developed.
This turbulent region was analyzed in chapter 4. At some selected points within the region an investigation on time series data has been done. At a specific point a complete analysis of the time series of velocity increments was done. Evidence for the validity of Markov properties were found although the dataset was rather short. Investigating the Kramers-Moyal coefficients it was found that at the regarded point $D^{(4)} \geq 0$, so that reconstruction of the time series using a Langevin equation based on Gaussian white noise showed some slight deviances from the

simulated time series. An extrapolation of the method by Taylor hypothesis to a spatially distant point using the statistical results from the first point, gave surprisingly good results. The whole flow field was inhomogeneous and anisotropic. Thus the agreement between the reconstructed new time series with a time series from the simulation was quite satisfying. However, slight deviances could still be observed in the mean flow and standard deviation of some components. There were multiple reasons for the deviation, as

- the short time series for the base of the stochastic analysis leaving much room for statistical errors,
- higher moments that were not taken account of by the used Langevin equation, based on Gaussian white noise,
- the inhomogeneous turbulent field influenced by the shear of the laminar separation on one hand and the airfoil on the other.

Apart from the latter, all of these reasons pose known solvable problems. This gives hope stochastic turbulence modeling in fluid dynamics, since such models depend on a good description of the statistical properties of a flow at positions or time scales.
In chapter 5 the effect the turbulence has on a model turbine was studied by the fluctuations on the angle of attack (AOA) on the blade. Therefore 10Hz data from a wind field measurement was characterized. For different types of simplified wind turbine models the effect on the AOA has been studied. For the investigated time scales of $0.1 \leq \tau \leq 3.0$s it was found that the changes in wind direction had a rather small effect on the changes compared to wind speed changes. The intermittent structures of the wind field increments were directly found in the statistics of the increments in the AOA. However, the extreme effects of the intermittency could be reduced by some controlling. Since the regarded time scales were so small, the fluctuations correspond to small, local structures, so that a control system is not expected to respond in time. For the probability density function of the changes a fit was done successfully, which makes more realistic dynamic stall simulations and measurements for wind turbines possible.

Kapitel 7

Outlook

This work has certainly been only a small piece of the enormous project of the correct description of the turbulent aerodynamics of wind turbines. The resulting curves for the changes in the angle of attack, however, could be used directly for dynamic stall measurement experiments in the future.
For CFD simulations of such dynamic stall effects with reliable results the improvement of the existing turbulence models is still required. The results of the reconstruction of the time series in the inhomogeneous turbulent field give a boost to the hope that stochastic models might be able to fulfill the necessary closure for turbulent fluid flow problems. Certainly until then there is still a long way to go, as the results are expected to improve with more data. Also the open question remains how the turbulent properties develop depending on shear, the boundary layer or the Reynolds number.
The method of spectral finite elements allows us to progress with this investigation with high accuracy. Although the method does have many drawbacks, in the end it was possible to use it for stable 3D simulations at least to Re=20000 as shown in fig. 7.1, where the flow is a lot more turbulent than in the so far described simulations.

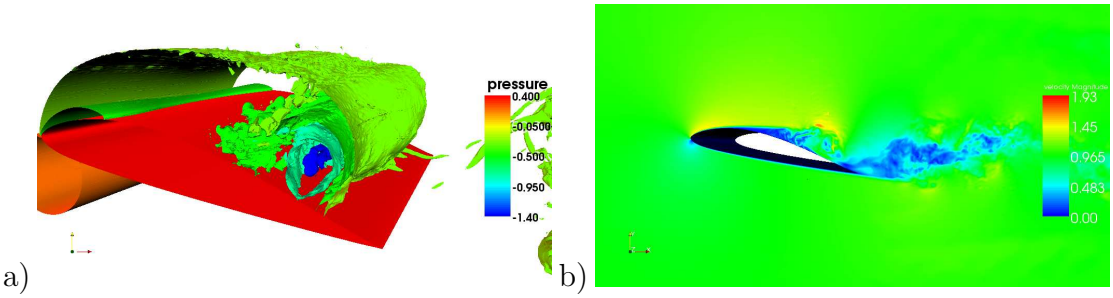

Abbildung 7.1: Snapshots of a simulation on the fx79-w151a airfoil at a Re=20000 - pressure contours in a) and a slice of the velocity magnitude in b) show a transient and turbulent flow on the airfoil. The spanwise resolution has been reduced for the postprocessing for the figures to keep the size of the data in a file manageable on a PC.

Acknowledgements

In the end i would like to thank Joachim Peinke for supervising and advising me in this work, yet leaving the a lot of freedom for own ideas and creativity. Also would like to thank Claus Wagner and Andrei Shishkin for all the support i got from them on a certainly not trivial task of handling the $\mathcal{N}\varepsilon\kappa\mathcal{T}\alpha r$-code and Spencer Sherwin for providing the code and for being open to answer question from people he doesn't know.
I would like also to acknowledge my TWiSt group for all the encouragement, advice and the good team work and nice times we had during all the time: Stephan Barth, Michael Hölling, Michael Langner, Bianca Schulte, Björn Ahrens, Edgar Anahua, Thomas Bohlen, Rene Güneberger, Gerd Gülker, Mathias Hölzer, Wilhelm Jürgensen, Pascal Knebel, Michael Langner, Anne Laupichler, Stephan Lück, Jens Lühning, Max Meessen, Amjed Mohammed,Agnieszka Parniak, Anne Schmidt, Christian Steigerwald, Nils Kirrkamm, Henning Foeste, Sebastian Marten, Motaher Hussain, Jörge Schneemann, Hendrick Heißelmann, Thomas Greve, Tim Hohmeyer, Allan Morales, Jaroslaw Puczylowski, Arnold Gräbeldinger and Gerrit Wolken-Möhlmann. Especially i would like to thank Julia Gottschall, David Kleinhans, Tanja Mücke, Philip Rinn, Wided Medjroubi, Robert Stresing, Patrick Milan and Matthias Wächter for directly supporting me in this work by reading, criticizing or answering quickly to my multiple questions.
Finally i would like to thank my Commune Alla Hopp for supporting, feeding and pampering during all the time when i was gone so much - either physically or mentally.

Lebenslauf

Persönliche Daten:

Name:	Bernhard Stoevesandt
geboren am	8.6.1970 in Bremen
Staatsangehörigkeit	Deutsch

Schulausbildung:

1977-1980	Besuch der Grundschule am Baumschulenweg Bremen
1981-1987	Orientierungsstufe und Besuch des Gymnasiums am Barkhof
1987-1988	Washington Highschool, Washington, IN
1988-1991	Besuch der Oberstufe und Abitur am Kippenberg-Gymnasium Bremen

Studium:

1993-2000	Physik-Studium an der Universität Bremen
1999-2000	Diplomarbeit in Kooperation mit der TU-Berlin Thema: Erstellung und Verifizierung eines Monte-Carlo-Simulationsprogramms für die tiefensensitive Mikro-Röntgenfluoreszenzanalyse

Berufstätigkeit:

2000-2001	Freiberufliche Tätigkeit: Entwurf einer HOPG-Röntgenlinse für das FZ-Rossendorf
2002-2004	Wissenschaftlicher Mitarbeiter der Universität Oldenburg und Meteocontrol GmbH im Bereich der Windleistungsvorhersage
seit 2004	ausschließlich Wissenschaftlicher Mitarbeiter im Institut für Physik an der Carl-von-Ossietzky Universität Oldenburg

Erklärung

Ich erkläre hiermit, dass ich diese Arbeit selbstständig verfasst und nur die angegebenen Hilfsmittel benutzt habe.

Oldenburg, den .....

.....

(Bernhard Stoevesandt)

Publikationsliste

der in dieser Arbeit enthaltenen Veröffentlichungen

B. Stoevesandt, A. Shishkin, C. Wagner and J. Peinke Direct Numerical Simulation of the Turbulent Flow Around an Airfoil *European Conference on Computational Fluid Dynamics ECCOMAS CFD 2006*, edited by P. Wessling, E. Onate, and J. Periaux, ISBN 90-9020970-0, 2006

Die Arbeit wurde durch J. Peinke betreut. A. Shishkin und C. Wagner haben durch Hinweise und Anmerkungen unterstützt. Die wissenschaftliche Ausarbeitung stammen von B. Stoevesandt

B. Stoevesandt, R. Stresing, A. Shishkin, C. Wagner and J. Peinke Multipoint Correlations in Direct Numerical Simulations *Prepared to be submitted to Physics of Fluids*

Die Arbeit wurde durch J. Peinke und C. Wagner betreut. J. Peinke und R. Stresing haben mit Rat und Ideen bei der Ausarbeitung, C. Wagner mit sprachlicher Überarbeitung unterstützt. A. Shishkin hat das Gitter zur Verfügung gestellt. Die wesentlichen Ideen und wissenschaftlichen Ausarbeitungen stammen von B. Stoevesandt

B. Stoevesandt, J. Peinke Effects of Sudden Changes in Inflow Conditions on the Angle of Attack on HAWT Blades *Prepared to be submitted to Wind Energy*

Die Arbeit wurde durch J. Peinke betreut, die wesentlichen Ideen und die wissenschaftliche Ausarbeitung stammt von B. Stoevesandt

Die Anteile der aufgeführten Autoren entsprechen den Angaben.

Oldenburg, den 26. November 2009

.....

(Prof. Dr. J. Peinke)

Weitere Publikationen mit meiner Beteiligung

B. Stoevesandt, E. Engel, M. Lange, G. Heilscher, S. Bofinger Comparing wind-prediction systems for power predictions *in Proceedings EWEC 2004*, London 2004

B. Stoevesandt, J. Peinke, A. Shishkin, C. Wagner Simulation Dynamic Stall using Sprectral/HP Method *in Proceedings EWEC 2006*, Athen 2006

B. Stoevesandt, A. Shishkin, C. Wagner, J. Peinke DNS of the turbulent flow around an Airfoil for Wind Turbines using Spectral/HP Method *in Proceedings DEWEK 2006*, Bremen 2006

B. Stoevesandt, J. Peinke, A. Shishkin and C. Wagner Numerical simuation of dynamic stall using spectral /hp method *in Wind Energy - Proceedings of the Euromech Colloquium*, eds. J. Peinke, P. Schaumann, St. Barth, (Springer, Berlin 2007) p. 241 - 244

B. Stoevesandt Learning form nuclear power? Better strategies for wind power! *in Proceedings EWEC 2007*, Milano 2007

B. Stoevesandt, J. Peinke, A. Shishkin and C. Wagner Computational simulation of the turbulent flow around an airfoil using spectral/hp method *in Proceedings EWEC 2007*, Milano 2007

B. Stoevesandt, C. Steigerwald, A. Shishkin, C. Wagner, J. Peinke Analysing flow structures around a blade using spectral/hp method and HPIV *in Proccedings of The Science of Making Torque from Wind* eds. Jens N Sorensen, Martin O L Hansen and Kurt S Hansen, (Journal of Physics: Conference Series, Volume 75, 2007) 012025

B. Stoevesandt, J. Peinke Changes in angle of attack on blades in the turbulent wind field *in Proceedings of EWEC 2009*, Marseille 2009